CROSS–SECTIONAL STM ANALYSIS OF MBE–GROWN InAs / InAsSb STRAINED–LAYER SUPERLATTICES

A Dissertation

by

KARA MAXINE KANEDY

Submitted to the Office of Graduate and Professional Studies of
Texas A&M University
in partial fulfillment of the requirements for the degree of

DOCTOR OF PHILOSOPHY

Chair of Committee,	Michael B. Weimer
Committee Members,	Glenn Agnolet
	Alexey Belyanin
	Christie K. Madsen
Head of Department,	George R. Welch

May 2016

Major Subject: Applied Physics

ABSTRACT

We show how cross–sectional scanning tunneling microscopy is used to examine a gallium–free, type–II InAs/InAsSb superlattice and perform compositional analyses of the *as–grown* structure through isovalent impurity identification. We describe the optimization of cleaving protocols, upgrades to the vacuum system, and standardized lab protocols for minimizing STM non–idealities. These improvements allow acquisition of representative, device–scale STM surveys yielding statistically–significant image ensembles.

We describe protocols for identifying surface antimony–for–arsenic substitutions in STM images, which facilitate monolayer–by–monolayer analyses of the antimony fraction across surveyed repeats. Reconstruction of representative bulk composition profiles, based on appropriate approximations to the bulk period, reveal compositional grading across superlattice interfaces consistent with anion segregation. HRXRD simulations based on these profiles provide insights into the discrepancies between intended and observed x–ray spectra.

We develop a quantitative, continuum segregation model to fit the observed antimony profiles, and examine the resulting fit parameters to determine what they reveal about segregation and cross–incorporation in InAs/InAsSb superlattices. We show how the model best describing the bulk profile relies on two, spatially distinct segregation sources with an offset close to one monolayer, consistent with either

monolayer roughness or substrate vicinality. This model also provides self–consistent period measurements over surveyed sections of the multilayer stack, that agree with bulk period approximations based on sliding window averages, thereby substantiating the occurrence of more than one bulk period in the superlattice. The insights achieved through such detailed analyses of the *as–grown* structure can be combined with STM and SIMS data pointing to a vertical evolution in the total incorporated antimony per period to obtain x–ray simulations in excellent agreement with the experimental HRXRD spectrum.

Finally, we demonstrate how cross–sectional STM may be used to measure local periods in superlattice structures via a novel, reciprocal–space technique analogous to Bragg's law in x–ray diffraction. The period measurements obtained with this technique are compared with those from sliding–window averages and the continuum segregation–model to validate the accuracy of this new method, and pinpoint period variations within the multilayer stack.

to my wonderful husband

ACKNOWLEDGEMENTS

I would like start by thanking my advisor, Dr. Michael Weimer for his guidance and patience throughout my studies here. I am also thankful for the assistance of my committee members, Dr. Glenn Agnolet, Dr. Alexey Belyanin, and Dr. Christie K. Madsen. Thanks also go to Eric Shaner, John Klem, and Jin Kim at Sandia National Laboratories for the sample used in this study.

So much of this work was a collaborative effort, and I am very grateful to Federico Lopez and Matthew Wood for all of their help with data acquisition as well as the discussions and critical input for data analysis.

I would also like to thank members of the Physics Electronic and Machine Shop for their assistance in improving and maintaining the instruments used in this study.

Many thanks go to my family for their love and support during my time here in College Station, and also to my friends at Beacon Baptist Church for all the encouragement and prayers.

Finally, a special thanks to my husband for his love, encouragement, and especially patience. He motivated me to keep going when things got rough and seemed as though they would never end.

TABLE OF CONTENTS

LIST OF FIGURES

Page

CHAPTER I

INTRODUCTION

Background and Motivation

Several applications utilize infrared (IR) radiation to gain information; these include environmental monitoring, terrestrial surveillance, missile warning systems, and astronomical research. Infrared radiation is electromagnetic radiation with wavelengths between visible light and microwaves, about 0.7 to 1000 microns. The long–wavelength (8–14 μm) IR region is often referred to as the 'thermal infrared' where there is considerable interest for the aforementioned applications. The most common material currently used to fabricate infrared structures is mercury–cadmium-telluride (HgCdTe). HgCdTe was first proposed as an IR absorber material by Schulman and McGill [1] in 1979 and has been the dominant source for infrared systems over the last few decades.

However, there are challenges faced by devices fabricated with the $Hg_{1-x}Cd_xTe$ alloy that have yet to be overcome, such as strong dependence on alloy composition [2] and compositional uniformity at longer wavelengths, creating strict composition requirements that are difficult to accomplish. Another challenge that still plagues HgCdTe devices is Auger recombination [2] (Fig 1.1). Within semiconductors Auger recombination involves two electrons and one hole, or one electron and two holes. After an electron–hole pair form, their energy is given to a third carrier, which increases its energy moving it to a higher energy level within the same energy band. This process decreases carrier lifetimes.

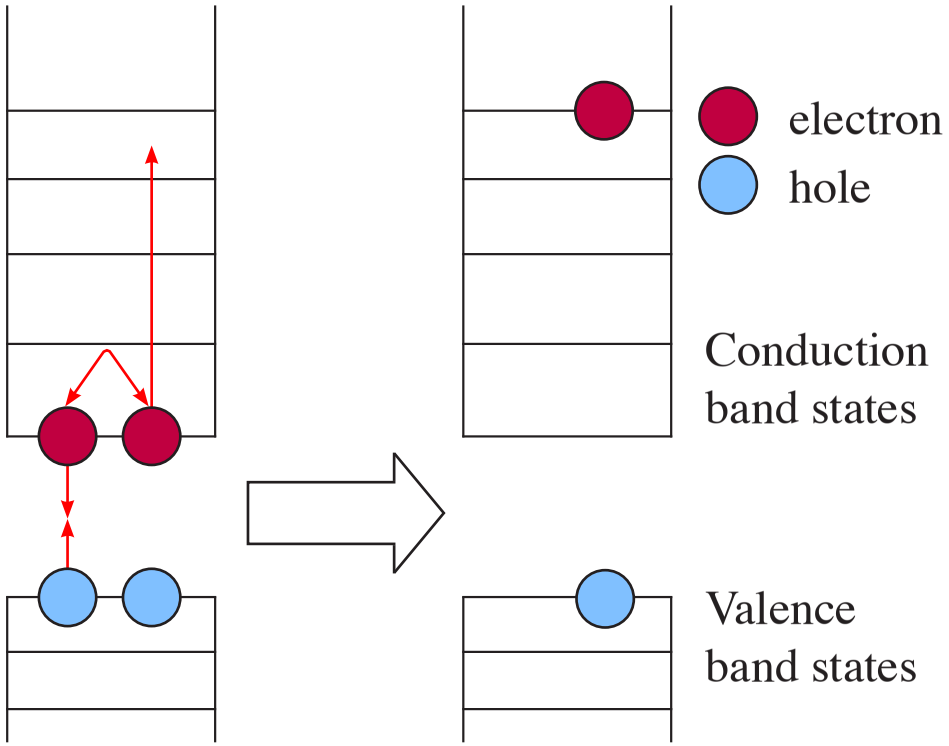

FIGURE 1.1. Auger Recombination involves two electrons and one hole (illustrated), or one electron and two holes. An electron and hole combine and the energy is given to a third carrier, which is excited to a higher energy level without moving to another energy band.

Lack of progress in recent years with regard to long-wavelength IR devices made from HgCdTe has led to increased interest in the prospects for devices built from the III–V materials system. Within this materials system (Fig 1.2, [3]) there are a number of binary and ternary compounds (e.g. InAs, GaSb, InAsSb, GaInSb) with lattice constants very close to each other, which can be grown with monolayer precision by way of a well–established growth method such as molecular beam epitaxy (MBE) [4, 5]. The alloy composition and layer thickness of the constituent layers within this type of structure can be adjusted to control the energy gap to fit a specific application, i.e. band–gap engineering.

The deliberate tailoring of optical transitions in such quantum–confined structures typically relies on theoretical or empirical paradigms whose predictive utility is judged against assumed (*intended*) rather than empirically determined (*as–grown*) constituent–layer sequences. Accurate knowledge concerning the *as–grown* atomic arrangements responsible for the confining potentials that make these structures unique is rarely available.

Cross–sectional scanning tunneling microscopy (STM) has proven to be a powerful tool for characterizing III–V semiconductor heterostructures with exceptional atomic resolution. STM is capable of providing real–space structural as well as morphological information on the cross–sectional epitaxial layers exposed through cleavage [6-8]. This analysis can be performed across the entire *as–grown* structure, characterizing any changes in the aforementioned properties from initiation to completion of the growth.

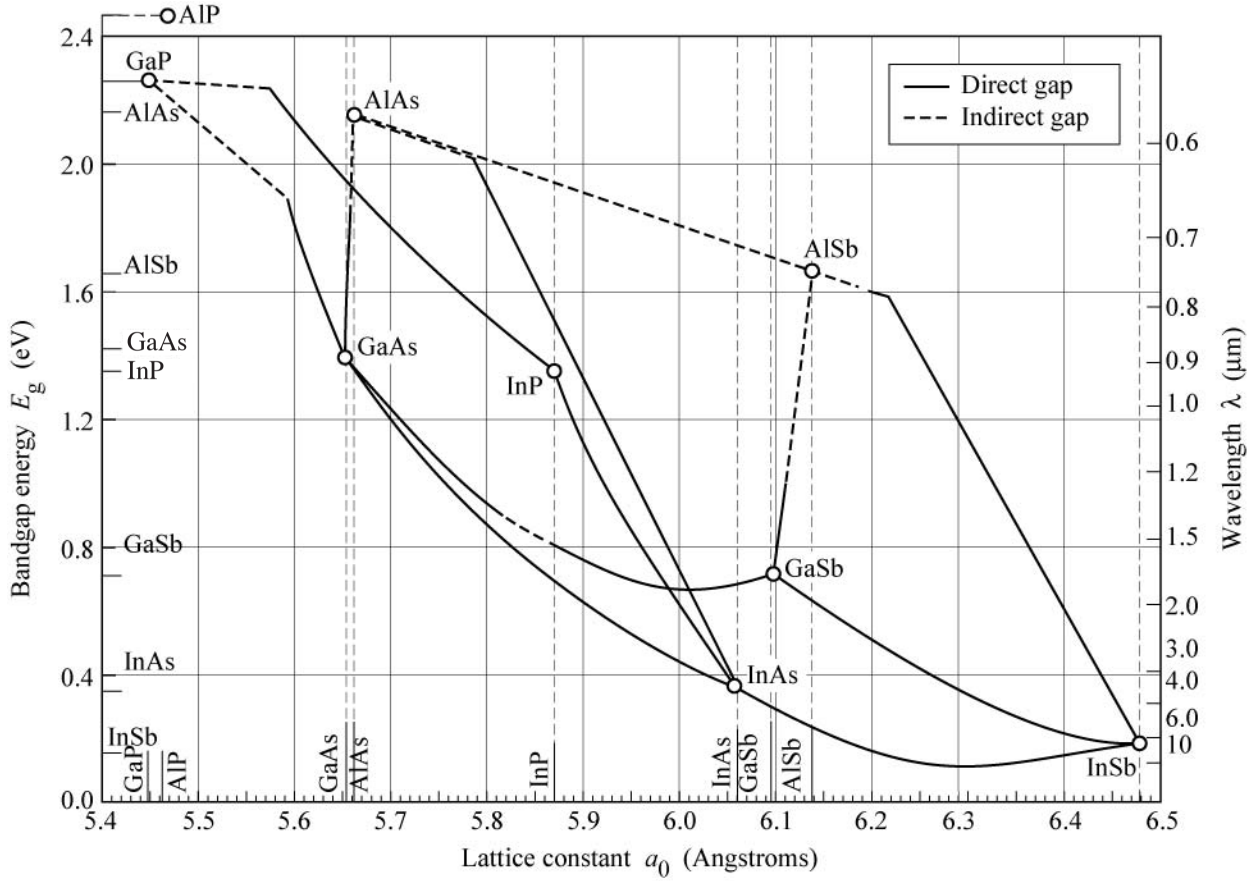

FIGURE 1.2. Bandgap energies and lattice constants for several III / V semiconductor alloys. With the proper choice of alloy composition and thickness, it is possible to fabricate heterostructures from these materials with atomic layer precision. Reprinted from the internet [3].

Alternative Infrared Device Materials

There are two band alignments formed from the III–V material system (Fig. 1.3). In one type of alignment, the electrons and holes are confined in a common potential well of the superlattice so that shifts in the electron and hole energy levels are coupled with changes in the well width (commonly referred to as type–I). In the other band alignment (type–II) electrons and holes are separately confined in neighboring layers whose thicknesses may be independently adjusted to achieve a desired optical transition energy, providing a degree of freedom not available with the type–I system.

InAs/GaSb type–II superlattices were first introduced in 1977 by Sai–Haiasz and Esaki [9], and ten years later Smith and Mailhiot [10] proposed their use for infrared detection. Theoretical calculations predict that InAs/GaSb type–II superlattices have a similar absorption coefficient to that of HgCdTe, and the strain present in InAs/GaSb suppresses Auger recombination [11], which should result in longer intrinsic carrier lifetime and higher quantum efficiency for the detectors. This suggests that type–II superlattices based on the InAs/GaSb system might hold distinct advantages over HdCdTe in long-wave-infrared applications. This non–common–atom binary material, and its closely–related, ternary variant InAs/Ga(In)Sb, have thus been extensively studied, but have not yet reached their theoretical potential, nor have they surpassed the HgCdTe–based devices. This is believed to be due to native defects formed during growth in the bulk InAs or bulk GaSb leading to Shockley–Read–Hall recombination [12]. Measurements of the carrier lifetimes of bulk InAs, bulk InAsSb, and bulk GaSb revealed that the GaSb had the shortest lifetime [13]. This suggests the defect limiting

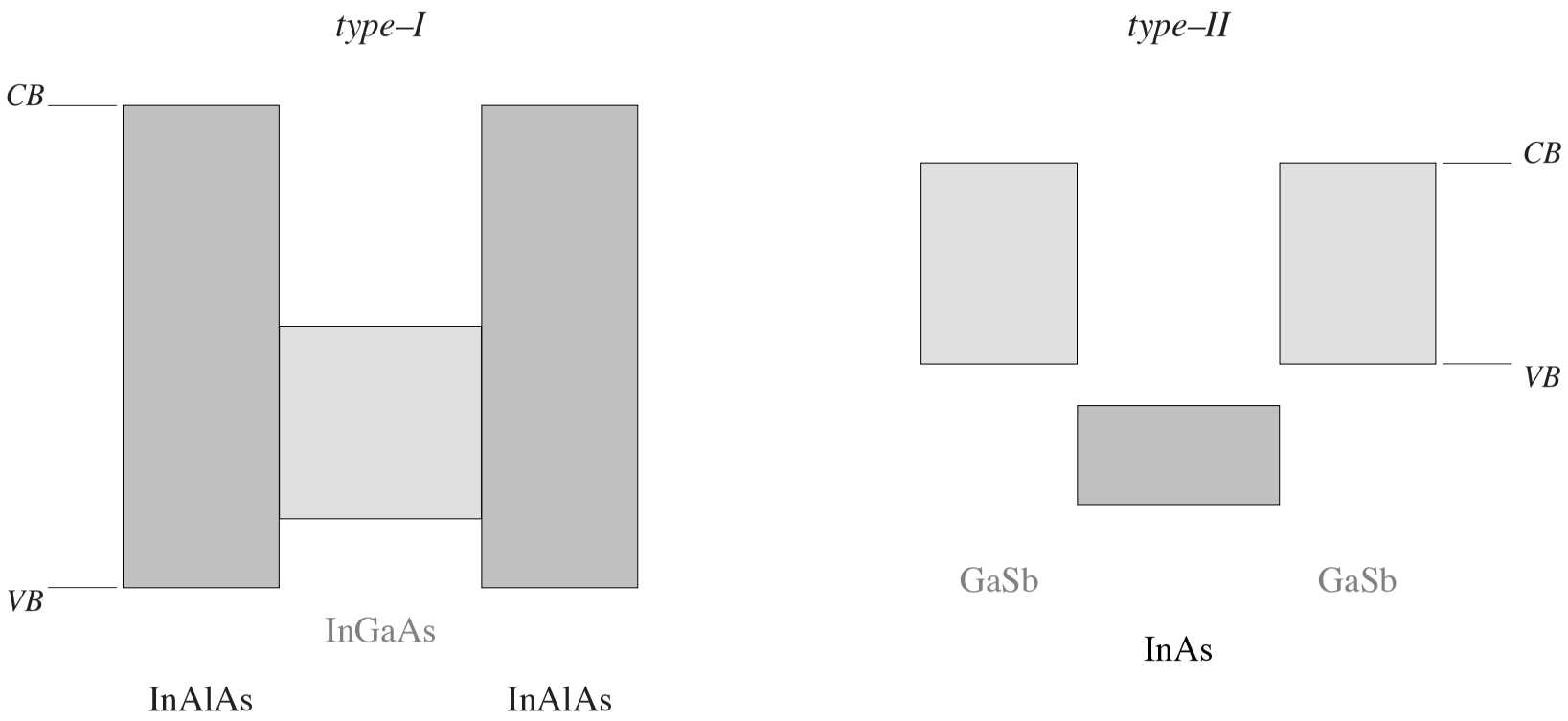

FIGURE 1.3. Representative energy band diagrams contrasting type–I and type–II band alignments. A type–I band alignment confines electrons and holes to one layer of the superlattice, causing any tailoring of the layer thickness to modify both electron and hole energy levels. Type–II superlattices, on the other hand, confine electrons and holes in neighboring layers whose thicknesses may be independently adjusted to achieve a desired optical transition energy.

the carrier lifetimes of InAs/Ga(In)Sb structures is located in the bulk GaSb, and that type–II superlattices without Ga will have longer carrier lifetimes.

The Ga–free type–II superlattice InAs/InAsSb, was proposed in 1995 by Grin et al [11], and demonstrated potential to replace the incumbent HgCdTe in infrared devices at longer wavelengths. From recent reports [14], InAs/InAsSb superlattices have exhibited carrier lifetimes an order of magnitude greater than those observed in InAs/Ga(In)Sb, possibly connected with the gallium–free nature of the structure. This has led to renewed interest in the prospects for competitive devices built from this Ga–free material.

Molecular Beam Epitaxy

Solid–source molecular beam epitaxy (MBE) has become a primary tool for fabricating superlattice structures. In an MBE setup (Fig.1.4, [15, 16]), there are several high temperature effusion cells inside an ultra high vacuum (UHV) chamber, each providing an elemental source such as gallium, indium, aluminum, or arsenic. The UHV environment increases the mean free path of the elements to be deposited, with excellent control over growth conditions for atomically thin, epitaxial films. The cells are arranged in the vacuum system with their beam paths directed towards the substrate mounted near the center of the chamber. Each effusion cell is heated to the sublimation temperature of its respective element, and the sources are projected as beams towards a substrate wafer where they diffuse to form molecules. Adjustments to the temperature of the effusion cells control the amount of material reaching the substrate, and to minimize

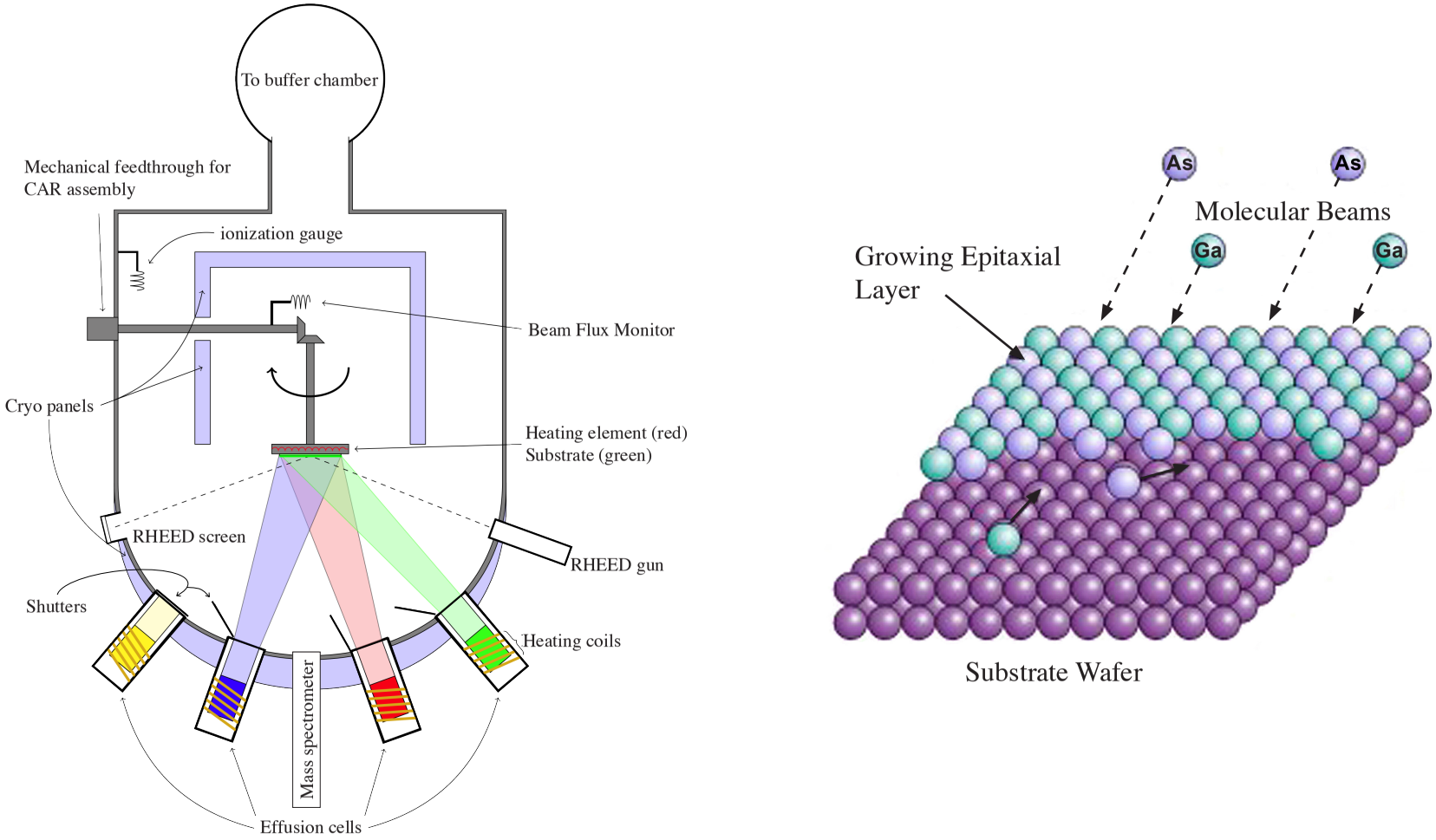

FIGURE 1.4. Schematic of a typical MBE system in an ultra–high–vacuum chamber. Pneumatic shutters permit growth of a specific layer sequence. Substrate is continuously rotated to improve layer uniformity. Reprinted from the internet [15,16].

concentration gradients the substrate is typically rotated as well as heated during growth. Computer-controlled pneumatic shutters placed just beyond the end of the effusion cells allow for termination of the material flux from each cell separately. The shutters are opened and closed in a controlled sequence allowing for deposition of the desired layer thicknesses to fabricate the intended structure. More in-depth descriptions of MBE systems can be easily found in literature [17, 18].

Materials Issues During Epitaxy

During epitaxial growth of type–II quantum structures, the anions and/or cations are adjusted at each layer interface, and it is important to maximize the quality of these interfaces for optimal device performance. Anion segregation and cross–incorporation [7, 8] (Fig. 1.5) are two well–known atomic–scale processes that occur during growth, where two or more anions compete for the available lattice sites. These processes frustrate the intended compositional discontinuities across the heterojunctions, which in turn affect the optical and electronic properties of the quantum structure.

Anion segregation refers to the geometric progression in anion incorporation that follows exposure of a growth surface to competing anion fluxes. For example, when antimony is co–deposited with arsenic, some portion of the antimony flux is incorporated in the current monolayer, while the remaining fraction is ejected to a floating layer on the surface and made available (in addition to the incoming flux) for incorporation into the next monolayer. Once the antimony–source shutter is closed, this

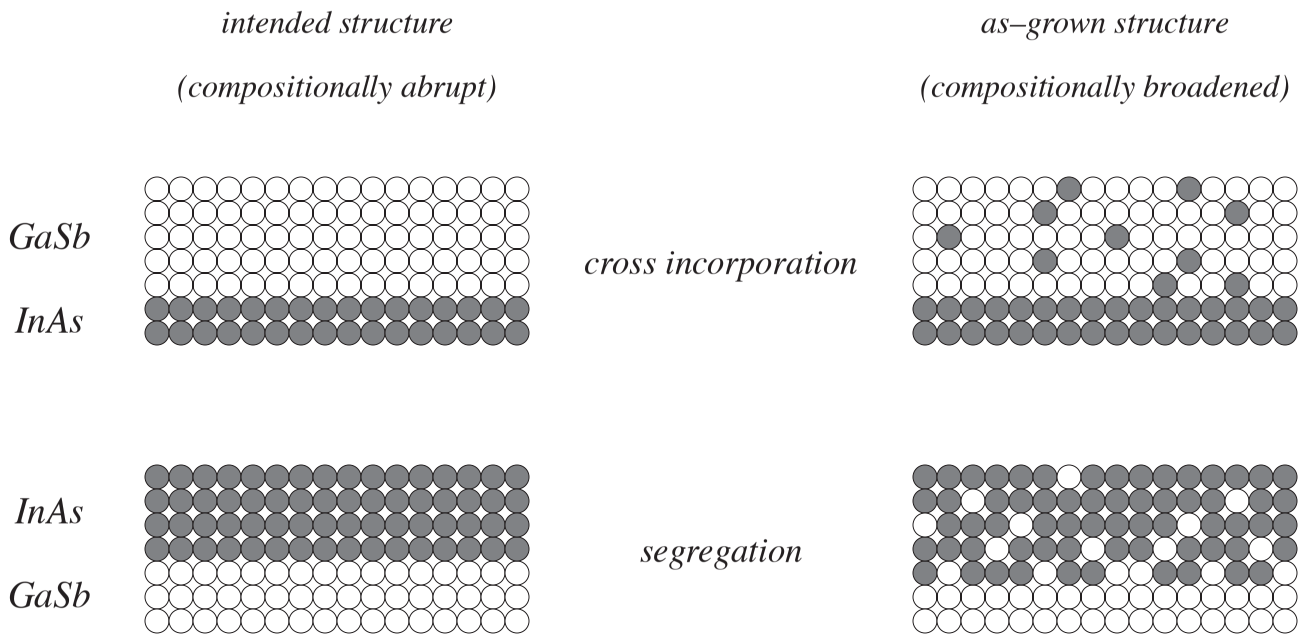

FIGURE 1.5. Simplified schematic illustrating processes that occur during MBE growth. These processes complicate the optimal growth of type–II structures.

partitioning continues as additional arsenic layers are formed until the antimony floating layer is exhausted or the shutter is opened again.

Anion cross–incorporation refers to a spatially uniform, random distribution of a foreign species incorporated into the growth via unintended substitution for another anion. The anion species produced by the effusion cells are typically molecular (e.g. Sb_2) while the cations are atomic (e.g. In). The sticking probability for the anion molecules is also smaller than that for the cation atoms, so an anion overpressure is (almost) universally required for stoichiometric growth [19, 20]. As the anion vapor in the effusion cell increases, molecules will leak around the effusion cell shutter forming an unwanted ambient background, which will then compete with the intended anion stream for incorporation during growth.

These non–idealities play an important role in the optical and electronic properties of the *as–grown* structure. Strain introduced by cross–incorporation and segregation influences transport of carriers through the structure. Interfacial mixing and compositional grading due to segregation leads to overall softening of band–edge confinement potentials, and likewise influences transport effective masses.

Characterization Techniques

Epitaxial growth with atomic layer precision is aided by reflection high–energy electron diffraction (RHEED), a standard analytical tool used in MBE systems for monitoring the growth quality in real time [21]. In a RHEED system (Fig 1.6) an electron gun produces a beam of high-energy electrons that strike the sample surface at

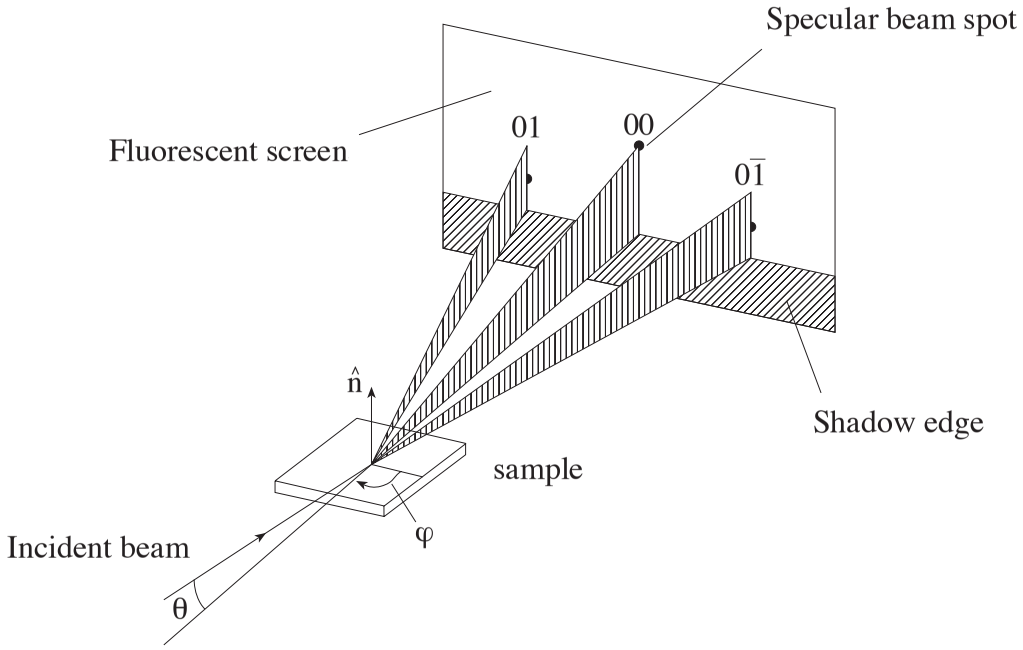

FIGURE 1.6. Relative geometry of electron beam path and growth surface for *in situ* monitoring by RHEED.

grazing incidence. Incoming electrons diffract off the topmost layer of the sample, and a small fraction of the diffracted electrons are observed with the detector screen. Diffraction patterns are formed at the detector when the diffracted electrons constructively interfere at specific angles corresponding to the spacing of the surface atoms. Valuable information about the structure and morphology of the sample surface during growth is made available from these electron diffraction patterns.

While RHEED provides *in-situ* monitoring of growth modes and surface reconstruction during growth, *ex–situ* characterization techniques are needed to better evaluate the quality of the grown heterostructure and to optimize growth conditions. Structural information on the growth quality can be obtained from such techniques as high–resolution x–ray diffraction (HRXRD) and transmission electron microscopy (TEM), while photoluminescence (PL) provides compositional insights regarding bound states of the heterostructure. These techniques spatially average over a large portion of the heterostructure; therefore, essential structural and compositional insights in the sub–nanometer scale regarding the electron confinement are not easily accessible.

Scanning Tunneling Microscopy

Scanning tunneling microscopy (STM) has been utilized for atomic–scale characterization of semiconductor surfaces for several years. An atomically sharp metal tip is brought very close to the sample surface and a small bias is applied between the two allowing electrons to tunnel through the vacuum barrier between the tip and

dangling bonds of the surface atoms [22]. A one–dimensional tunneling schematic is illustrated in Fig 1.7 [23]. The tunneling current between the tip and sample

$$I \propto \int_0^{eV} \rho_s(E,eV)\ T(E,eV)\ dE \tag{1.1}$$

is a function of the local density of states for the sample, ρs, with a transmission coefficient,

$$T(E,eV) \propto \exp(-2\kappa s) \tag{1.2}$$

which has an exponential dependence on the separation, s, between tip and sample. T also depends on the applied voltage, V, according to

$$\kappa = \sqrt{\frac{2m}{\hbar^2}\left(\overline{\Phi}(eV) - E\right)} \tag{1.3}$$

where Φ is the mean barrier height, and κ is on the order of 1 $Å^{-1}$.

Cross–sectional STM allows for investigation of *as–grown* heterostructures through cleavage in vacuum and subsequent exposure of the epitaxial layers in cross section; a simple schematic of the technique appears in Fig. 1.8. The III–V materials that make up the structure examined in this study have the zincblende structure for which there are two orthogonal crystal planes, (110) and (1–10), containing equal numbers of anions and cations in zig–zag chains. These two non–polar planes are preferential when cleaving the structure. Following cleavage along a <110> plane, the surface undergoes a Jahn–Teller relaxation [24] rather than reconstructing, where the anions and cations experience a coordinated rigid–bond rotation. This leads to a shift in the cleavage

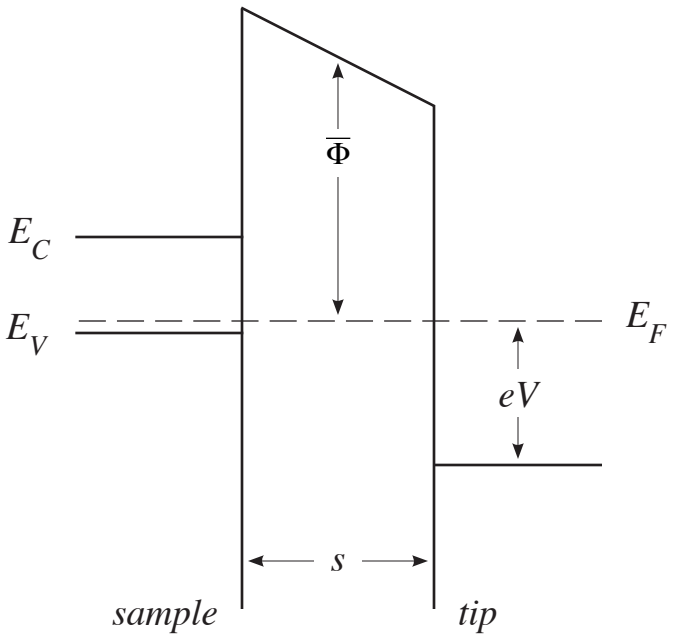

FIGURE 1.7. Schematic electron energy diagram illustrating a typical, planar tip-sample junction. Sample is biased, by a voltage V, to adjust its Fermi level, E_F, with respect to the tip. Adapted from [23].

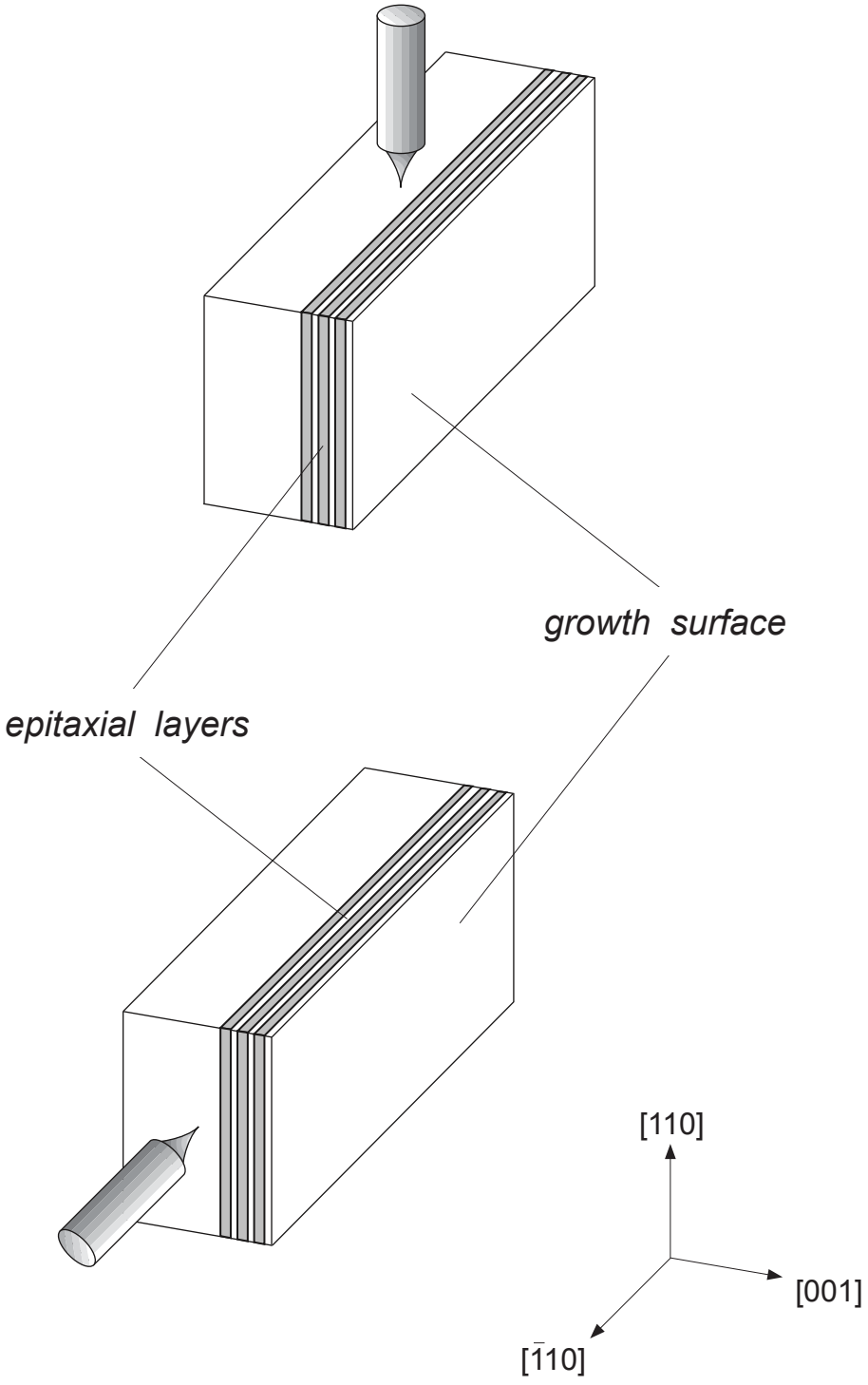

FIGURE 1.8. Illustration of cross sectional scanning tunneling microscopy. There are two non–polar crystal cross sections accessible for analysis with STM, (110) and ($1\bar{1}0$).

surface atomic geometry with the anions displaced slightly outward and the cations displaced slightly inward. An attending charge transfer leads to the cations becoming empty states and the anions becoming filled states, making atom–selective imaging possible with STM [25]; the cation or anion sublattices can be imaged separately by tunneling into or out of the sample.

Precise position control allows placement of the STM tip above a chosen set of superlattice periods. Once positioned over a region of interest, the tip is brought within a few angstroms of the exposed surface and a bias is then applied. A negative bias is applied to the sample to obtain images of the filled states corresponding to the top layer anions (such as arsenic or antimony), while a positive voltage images the empty states associated with the cation dangling bonds (such as indium or gallium).

As the STM tip scans the sample surface, the separation between tip and sample adjusts to keep a constant tunneling current (Fig 1.9). This constant–current contour mirrors the surface local electronic density of states within the energy window available for tunneling [26, 27], which provides a "topographic" representation of the density of states, typically displayed as grayscale in STM images. The varying shades of gray in an STM image are influenced by two key factors. The first is electronic effects resulting from band edge energy shifts, along with deviations in the density of states available to participate in tunneling, displayed as layer contrast. The second factor arises from local surface morphology changes accompanying differences in local bond lengths due to isovalent impurities. These changes are readily apparent in the STM image of a type–II InAs/GaSb superlattice (Fig 1.10) with geometrical perturbations in the local surface

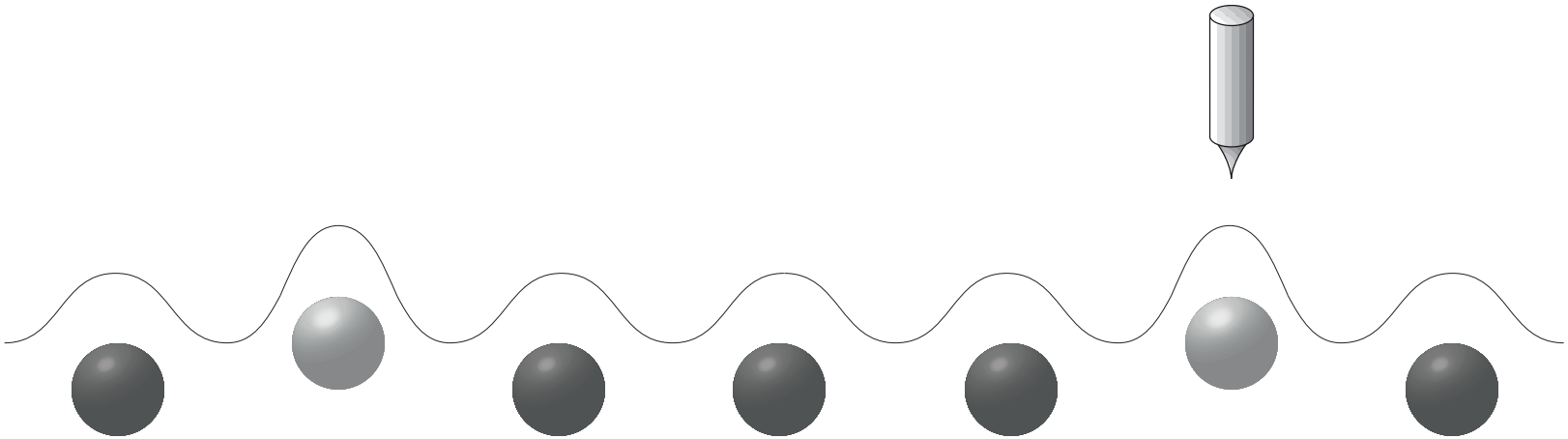

FIGURE 1.9. Schematic illustrating adjustments to the separation between the STM tip and sample to maintain a set tunnel current – and a fixed local density of states – over a surface with two, distinct bond lengths. Longer bond lengths will lead to a brighter appearance, and shorter bond lengths a darker appearance, in typical grey–scale STM images. Adapted from [23].

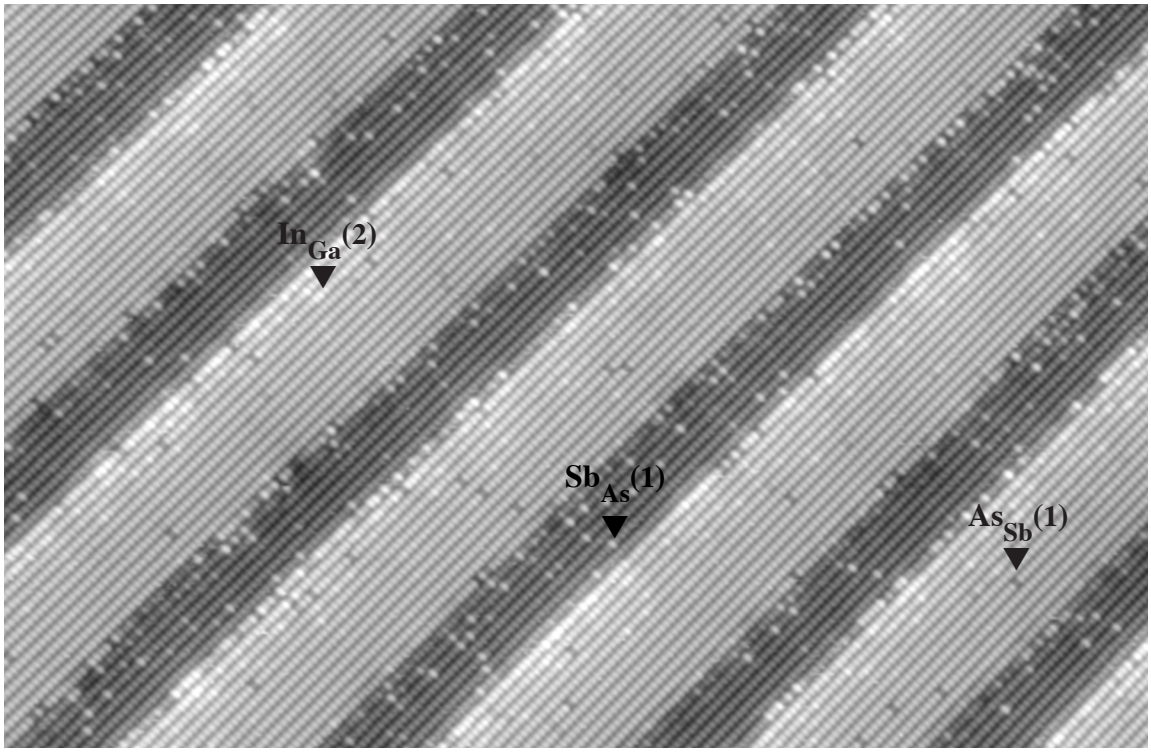

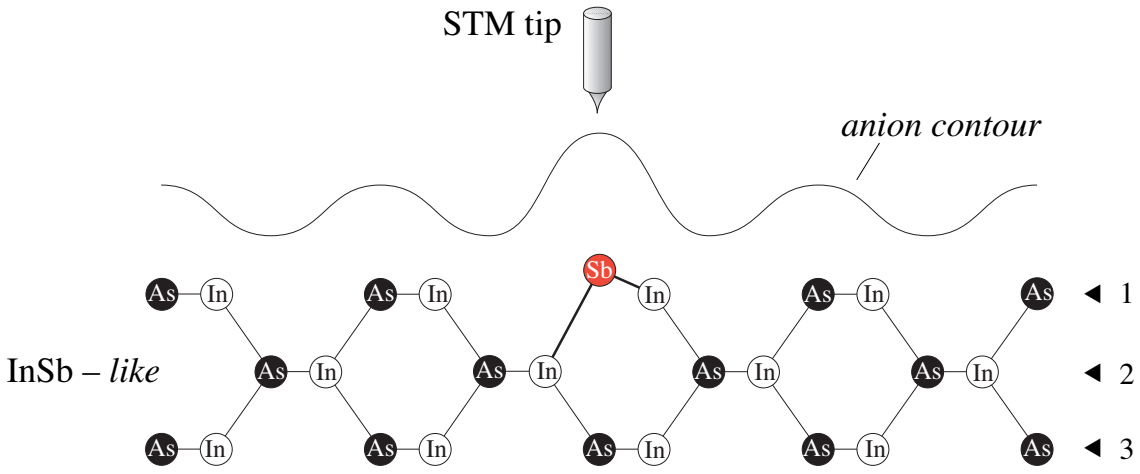

FIGURE 1.10. Atomic–resolution STM image of the anion sublattice (Sb, As) for a type–II InAs / GaSb superlattice. Isovalent impurities are indicated by carets in the image. The lower schematic illustrates the change in current contour as the tip encounters a change in surface topography. Growth direction is from top–left to bottom–right.

morphology indicated by carets. Every feature can be atomically resolved and the entire structure can be characterized based on these real–space observations.

Dissertation Overview

The remaining chapters of this manuscript are devoted to: a discussion of the changes made to the UHV system to provide a contamination–free environment for freshly cleaved samples, optimization of the experimental procedures and protocols employed to produce reliably flat cleaves, a brief overview of well–known non–idealities exhibited by tripod scanners, and standardized lab protocols to minimize the undesirable effects of these deficiencies during data acquisition; a cross–sectional STM study of the antimony distribution in an InAs/InAsSb superlattice and reconstruction of the monolayer–by–monolayer antimony fraction in a representative bulk period; development of a quantitative segregation model to fit the observed antimony profiles together with examination of the resulting fit parameters and what they tell us about segregation in InAs/InAsSb superlattices; and, finally, discussion of a novel reciprocal–space technique that transforms cross–sectional STM into a precision tool for measuring the vertical evolution in local superlattice periodicity anywhere along a multilayer stack.

CHAPTER II

EXPERIMENTAL SETUP

UHV System Reconditioning

The experiments in this study were performed using a commercial STM manufactured by Omicron Vakuumphysik [28]. Our microscope resides in an ultra high vacuum (UHV) chamber (Fig. 2.1, right) which provides an *in–situ* environment for cleavage and subsequent examination of semiconductor surfaces (Fig. 2.1, left) without atmospheric contamination. Details regarding the design and construction of this setup are described in dissertations of prior students [29, 30].

The partial pressures in our main vacuum chamber are at or below $1x10^{-13}$ Torr for all species, except hydrogen, which is close to $1x10^{-11}$ Torr. These near–extreme high vacuum (XHV) conditions are the result of an extensive and laborious overhaul of the inherited vacuum chamber, led by fellow lab member Federico Lopez Cruz, and carefully documented in his dissertation [23]. This upgrade was made in response to a quantum cascade (QC) superlattice containing a highly–reactive Al–bearing material. Freshly cleaved surfaces reacted quickly to the already low levels of residual gases in the original vacuum system, becoming contaminated with adsorbates within a matter of hours, such that analysis with STM was not feasible.

To reduce outgassing loads in the vacuum chamber, we removed all unused components from the system, replaced the pumps with newer and more efficient models, and installed a new transporter rod. The main vacuum chamber following modifications

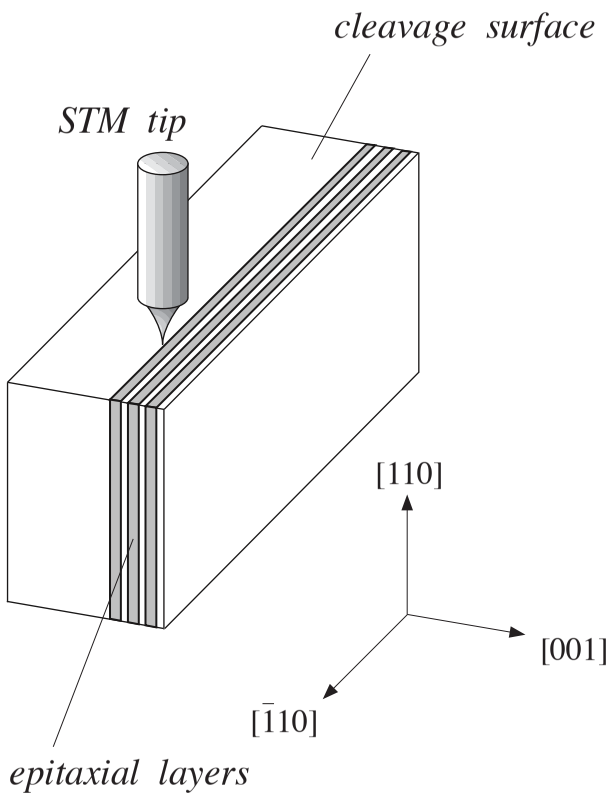

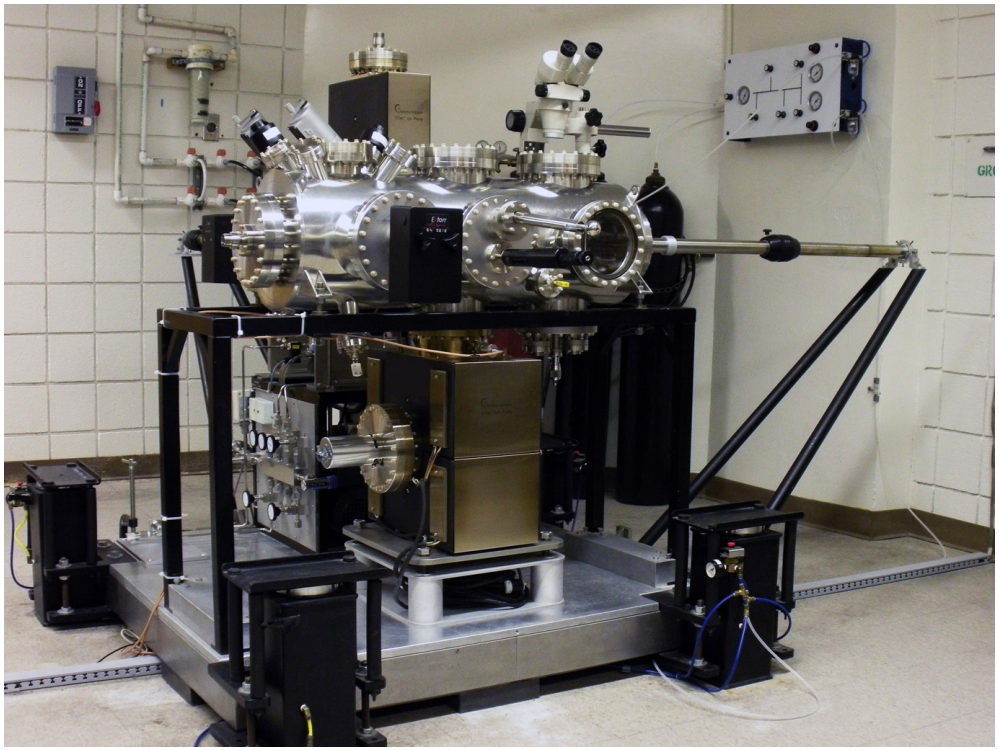

FIGURE 2.1. Illustration of the crystal cross sections accessible via in–situ cleavage (left), alongside the dedicated UHVchamber (right) where the scanning tunneling microscope resides. Reprinted with permission from [23].

is shown in Fig. 2.2. Another piece of instrumentation contributing the gas load in the main chamber was the cleaving–stage carousel. Historically, following cleavage of a sample, the carousel had to be rotated for the cleaved surface to face the STM tip; this actuation produced outgassing that can have an adverse effect on freshly–cleaved surfaces. To avoid this rotation and its accompanying release of gases, a change to the sample mounting was made. By moving the mounting pieces to the reverse side of the symmetric platen, sample dies can now be cleaved in the carousel already facing the tip (Fig. 2.3).

Attached to the main chamber via a series of valves is a pair of chambers that serve as the load lock and transfer chamber for introduction (and retrieval) of samples and tips to (and from) the main chamber. This entry system underwent an extensive redesign due to an unintentional cadmium contamination, but the reconstruction led to improved pumping speeds and decreased gas loads. Fig. 2.4 shows the current setup of the entry chamber.

State–of–the–art residual gas analyzers (RGA) [31] were installed in the entry and main vacuum chambers to provide important monitoring of gas partial pressures and enable early detection of any possible future contamination. Near–XHV pressures are highlighted by the RGA data of current levels of reactive species (Fig. 2.5, left). With these existing vacuum conditions, a freshly cleaved surface will remain contamination–free for several days, up to a few months, as illustrated by the plot of the monolayer formation time for a reactive species, assuming ideal circumstances, in Fig. 2.5 (right).

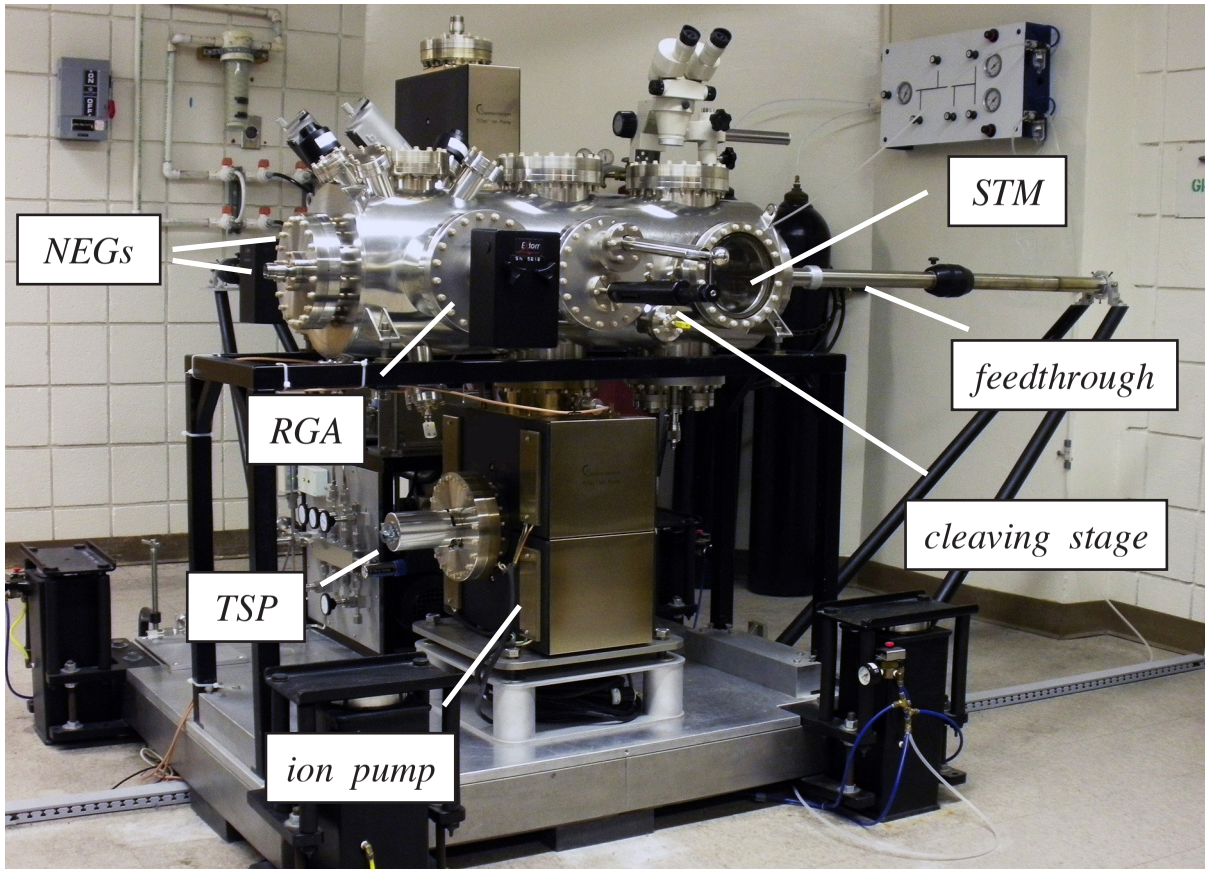

FIGURE 2.2. Front view of the upgraded UHV system (ca. 2008) highlighting major reconditioning to the main vacuum chamber. Newer, more powerful vacuum pumps and a new smoothly actuated linear feedthrough were installed in the main chamber to provide a suitable habitat for freshly cleaved Al–rich surfaces. Vacuum improvements were monitored with a new electron–multiplier enhanced RGA. Reprinted with permission from [23].

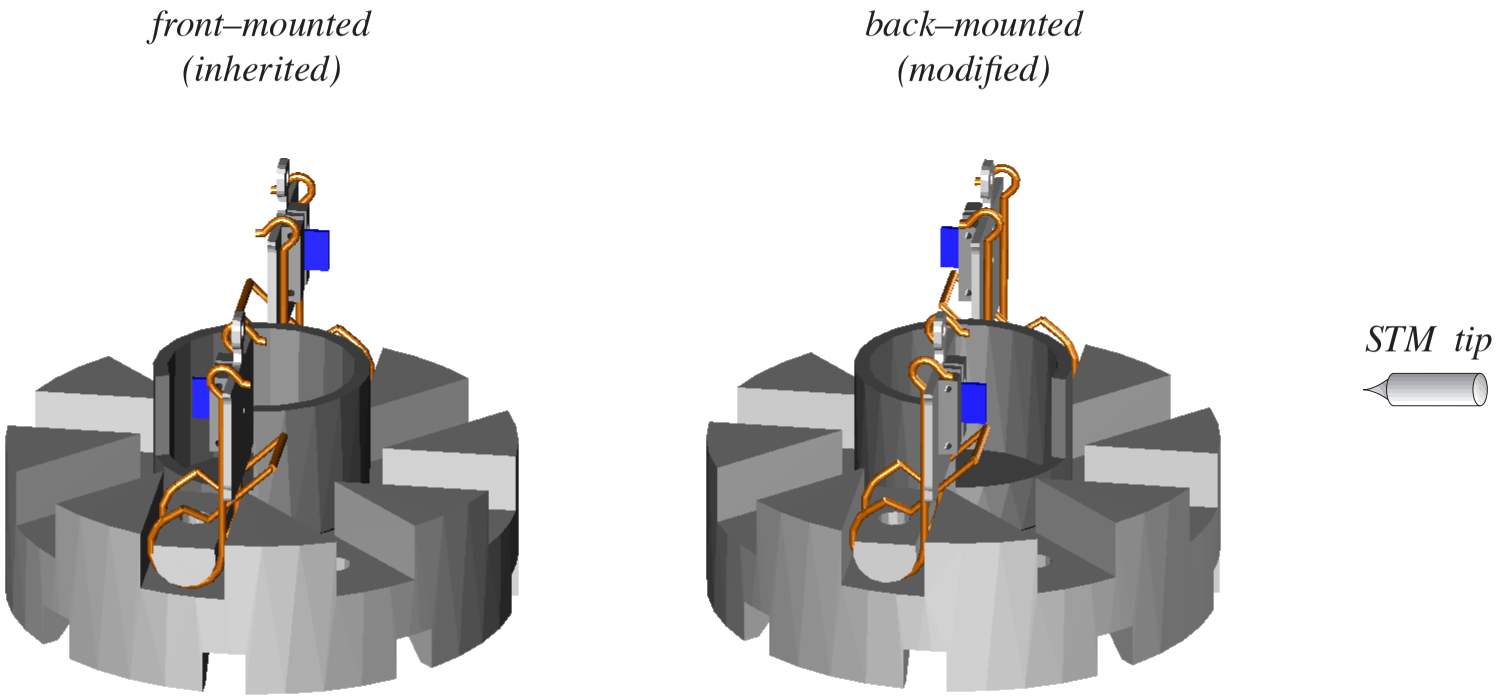

FIGURE 2.3. Traditional fastening of notched, sample dies to the front of an STM platen (left) entails carousel rotation – with its attendant pressure transient – following cleavage for the sample surface and STM tip to face one another. Fastening these dies to the back of the symmetric, STM platen (right) circumvents any need for carousel rotation, since cleavage surface and STM tip are naturally aligned.

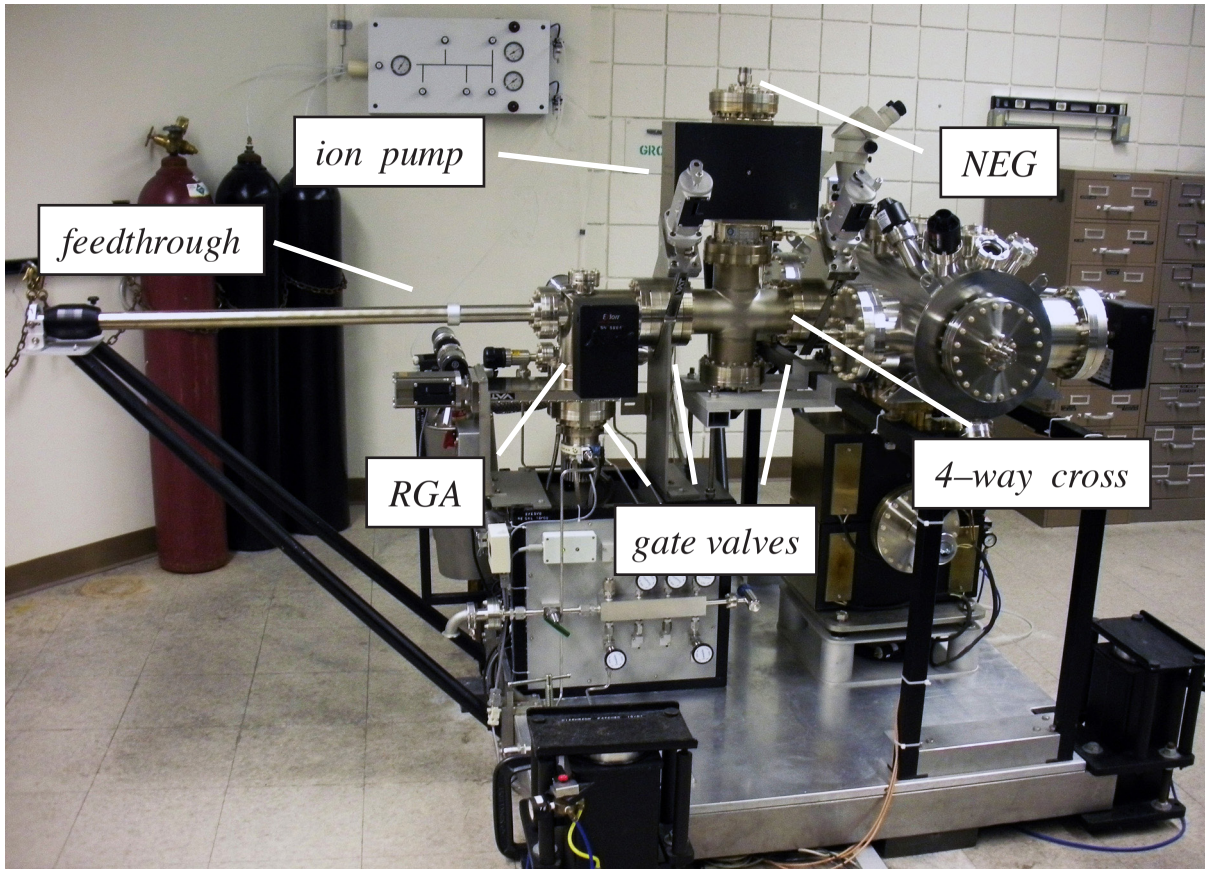

FIGURE 2.4. Side view of the upgraded UHV system (ca. 2008) highlighting major reconditioning to the load lock and transfer chamber. Vacuum pumps, gate valves, and the linear motion feedthrough were all replaced with newer, high–performance components; a dedicated RGA was added to the sample load lock. Stainless–steel tubulation increased from 2.75” to 4” OD minimum throughout. A simple, 4–way cross serves as a transfer chamber. Reprinted with permission from [23].

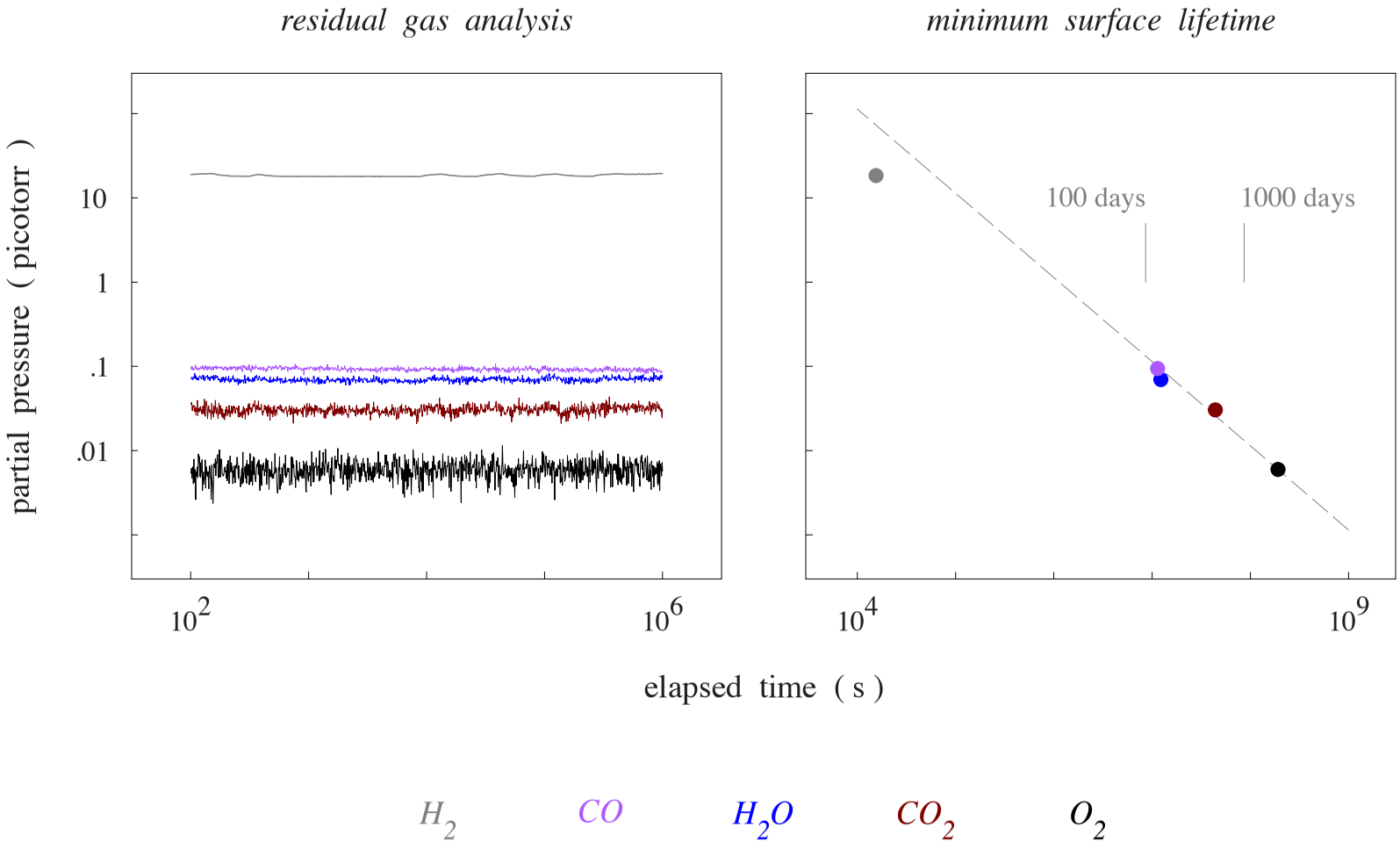

FIGURE 2.5. RGA partial–pressure analysis illustrating steady–state XHV conditions achieved with the upgraded UHV system (left) and associated (minimum) monolayer–formation times under ideal circumstances (right). Adapted from [23].

Another technical aspect important for STM analysis is the vibration isolation. The vibration isolation is needed to obtain atomic resolution data with the STM. The vacuum system sits on a stainless steel table supported by four air piston legs, or Gimbal Piston isolators, commercially available through TMC [32]. Each isolator utilizes two air chambers for damping, along with a specially designed piston and piston diaphragm to provide vertical and horizontal isolation. Seismometer measurements indicated that the vibration isolation provided by the air legs had decreased since the system was originally assembled two decades earlier (Fig. 2.6). To remedy this, we disassembled the Gimbal piston isolators in order to replace the pistons and piston diaphragms, and updated the tubing and valves that control flow to the air chambers for improved isolation (Fig. 2.7).

Sample Cleavage Optimization

For cross–sectional STM a smooth flat cleavage surface is key, as well as the ability to produce such as result in a reliable manner. The original cleaving protocols were developed while studying superlattices grown on GaSb substrates, and while former students were able to obtain successful cleaves, it could take several attempts before getting an acceptable cleave for analysis. In order to create a reliable set of cleaving parameters to minimize material waste, we systematically explored each parameter of the original cleaving protocol to determine the optimal cleaving conditions

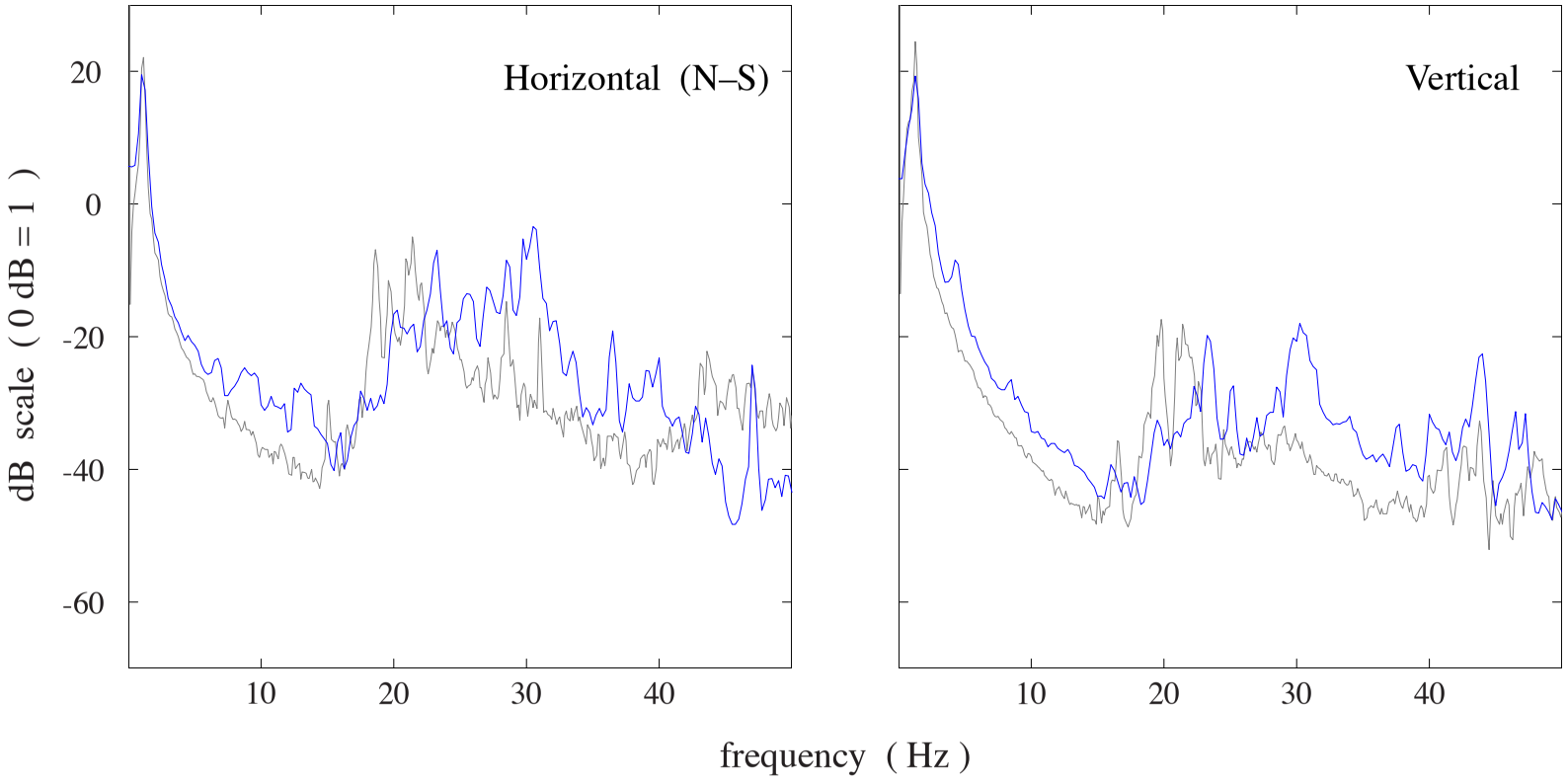

FIGURE 2.6. Plots comparing seismometry data from 1993 (grey) and 2010 (blue) with original piston assembly. The measurements from 2010 highlighted the need for replacement of the piston diaphragms.

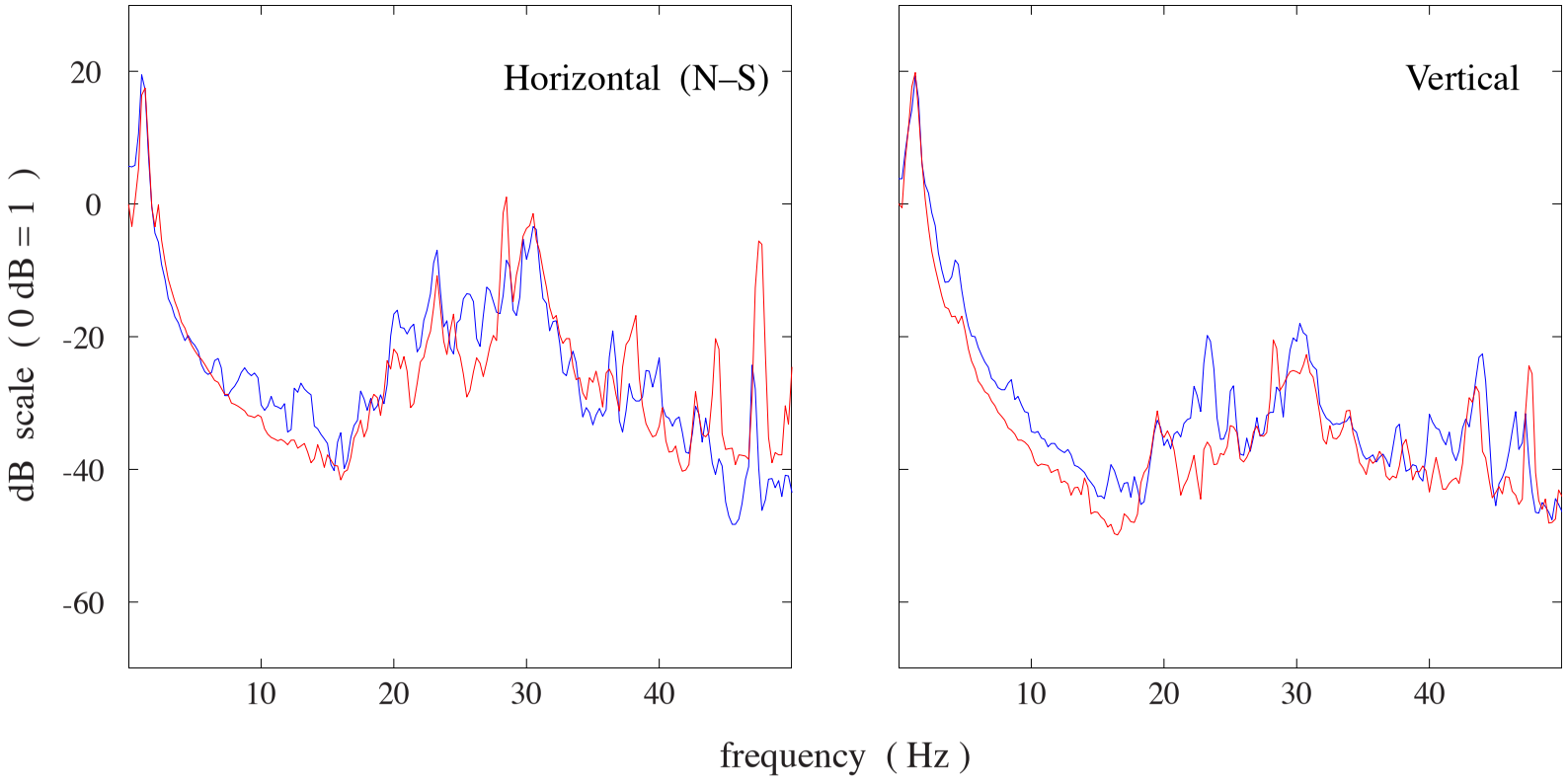

FIGURE 2.7. Plots comparing seismometry data from 2010 (blue) original piston assembly with 2011 (red) new piston assembly. The measurements from 2011 highlight the improvement following replacement of the piston diaphragms.

for GaSb substrates[1], which is the same substrate material used for the structure examined in this study.

To aid improvement of the cleavage surface, we utilized a Zeiss Axiophot light microscope located at the Microscopy Imaging Center on TAMU campus (Fig. 2.8). The microscope is equipped for Nomarski differential interference contrast (DIC) microscopy. DIC or Nomarski microscopy [33, 34] is a method used to enhance the contrast in a variety of samples to distinguish features that are normally not visible with regular bright field light microscopy. A plane-polarized light enters a Nomarski prism[2], where it is split into two slightly offset beams of equal intensity. The beams illuminate the sample through the microscope objective and the light reflected off the sample surface is collected by the same objective. Upon passing through the Nomarski prism for a second time, the beams are co-aligned and then impinge on a polarizing filter (analyzer) where they are able to interfere. An interference pattern generated from the recombination of the two beams is a result of their optical path difference (OPD). Thus, small surface height variations can be visualized with good contrast. The resulting DIC image has a false three-dimensional relief appearance, with variations in brightness corresponding to the first derivative of the OPD changes on the surface. DIC is a qualitative technique, i.e., surface changes can be detected, but height or OPD cannot be measured quantitatively, because the same brightness in the image may result from two

[1] These parameters were also examined simultaneously for InP substrate, described fully in reference [23].

[2] The Nomarski prism is a modified Wollaston prism.

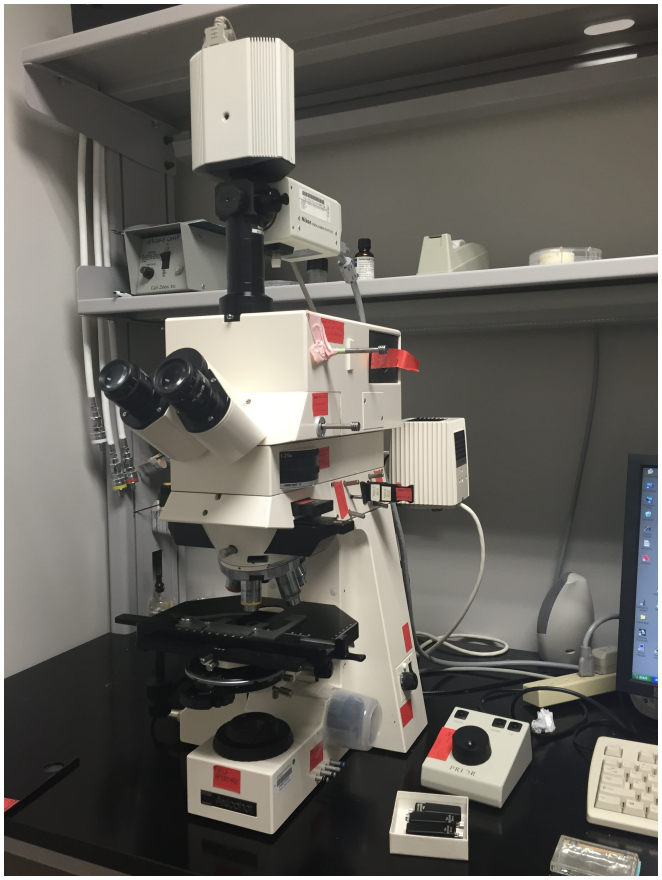

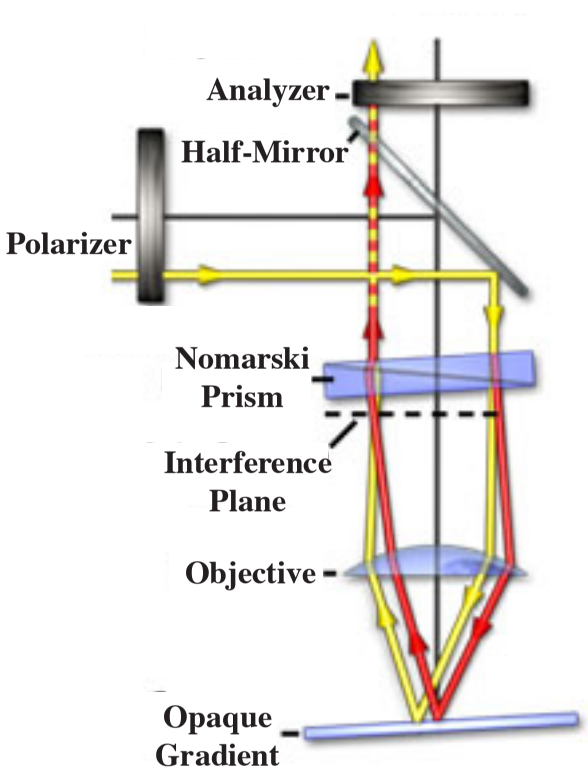

FIGURE 2.8. A Zeiss Axiophot light microscope equipped for Nomarski DIC microscopy provides enhanced contrast to discern faint details on a sample. The schematic on the right illustrates the path of the polarized light in the DIC setup.

OPDs that differ by one wavelength. Employing Nomarki to image freshly–cleaved surfaces (Fig. 2.9) provides contrast detail of features not visible with a standard lab light microscope, aiding improvements to the cleavage protocols.

To begin our exploration of the cleaving protocol, we examine the steps involved in preparing a piece of the sample wafer for cleavage. We use an ESI laser trimming system, also referred to as a laser scriber, which is equipped with an NdYAG laser and several mirrors to direct the laser beam from its source to the stage where the wafer is placed for scribing (Fig. 2.10). A substrate wafer is cut into several small 5.08mm x 5.08mm squares with the laser scriber, aligning the edges of the squares with the major and minor flats of the wafer. Once these dies have been cut from the wafer, the laser beam is used to scribe a vertically–centered notch on each, aligned with one of the wafer flats, which aids cleavage by initiating a fracture process to reveal a specific crystal plane, either (110) or (1–10), as illustrated in Fig. 2.11.

Surprisingly, the laser path direction when notching the die (Fig 2.12, left), as well as the length and depth of the notch (Fig. 2.12, right), affect the quality of the cleavage surface. Historically the notch was made by rastering the laser from the edge to the center of the die; following several tests we found reversing the direction of the laser (center to edge of die) noticeably improved cleaves. To control the length of the notch, the user simply specifies a number of steps for the laser scriber stepper motor. Changes to the notch depth are more complicated as it is determined by a combination of beam parameters and material properties. Some of these are known, such as the wavelength of the laser, and the optical and thermal properties of the substrate wafer, while some

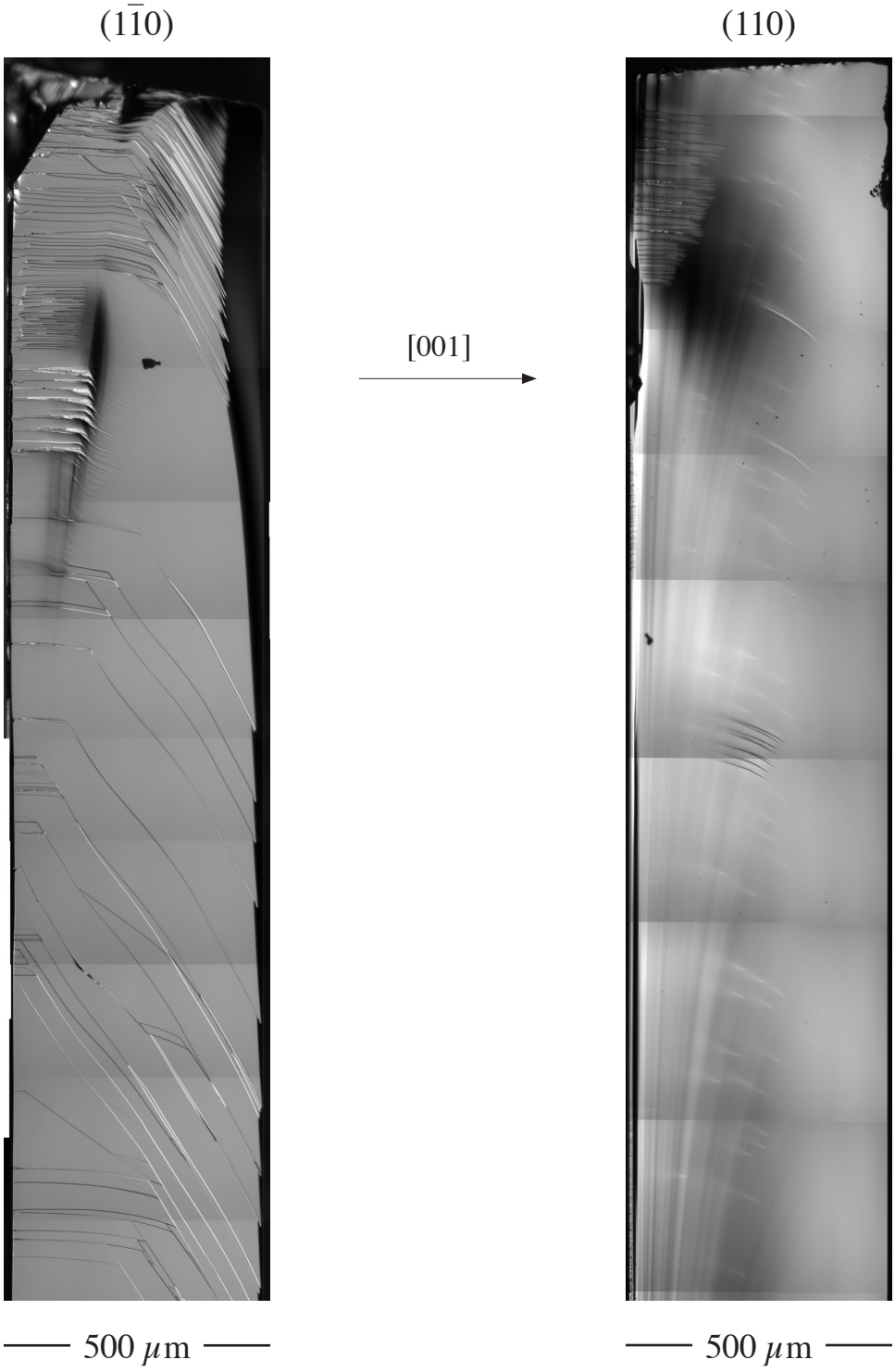

FIGURE 2.9. Nomarski micrographs exhibiting typical cleavage results achieved for GaSb substrates in either (110) (right) or (1$\bar{1}$0) (left) cross sections when employing inherited cleaving protocols. Growth direction is from left to right.

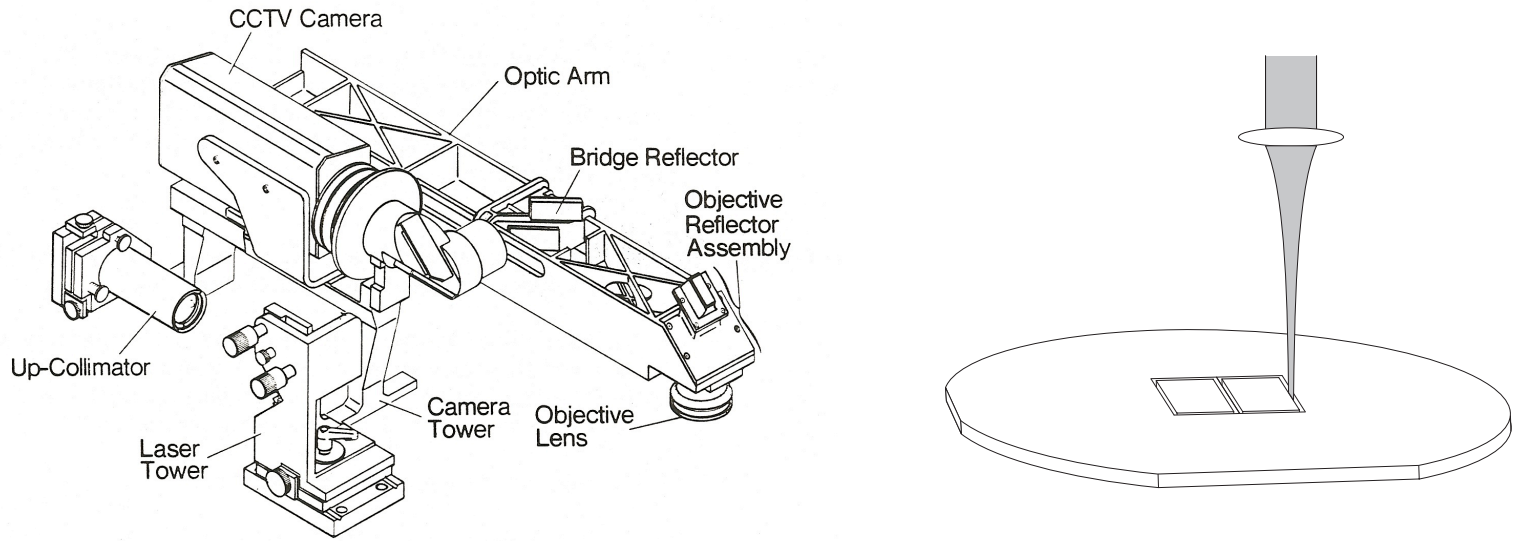

FIGURE 2.10. An ESI laser trimming system is used to scribe sample die for STM. A schematic of the path of the laser beam is shown on the left, and illustration of how die are scribed from a wafer on right.

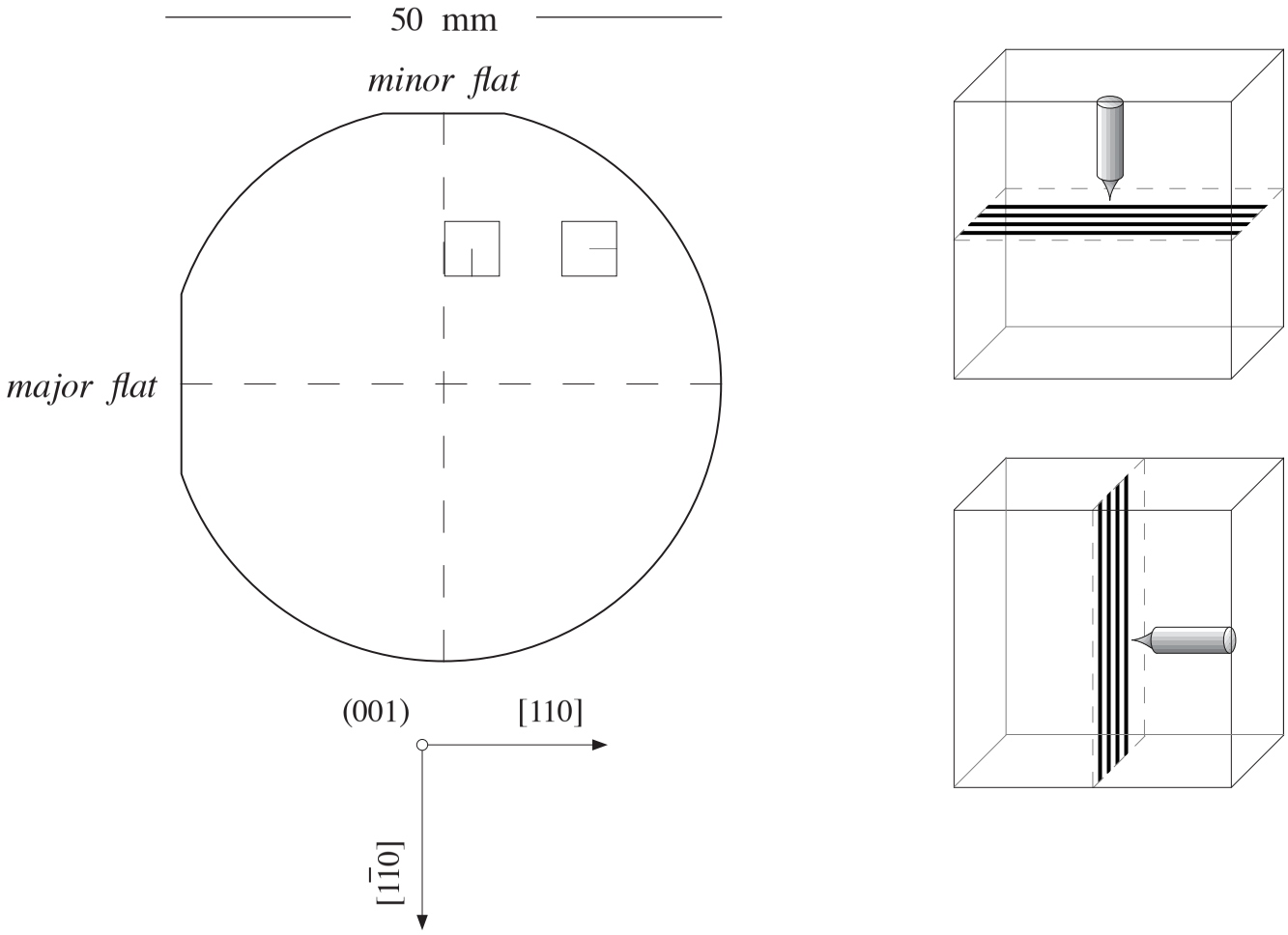

FIGURE 2.11. Schematic illustration, left, of a commercial semiconductor wafer with crystal planes indicated by conventional major– and minor– flats. A small notch aligned with the corresponding crystal axes directs the fracture process. On the right, an STM tip is shown as if rotated to probe the exposed epilayers in orthogonal cross sections; in reality the tip remains fixed while the sample is rotated according to the desired cross–section. Reprinted with permission from [23].

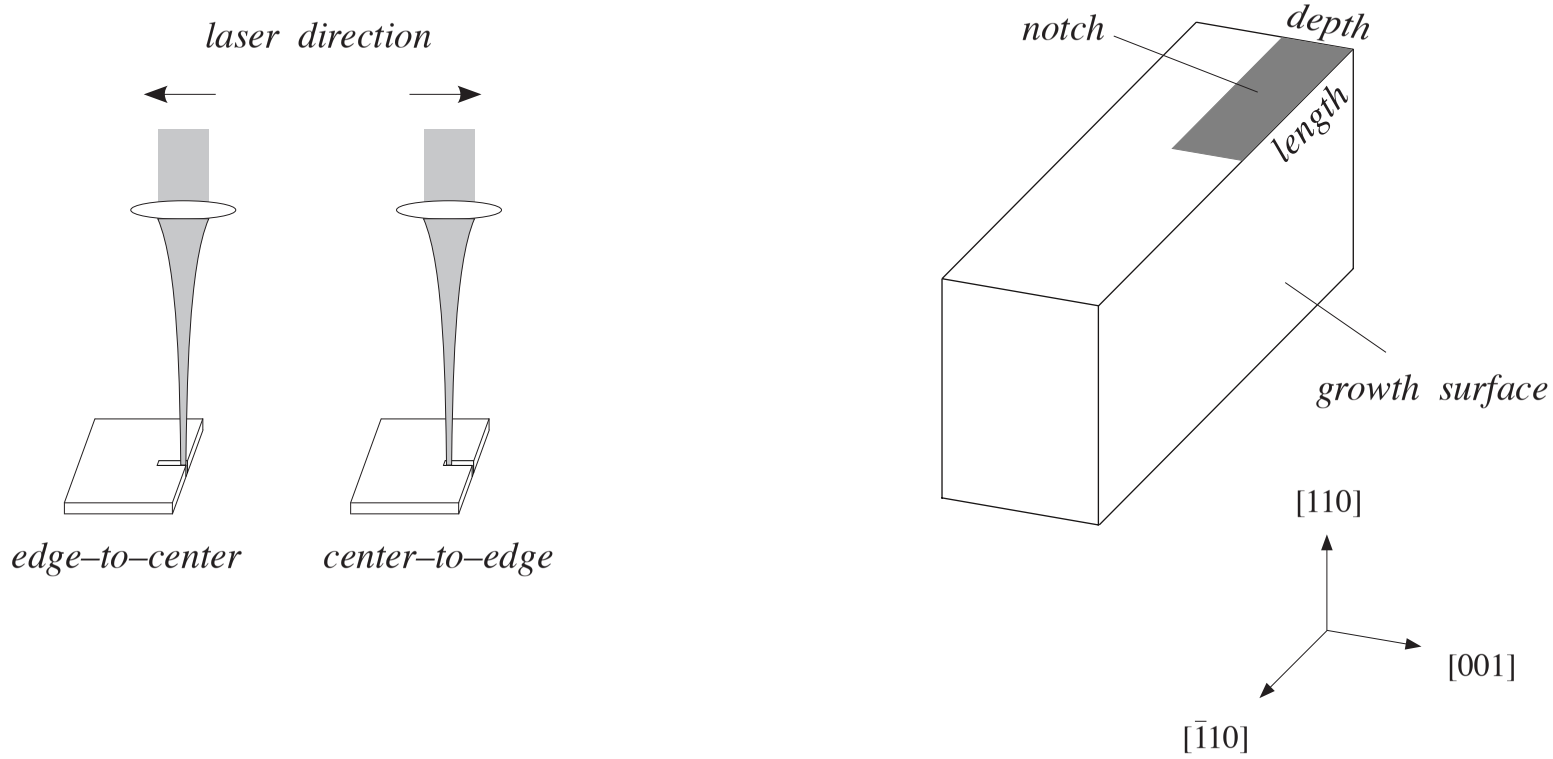

FIGURE 2.12. Illustration of the movement of the laser when scribing the notch (left), and a rotated and exploded view (right) of exposed substrate notch morphology (in cross section) following sample–die cleavage. Scribing direction, notch length, and notch depth are important factors affecting the fracture process during cleavage; the two former are relatively easy, and the latter comparatively difficult, to control. Adapted from [23].

parameters are fixed such as the beam profile; therefore, only the beam power and dwell time were modified.

The power of the beam is controlled by adjustments to the input current to the laser. Once the optimum setting was determined, the power remained fixed while the dwell time was adjusted by specifying a time per step for the stepper motors. The optimal resulting notch length for cleaving GaSb is in the range of 1.7 – 1.8 mm and the depth is in the range of 160 – 172 μm (or 30% of the GaSb substrate).

After the sample dies are scribed and notched according to the desired cleavage plane, they are cleaned with a standard degreasing method – ultrasonically soaked in acetone followed by ethanol. Each die is then mounted in a specially–designed sample holder (Fig. 2.13, left), which facilitate cleavage and subsequent analysis with cross–sectional STM. The die is held in place by a stainless steel anvil and clamp, and a beryllium–copper (Be–Cu) spring is placed between the clamp and a compression bar; a set of fastening screws keeps all pieces secure. The Be–Cu spring keeps the sample from being crushed by thermal expansion during vacuum bake–outs. Both the sample die and the Be–Cu spring were previously centered between the screws, but cleave tests revealed changing the placement of the sample and spring could improve the quality of the cleaved surface. The best results were produced with the die positioned low in the sample holder next to the bottom screw, and the spring asymmetrically raised towards the top screw.

To expose the superlattice structure in cross section, the die must undergo an impact from the cleaving rod. Historically, samples were cleaved by manual actuation

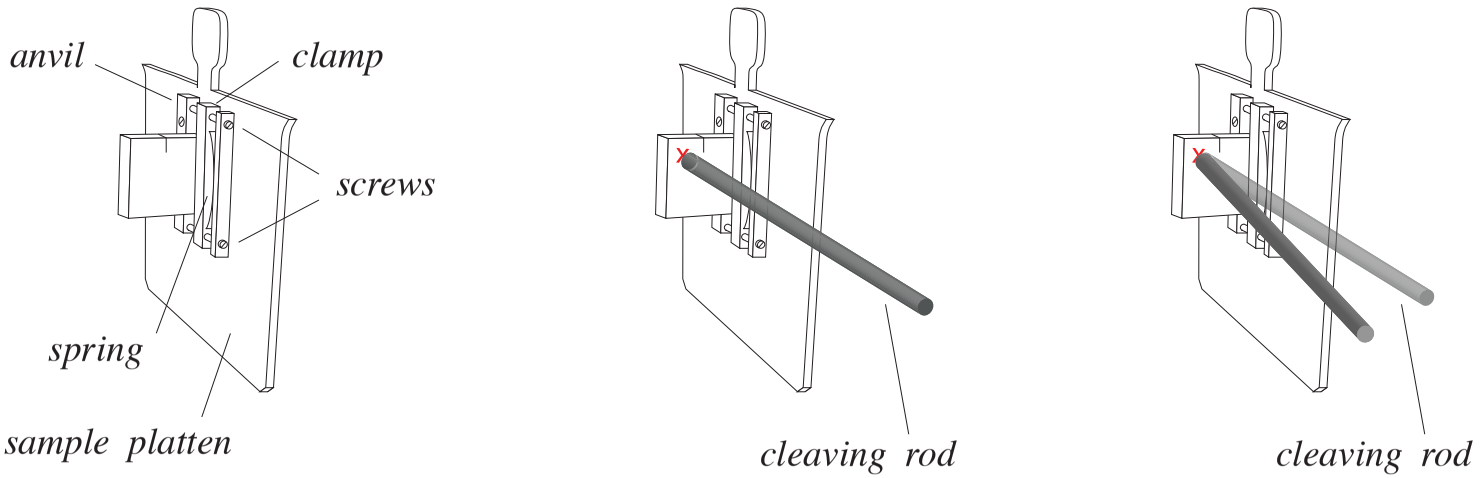

FIGURE 2.13. Schematic illustrating sample mounting, impact location, and impact angle. Adapted from [23].

of the cleaving rod, so that the speed at which the samples were impacted varied based on the user. By adjusting the setup to allow for pneumatic actuation [35], this inconsistency is removed, ensuring reproducible results. To make the cleave test process more efficient, we set up an atmospheric cleaving stage (Fig. 2.14) mirroring the setup used inside the vacuum system. This allowed us to study the effect from each change of parameters more quickly by avoiding the time drain of introducing samples to the vacuum chamber and their subsequent retrieval following cleavage. The most effective location of impact (Fig. 2.13, center) was determined to be the upper right–hand corner of the die. We also found the angle at which the cleaving rod impacts the sample (Fig. 2.13, right) affects the quality of the cleavage surface for GaSb substrate. The (110) cleavage plane favors an impact perpendicular to the die surface, while (1–10) seemed to favor an angle slightly less than 90 degrees.

Another important element to consider is the speed at which the cleaving rod impacts the sample die. A commercially available USB accelerometer [36] was attached to the handle of the actuator to monitor the linear acceleration as a function of time. Integration of the data provides the linear velocity of the cleaving rod, which can be converted to linear displacement with a second integration. Fig. 2.15 illustrates a plot of velocity versus displacement, where the X indicates the distance the rod travels to the die, providing the velocity at impact. Tests concluded speeds above 240 mm/s provide the best results for (110) GaSb cross sections, while speeds below 180 mm/s are optimal for (1–10) GaSb cross sections. The improvements to the cleavage surface are well documented with Nomarski, as highlighted in Fig. 2.16 for a (1–10) cleavage surface.

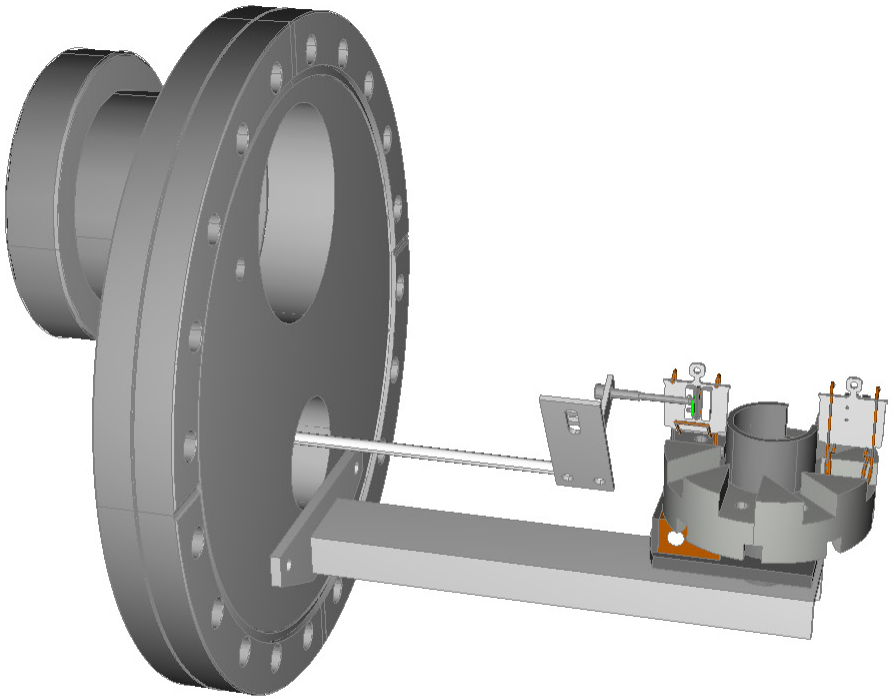

FIGURE 2.14 Schematic of cleaving stage assembled outside of vacuum to expedite improvements to cleaving protocols.

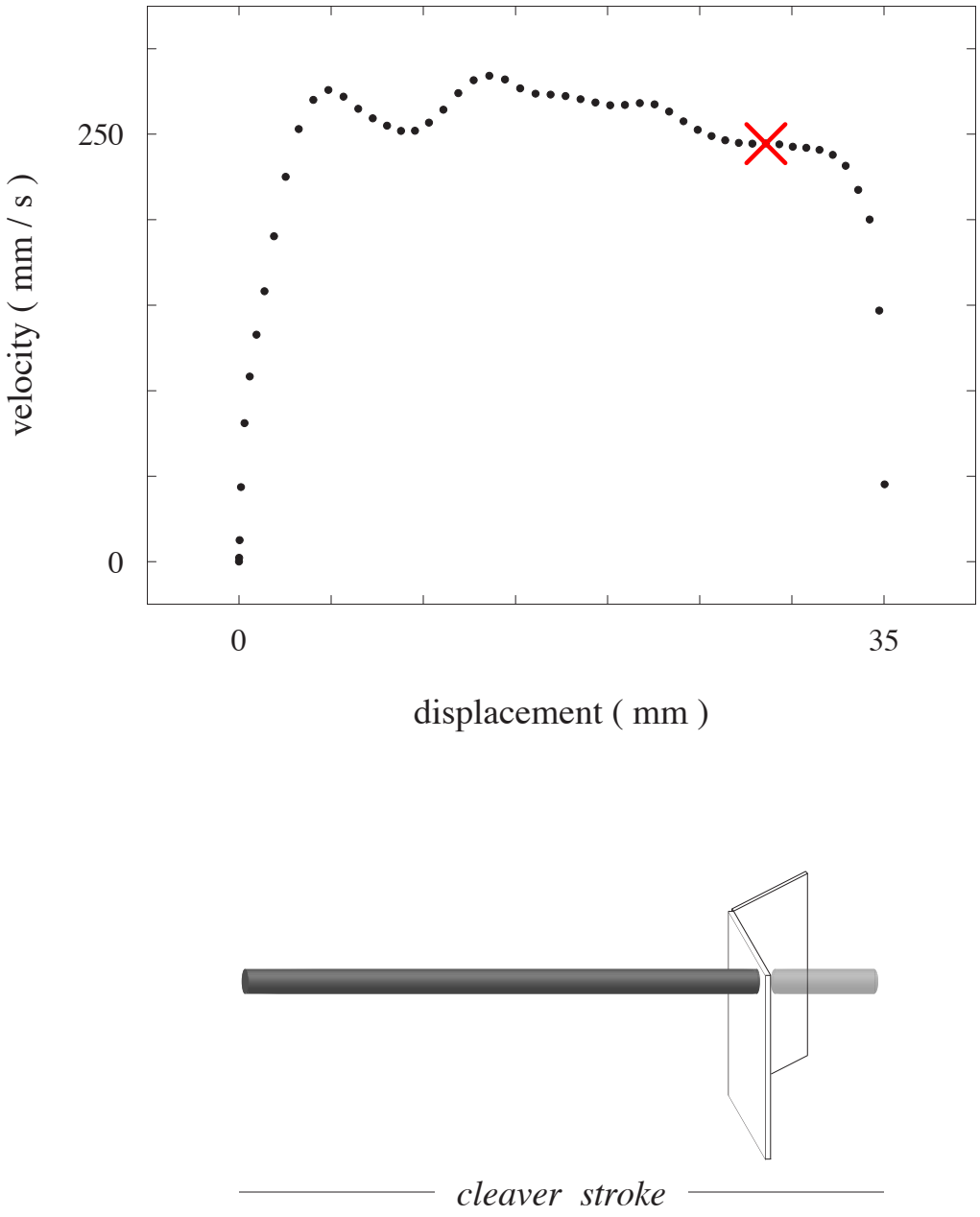

FIGURE 2.15. Pneumatically–actuated cleavage rod velocity versus displacement (top) with illustration of real–space stroke schematic (bottom). The velocity at impact (X) can be determined directly from this graph once the retracted–rod–to–sample distance is known.

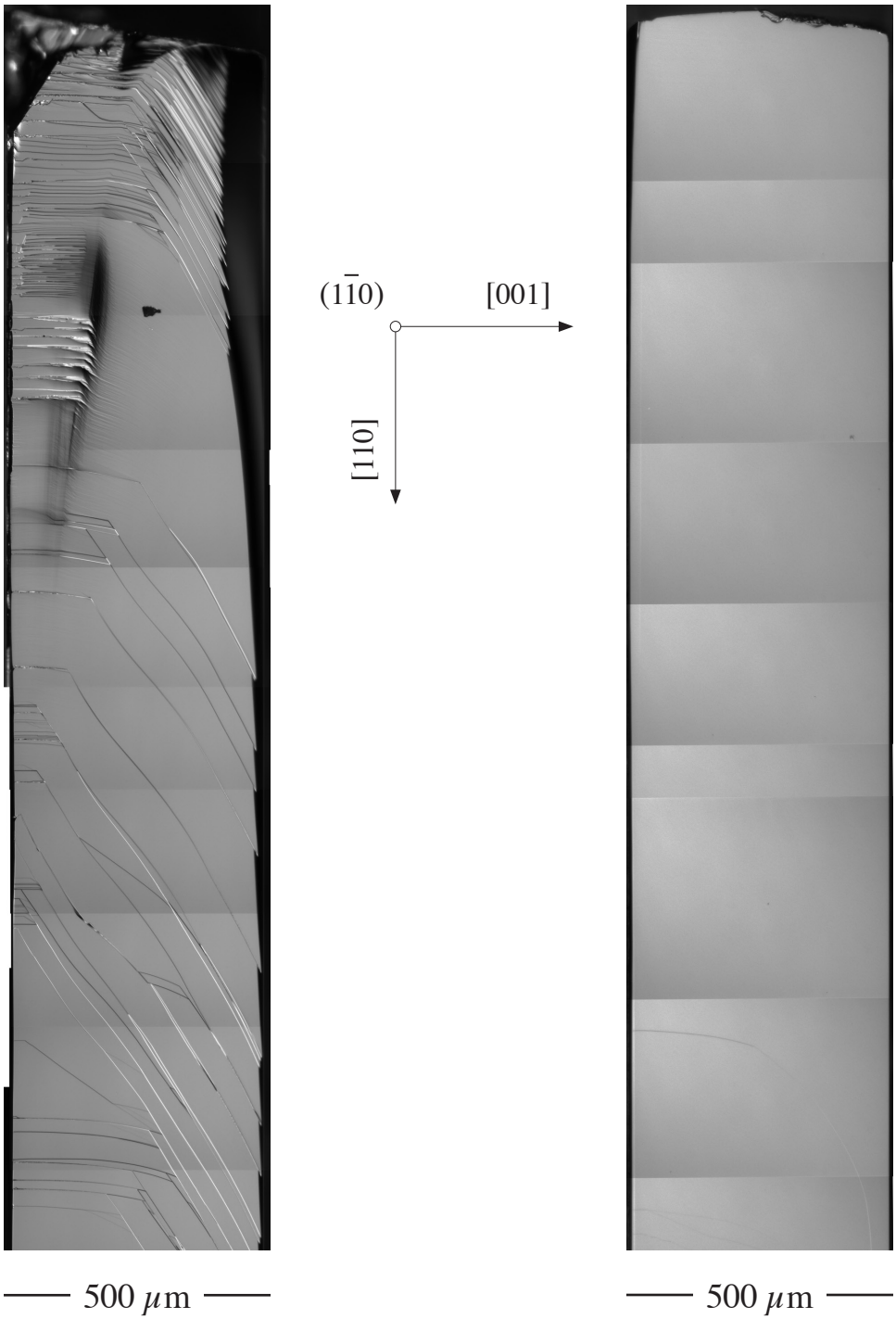

FIGURE 2.16. Nomarski micrographs highlighting (1$\bar{1}$0) GaSb facets obtained with inherited (left) and improved (right) substrate cleavage protocols. Similar results are obtained for (110) GaSb facets. Growth direction is from left to right.

Having successfully addressed the vacuum conditions and cleavage protocols, atomic–resolution images of the InAs / InAsSb superlattice can now be acquired. To image a freshly cleaved surface we need an atomically sharp tip. We use 0.2mm platinum–iridium (Pt/Ir) 80:20 wire, as platinum is inert and does not form an oxide[3] and the iridium provides the needed strength and stability for imaging. The tips are fabricated from the wire via an electrochemical etch process, which uses a CaCl2/H2O/HCl solution based on recipes reported in literature [37] and refined in the STM lab; a detailed description can be found in the Honors Thesis of Chad Sosolik [38]. Once several acceptable tips have been etched, they are placed in tip holders and held in place with indium solder. The tip holders are then placed in platens designed to allow transfer of the tips into the vacuum system and to the STM stage.

Instrumental Non–Idealities

As mentioned in Chapter I, the STM tip can be precisely positioned over any desired subset of layers in the growth stack for navigation in the <110> direction. Overlapping images along the desired periods are assembled to form large–area survey mosaics. Great care must be taken to obtain high quality atomic–resolution images, as the STM piezoelectric raster mechanism suffers from well–known non–idealities that affect data acquisition. These distortion processes are either temporal or instrumental in nature, both of which can be controlled to some degree. Generally, substandard STM

[3] In comparison to another common metal used to make tips, tungsten, which does form an oxide.

data acquisition leads to temporal distortion, but this can be easily modified. The piezoelectric ceramics actuating the STM stage allow for coarse motion to quickly find an area of interest. Following this repositioning, the stage will continue to drift in the same direction of the movement due to inertia (Fig. 2.17); to minimize any effects from this drift on image acquisition we typically allow for a settling time of a few hours, while scanning the area every few minutes to check the condition of the tip.

Once an area of interest has been found on the exposed epitaxial layers, a more suitable method of navigation is by way of fine offsets made to the x– and y–piezos of the tripod scanner, which controls the movement of the STM tip. The fine adjustment piezos in the tripod scanner are not exempt from non-idealities and extra care must be considered during navigation. The tripod scanner exhibits undesirable instrumental distortion effects such as piezo creep [39] and hysteresis [40], illustrated in Fig. 2.18. Hysteresis, or piezo nonlinearity, is a non–linear response of the piezoelectric ceramics to the scan voltage applied during operation, but can be worked around, as will be explained in Chapter V.

Piezo creep is a change in the piezo displacement (elongation or contraction) occurring after a change in the applied electric field to the piezo ceramics, which can appear as a bowing effect or whiplash at the start of an image acquisition. The y–piezo is particularly susceptible to creep as it is associated with the slow–scan direction of the tripod scanner. To minimize the distortion due to creep, the offset applied to the z–piezo to move the tip must be must be parallel, but in the opposite direction, to the slow–scan increment (Fig. 2.19).

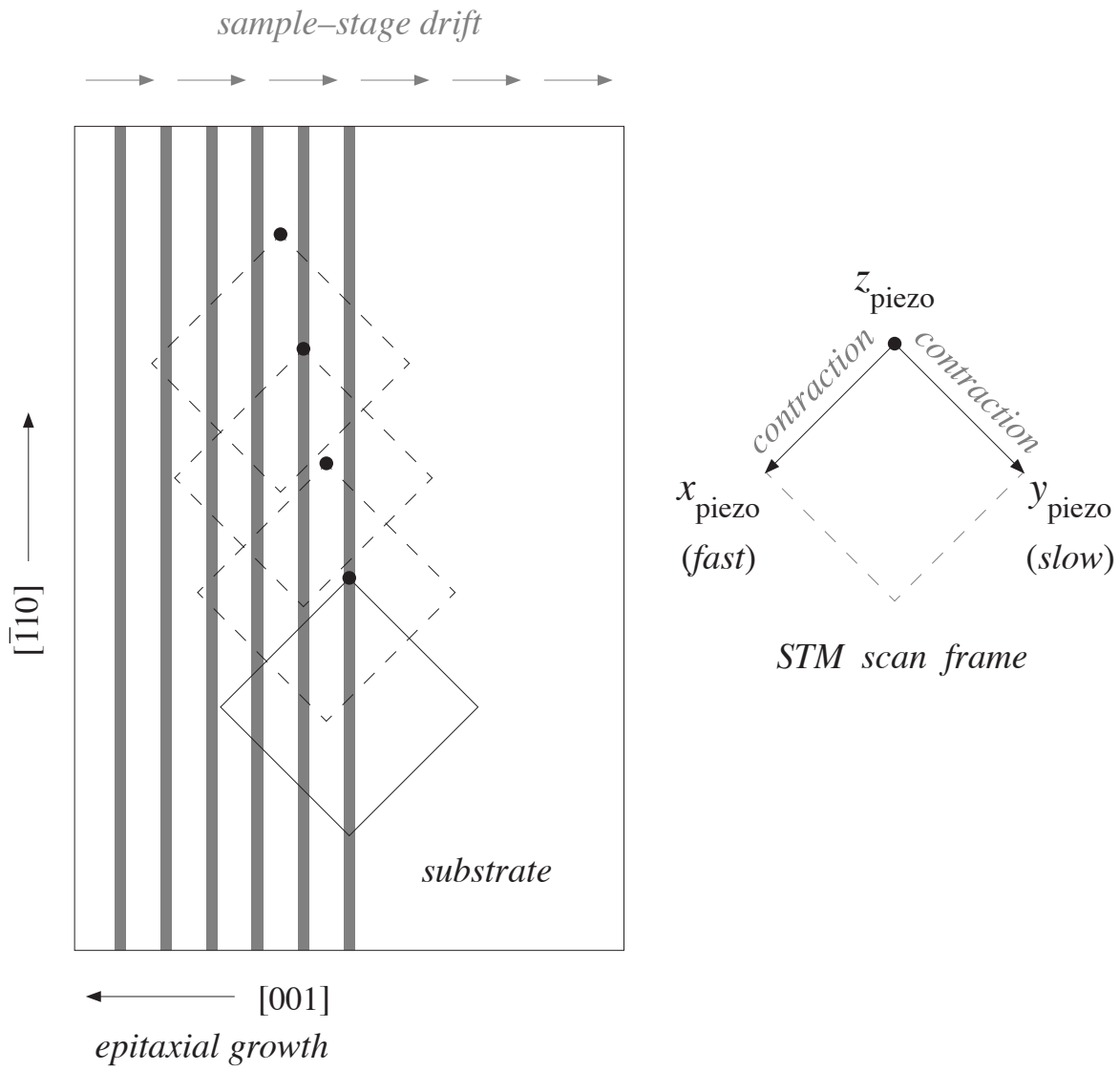

FIGURE 2.17. Schematic diagram (left) illustrates apparent drift of the STM scan frame due to piezo–inertia of the sample stage. This stage permits sample movement either left (in growth direction), or right (opposite growth direction) with respect to the tip. The induced drift typically requires several hours to settle. Also illustrated (right), contraction of the *x*– and *y*–piezos of an STM scan frame produce positive displacements. Cleavage plane coincides with plane of paper. Growth direction is right to left. Reprinted with permission from [23].

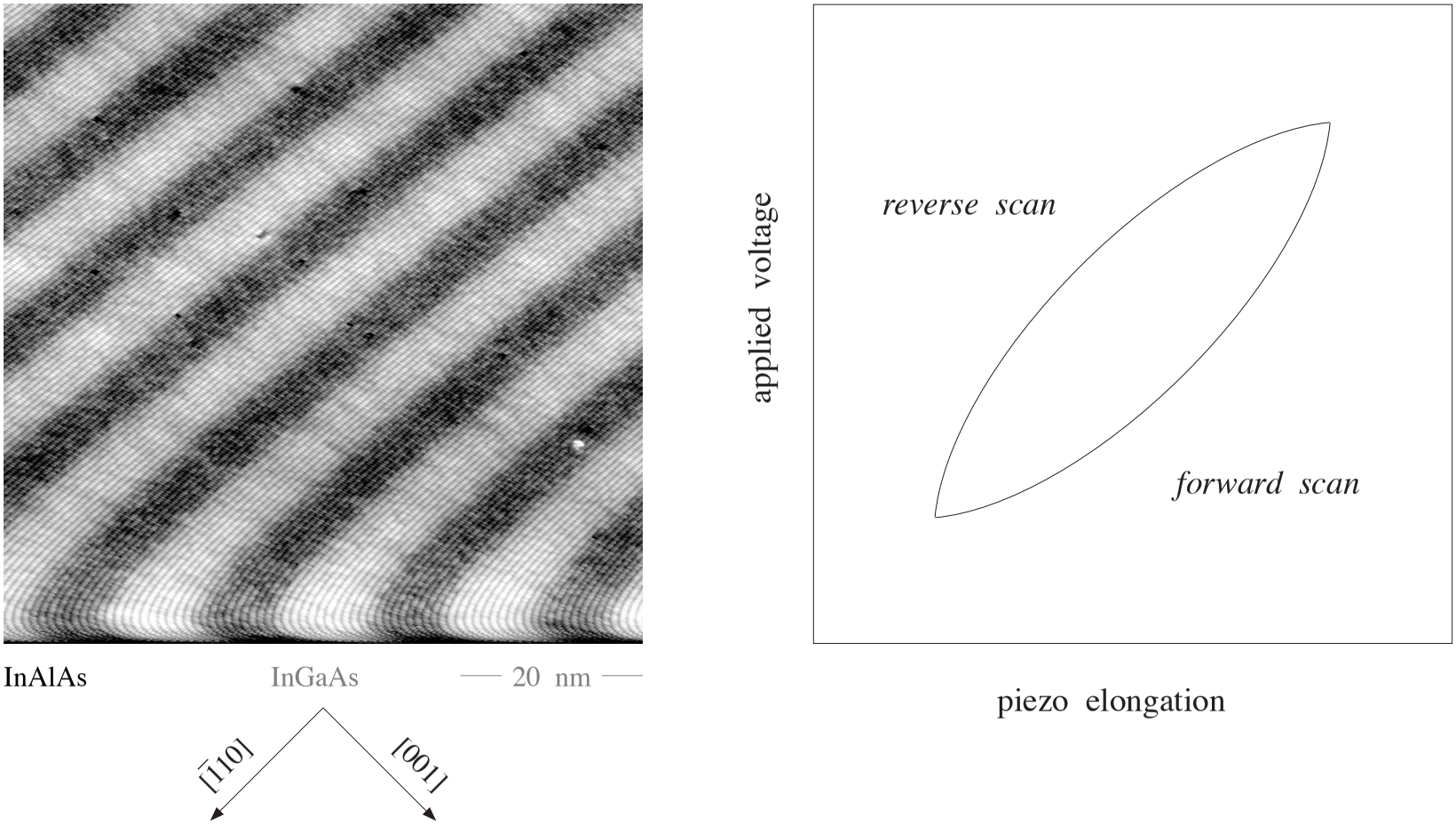

FIGURE 2.18. Typical non–idealities in piezo–scanners include piezo–creep (left) and hysteresis (right). Piezo–creep is visible here as whiplash in the bottom of the image; a subtler, but nevertheless undesirable symptom of piezo–creep also occurs throughout the image if the *y*–offsets are inadvertently taken to be parallel to the slow–scan direction. Piezo non–linearity (hysteresis) is, on the other hand, unavoidable; a workaround is to use a restricted area of the image where piezos are most linear in our current setup; further details explained in Chapter V. Reprinted with permission from [23].

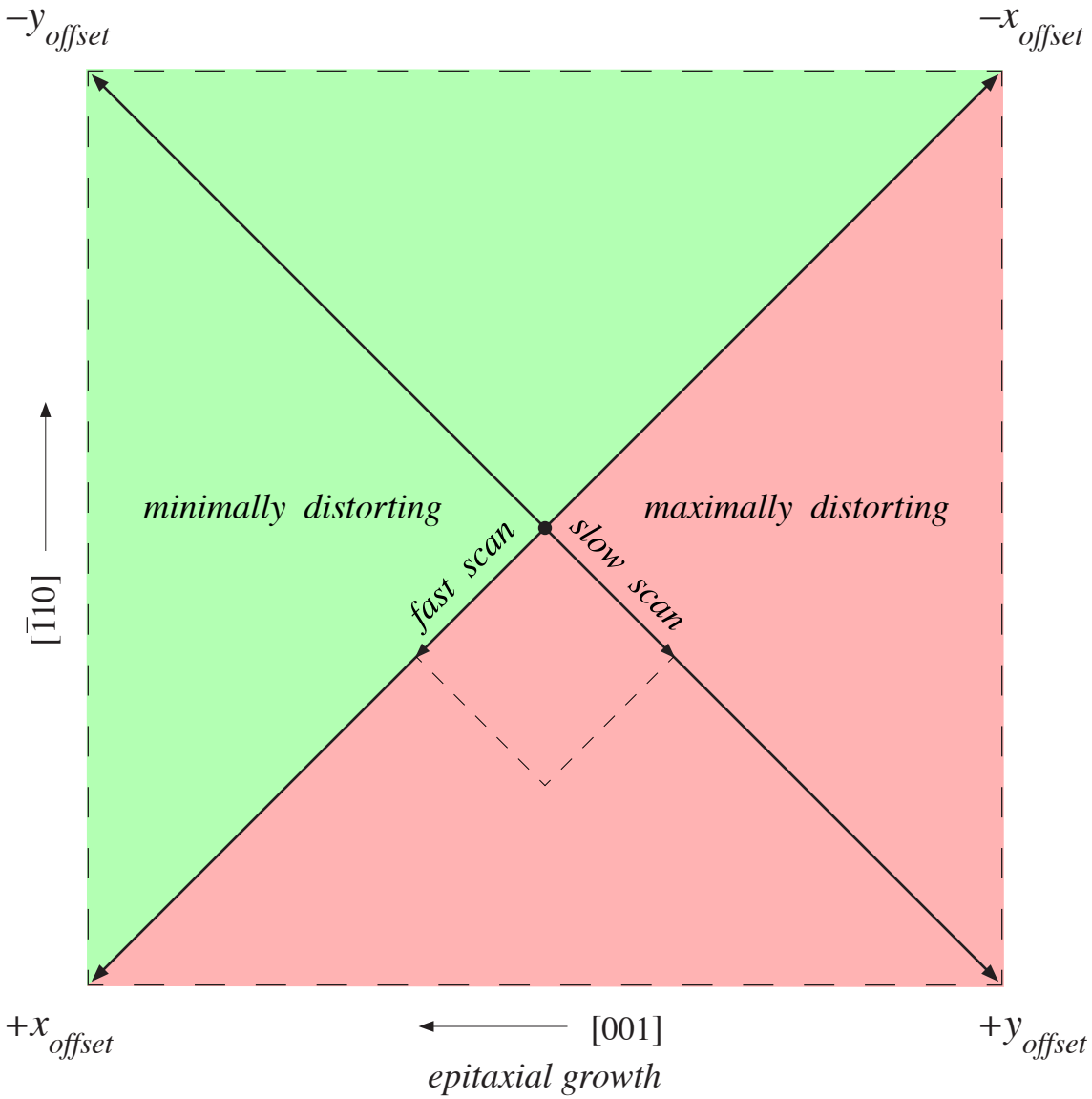

FIGURE 2.19. STM image frame located at the origin indicates fast– and slow–scan directions oriented along x– and y–piezo axes, respectively. This image frame can be precisely positioned anywhere within the one–micron–squared maximum area available to the tripod scanner with fine adjustment of the x– and y–piezo offsets. Minimally distorting zone corresponds to navigation routes that avoid positive increments of the y–piezo offset. Growth direction is right to left. Reprinted with permission from [23].

The x–piezo, fast–scan direction, is minimally effected by piezo creep due to its incremental motion – the ceramics contract in the forward direction and subsequently expand in the reverse direction; in comparison, the slow–scan increment is one–directional, always contracting. Piezo creep manifested as whiplash during the commencement of an image acquisition can be minimized by following an established procedure – start acquisition of an image, scan for 150 lines, end the scan, and discard the data, then repeat once more before starting a scan suitable for storage.

It is important to note these instrumental non–idealities will play a part in an analytical method to determine local superlattice periodicities to be discussed in Chapter V. The analysis discussed in Chapters III and IV is based on a counting method that is insensitive to these non–idealities.

Standardized Navigation Routes

Finally, taking into account the tripod scanner non–idealities, we established standardized navigation protocols for acquiring minimally–distorted data. Maintaining negative (anti–parallel) increments of the slow–scan piezo to minimize creep, the fast–scan piezo increments are chosen based on the direction of the desired survey. For a transverse survey exploring the entire multilayer stack from initiation to completion in the [001] growth direction, the applied increment to the fast–scan piezo will be negative; for lateral surveys navigating in the orthogonal [1–10] direction along a specific subset of layers from the stack, the piezo will have a positive increment.

An example of these navigation routes is illustrated in Fig. 2.20 by the device–scale surveys of an InAs/InAsSb superlattice. A lateral survey acquired at the beginning of the epitaxial growth clearly indicates the transition from the GaSb buffer to the superlattice structure; the subsequent transverse survey allows us to check for any cleavage–related steps across the growth sequence; and finally a lateral survey acquired close to the conclusion[4] of the structure permits comparative analysis of the composition and uniformity of the growth from initiation to completion.

[4] As there was no capping layer, we avoided the last few periods of the growth to remove the risk of imaging the edge and possibly losing the tip.

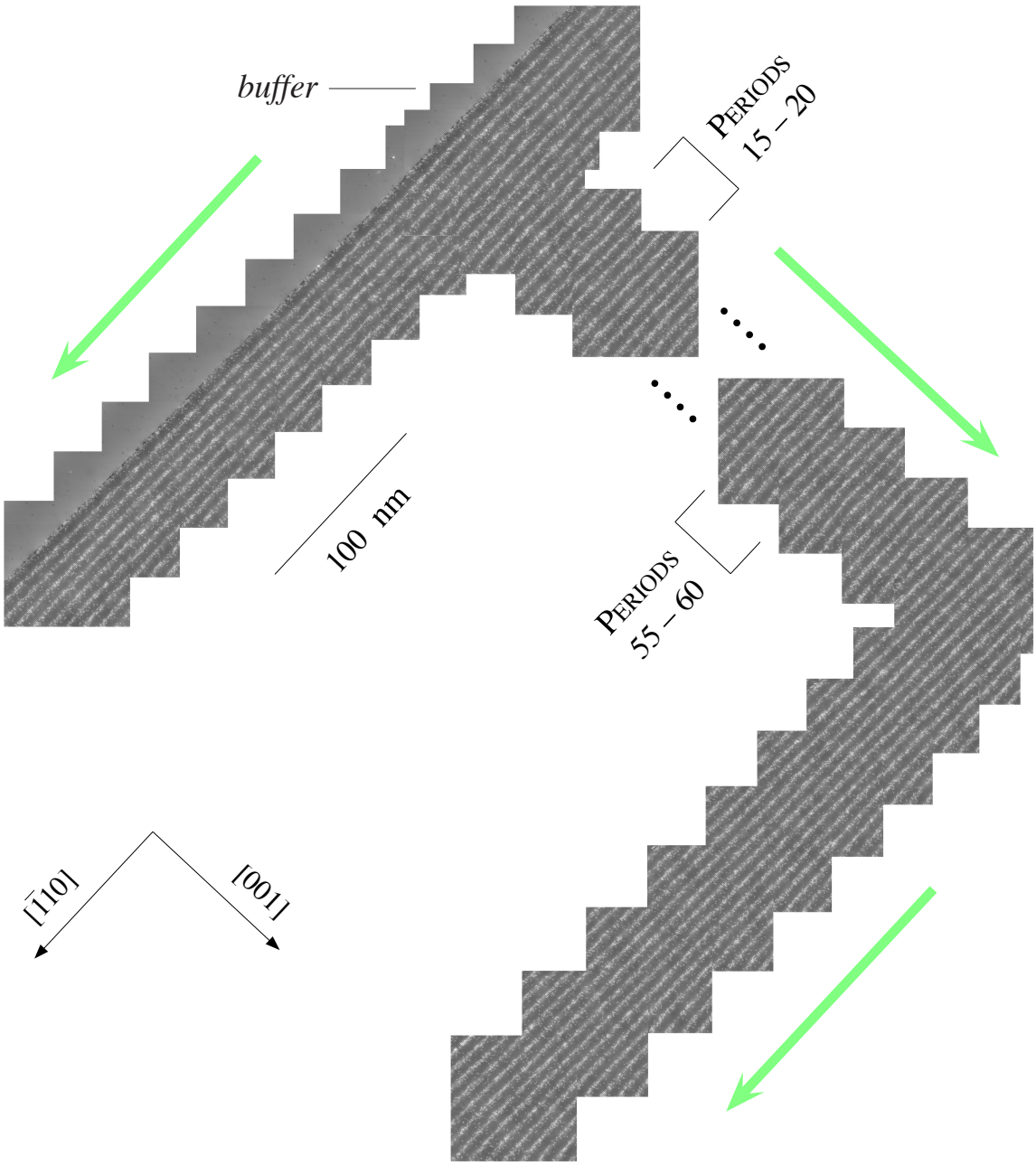

FIGURE 2.20. Device–scale, atomic–resolution surveys of an InAs / InAsSb superlattice. The lateral survey on the left was acquired at the start of the growth as indicated by the GaSb buffer layer, while the lateral survey on the right was acquired towards the conclusion of the growth. The two lateral surveys are joined by a transverse survey obtained across eighty–five repeats. Green arrows indicate the direction each survey was acquired. Growth direction is from top–left to bottom–right.

CHAPTER III

COMPOSITIONAL ANALYSIS*

Introduction

In this chapter, we present an analysis of the distribution of antimony in an MBE–grown gallium–free type–II superlattice with cross–sectional scanning tunneling microscopy. The composition of such a quantum–confined structure largely dictates the layer–by–layer strain, as well as layer–by–layer electronic properties. Deviations from the intended composition will modulate the local strain, affect the band–edge confinement potentials, and likewise influence transport effective masses. The nearly universal disconnect between intended and *as–grown* structures thus underscores the centrality of precision characterization for realistic device modeling.

We begin with a brief description of the device structure used for our study and quickly proceed to a discussion of the layer–by–layer mapping of the antimony distribution in this structure. We then review the general principles that govern the strobing of bulk planes by an STM tip positioned over the cleavage surfaces of zincblende structures. Finally, we present the case for well–motivated approximations to the bulk period in order to reconstruct a representative bulk composition profile from these STM data, and evaluate their credibility by way of dynamical x–ray simulations.

---

* Part of the data in this chapter is reprinted from M.R. Wood, K. Kanedy, F. Lopez, M. Weimer, J.F. Klem, S.D. Hawkins, E.A. Shaner, J.K. Kim, Journal of Crystal Growth, 425 (2015) 110-114.

Sample Structure

In this study we focus on an InAs/InAsSb superlattice fabricated by solid–source molecular beam epitaxy at Sandia National Laboratories. The nominal superlattice structure, outlined schematically in Fig 3.1 (left), consisted of 15.4 monolayers of InAs alternating with 5.4 monolayers of $InAs_{0.67}Sb_{0.33}$ for 100 periods atop an un–doped GaSb buffer; the intended bulk band alignments [41, 42] are shown in Fig. 3.1 (right). These layers were deposited on an (001)-oriented *n*–type GaSb substrate under an anion overpressure[5] of ~1.5:1 and growth rate of 0.9 monolayers / sec (ML/s). The substrate was held at approximately 420º C and rotated continuously throughout deposition. A high–resolution x–ray diffraction (HRXRD) examination of the (004) reflections in a triple–axis configuration was performed at Sandia, and subsequently analyzed by the STM Lab at TAMU. The x–ray spectrum revealed a period of 20.62 ML[6], and a mismatch of –0.05%, following analysis of nine superlattice satellite orders using Bragg's law [43], as shown in Fig 3.2.

Design Discrepancies with HRXRD

The HRXRD spectrum illustrates the quality of the crystalline structure for this growth, as well as the excellent match to the substrate. We used a dynamical x–ray simulation program [44] to generate a simulated spectrum for the intended structure (Fig. 3.1 left), assuming abrupt interfaces and compositional uniformity throughout the

[5] The quoted anion overpressure represents a sum of As:In of ~1.2 and Sb:In of ~0.3.

[6] This corresponds to 6.28 nm.

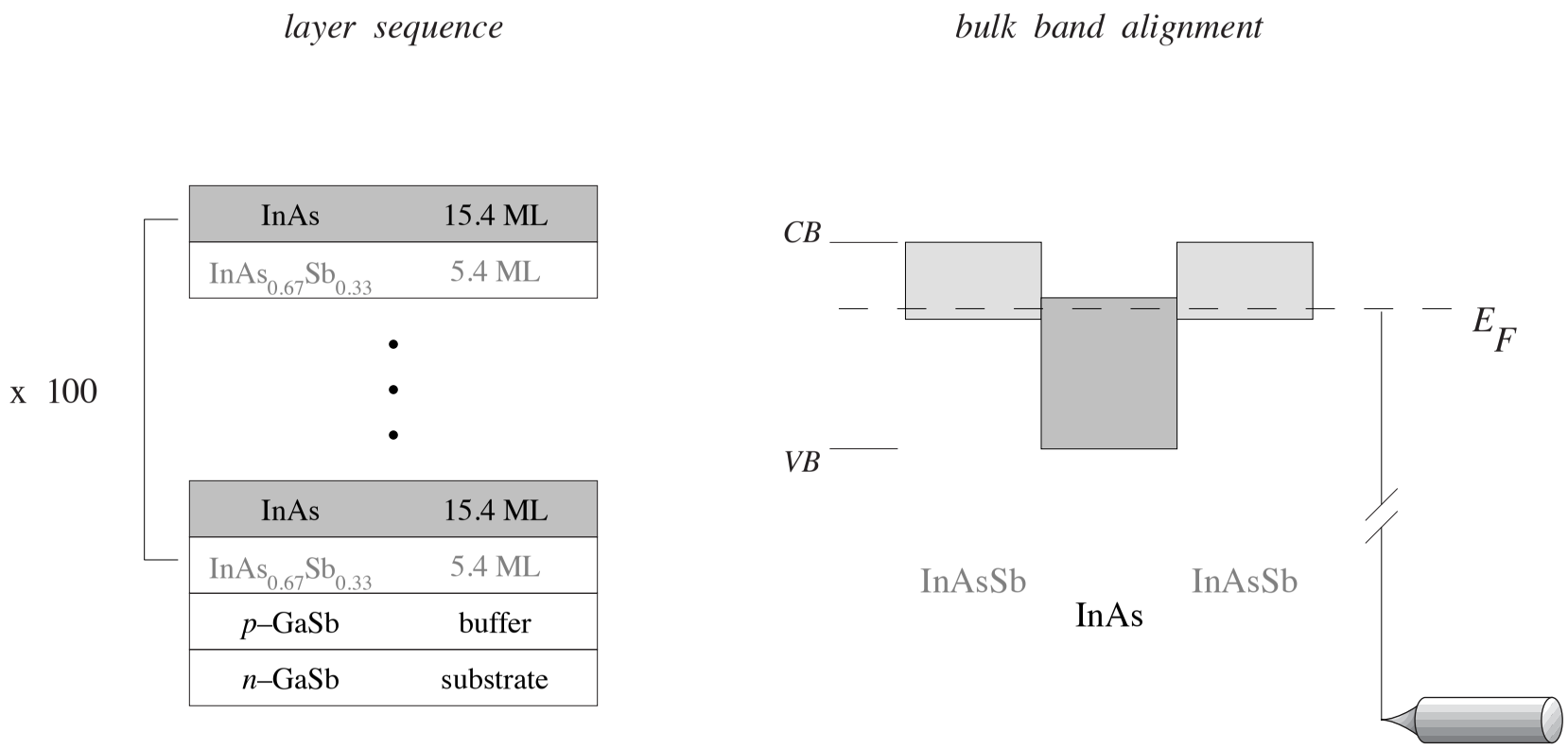

FIGURE 3.1 Intended layer sequence for the InAs/InAsSb superlattice (left); growth direction is bottom to top. The corresponding bulk band alignments are shown to the right.

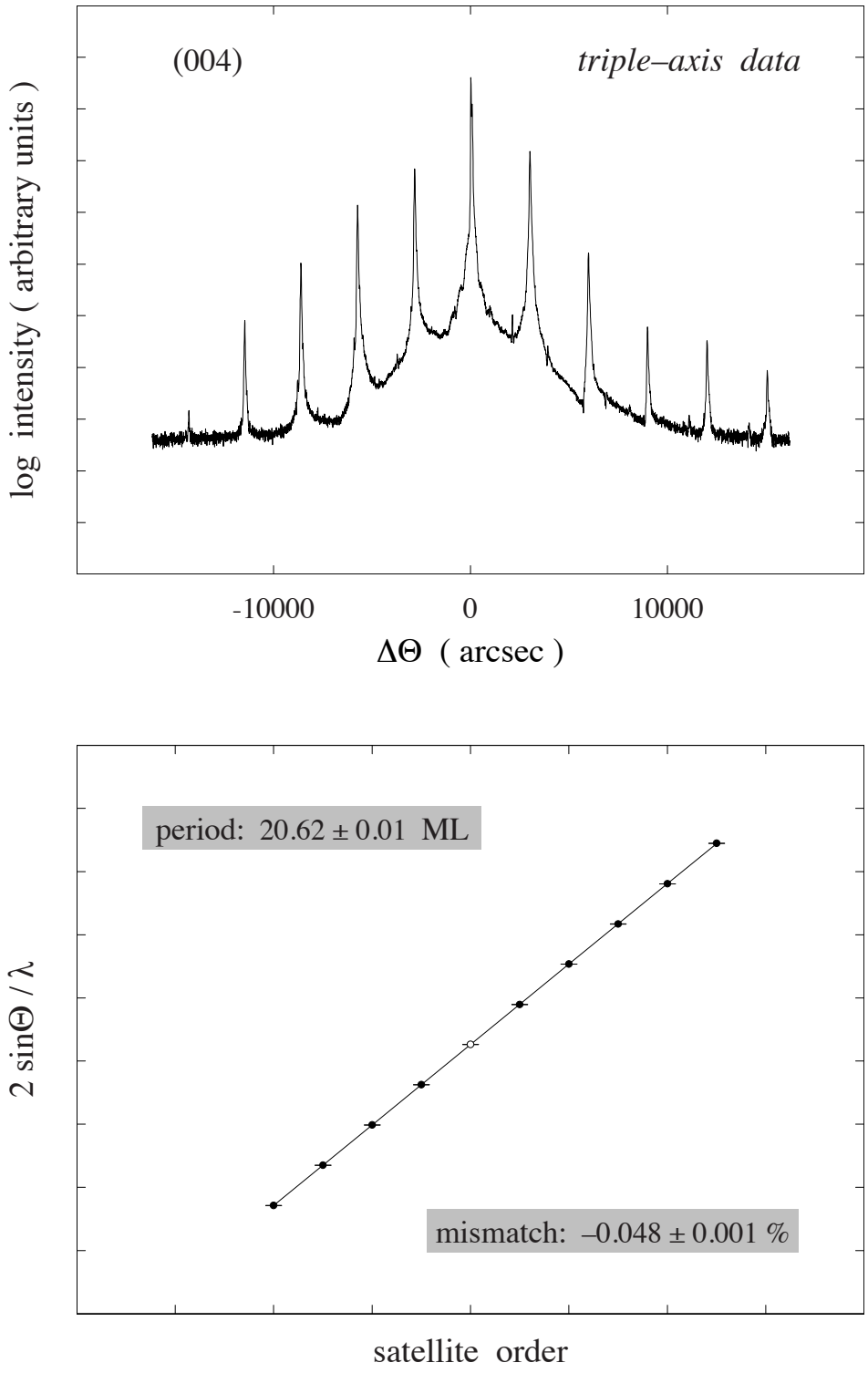

FIGURE 3.2 Conventional (004) triple–axis HRXRD measurement (top) and corresponding determination of superlattice periodicity from Bragg's law (bottom). The 100–period average measured by x–ray diffraction is 20.62 ± 0.01 ML.

structure. We then compared this simulation with the experimental HRXRD, as illustrated in Fig 3.3. Predicted and observed satellite peak locations agree, demonstrating the *as–grown* period and mismatch are close to their intended values, but predicted and observed peak intensities differ by up to two orders of magnitude bringing the assumed compositional uniformity into question. In addition to this conspicuous quantitative discrepancy, the assumed structure likewise fails to capture the visible broadening at the base of each satellite peak.

To determine the underlying cause(s) for these discrepancies, we used cross–sectional scanning tunneling microscopy (STM) to perform a real–space, monolayer–by–monolayer mapping of the superlattice composition. As mentioned earlier, the gross amount and detailed spatial distribution of antimony per superlattice period determines the energy band profiles for gallium–free, type–II superlattice structures.

STM Identification and Counting Method

Several lateral surveys, such as those shown in Fig 3.4, were acquired at select locations along the growth sequence for three separate sample dies; two were scored to expose a (110) cleavage plane, and the other a (1–10) cleavage plane, to specifically check for any growth anisotropies. A representative, atomic–resolution STM image of the anion sublattice is presented in Fig 3.5 with growth direction from upper left to lower right. Bright sites indicate isovalent replacement of antimony for arsenic, with individual instances labeled Sb_{As} (1) and Sb_{As} (3) corresponding to antimony substitutions that occur within the cleavage–exposed and second subsurface planes, respectively. These

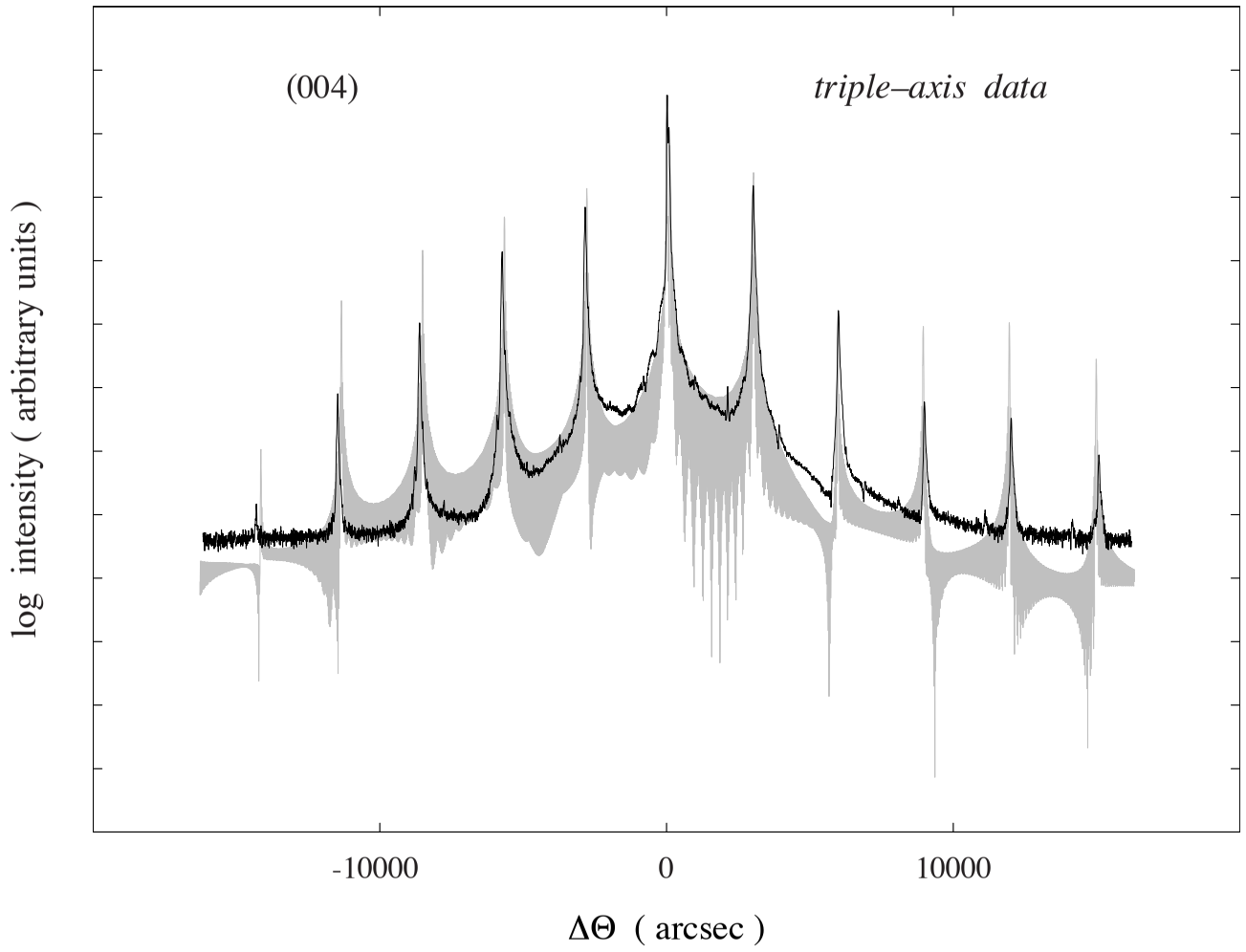

FIGURE 3.3 Dynamical x–ray simulation (normalized to the observed substrate peak intensity) assuming the intended composition shown in Figure 3.1, with compositional uniformity throughout the superlattice (grey). Comparison with the experimental HRXRD spectrum (black) reveals the assumed structure provides a comparatively poor global description of the x–ray data.

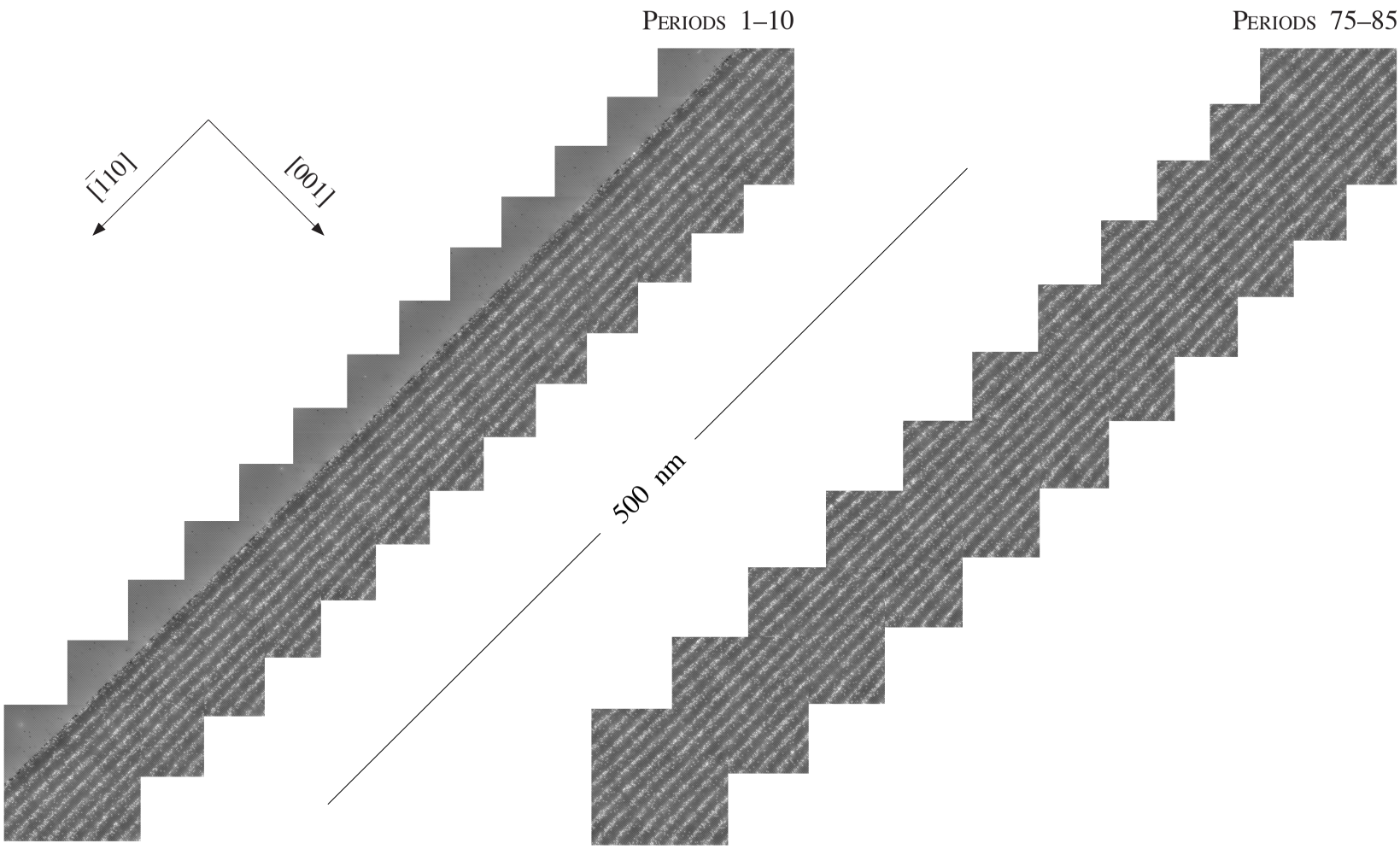

FIGURE 3.4. Device–scale, atomic–resolution surveys acquired along periods near the initiation and completion of the InAs / InAsSb superlattice from a (110) cross–section.

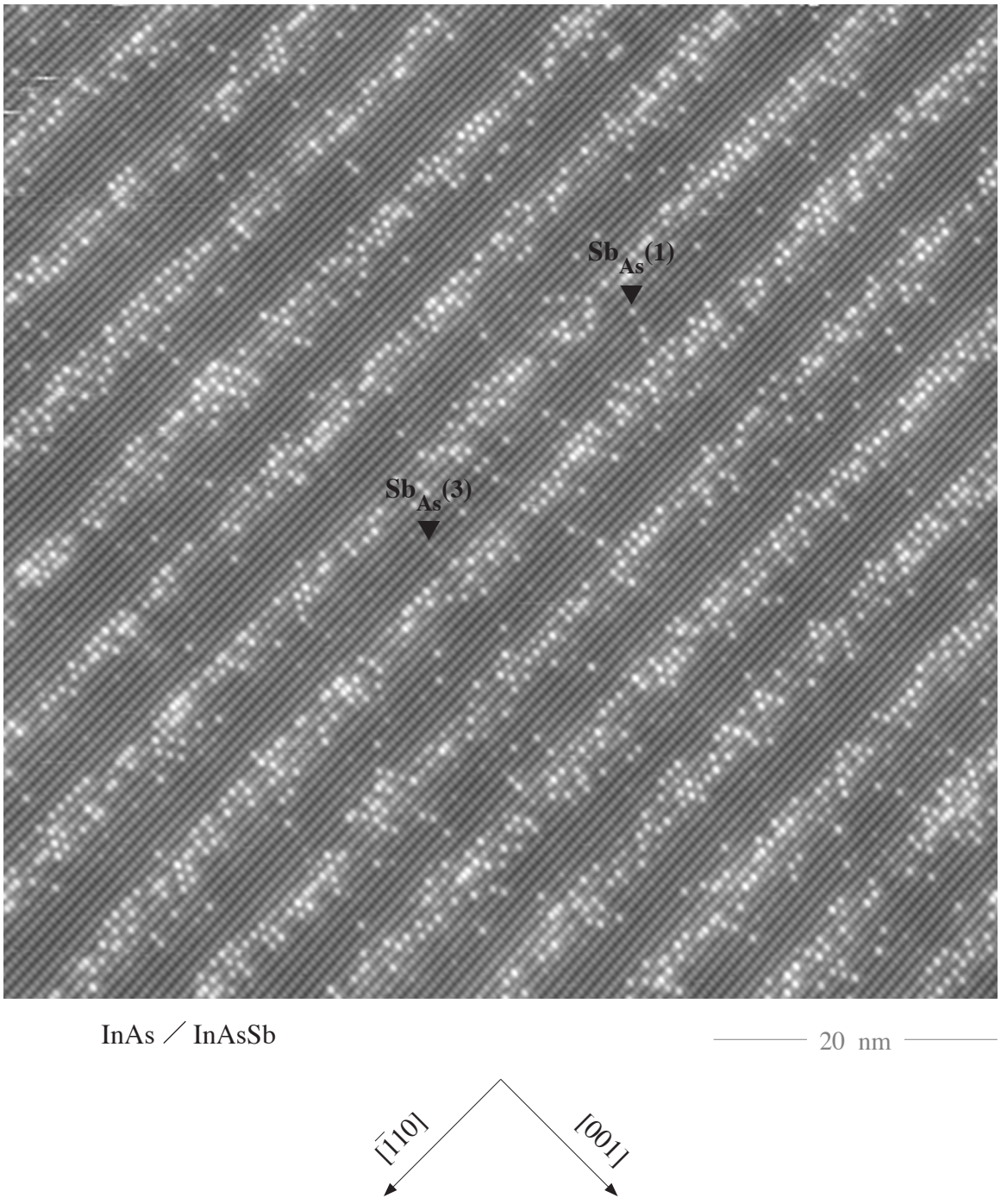

FIGURE 3.5 Atomic–resolution STM image of the anion (Sb, As) sublattice from a type–II InAs / InAsSb superlattice. Antimony–for–arsenic replacement within the top–layer, cleavage–exposed plane and second subsurface plane are identified by carets. Growth direction is from top–left to bottom–right.

sites appear bright due to two re-enforcing effects – the larger back–bond length attending non-native, InSb–like pairings in InAs, and the higher filled–state dangling–bond orbital energy for antimony versus arsenic. The distribution of these antimony sites is non–uniform and there is significant intermixing at the two interfaces.

To facilitate analysis of the antimony distribution within this structure, a counting window is overlaid on each STM image (Fig 3.6) to demarcate the same atomic rows across an entire survey. The STM images necessarily have some overlap with preceding and succeeding ones, so the width of the counting window along the in–plane <110> direction must be selected to maximize counting statistics while avoiding duplicate counts in neighboring images. The length of the window in the [001] growth direction, 62 surface monolayers, is chosen to sample the maximum number of bulk superlattice repeats consistent with the standard image size and previously determined window width (Fig. 3.6). It is then a straightforward, but time–consuming, task to carefully count by hand the individual Sb_{As} (1) sites. These top–layer antimony–for–arsenic sites are especially prominent due to their long back–bond and high dangling–bond orbital energy; subsurface Sb_{As} (3) sites, on the other hand, can be occluded by top–layer (Sb_{As} (1)) substitutions making their count less certain. An identical counting protocol was implemented for all lateral surveys.

The surveyed antimony counts in each atomic row are normalized to the total available sites within all windows to obtain the antimony fraction as a function of surface monolayer. Errors for each data point are then calculated by assuming the counts are random and using the standard deviation for a binomial distribution [45]

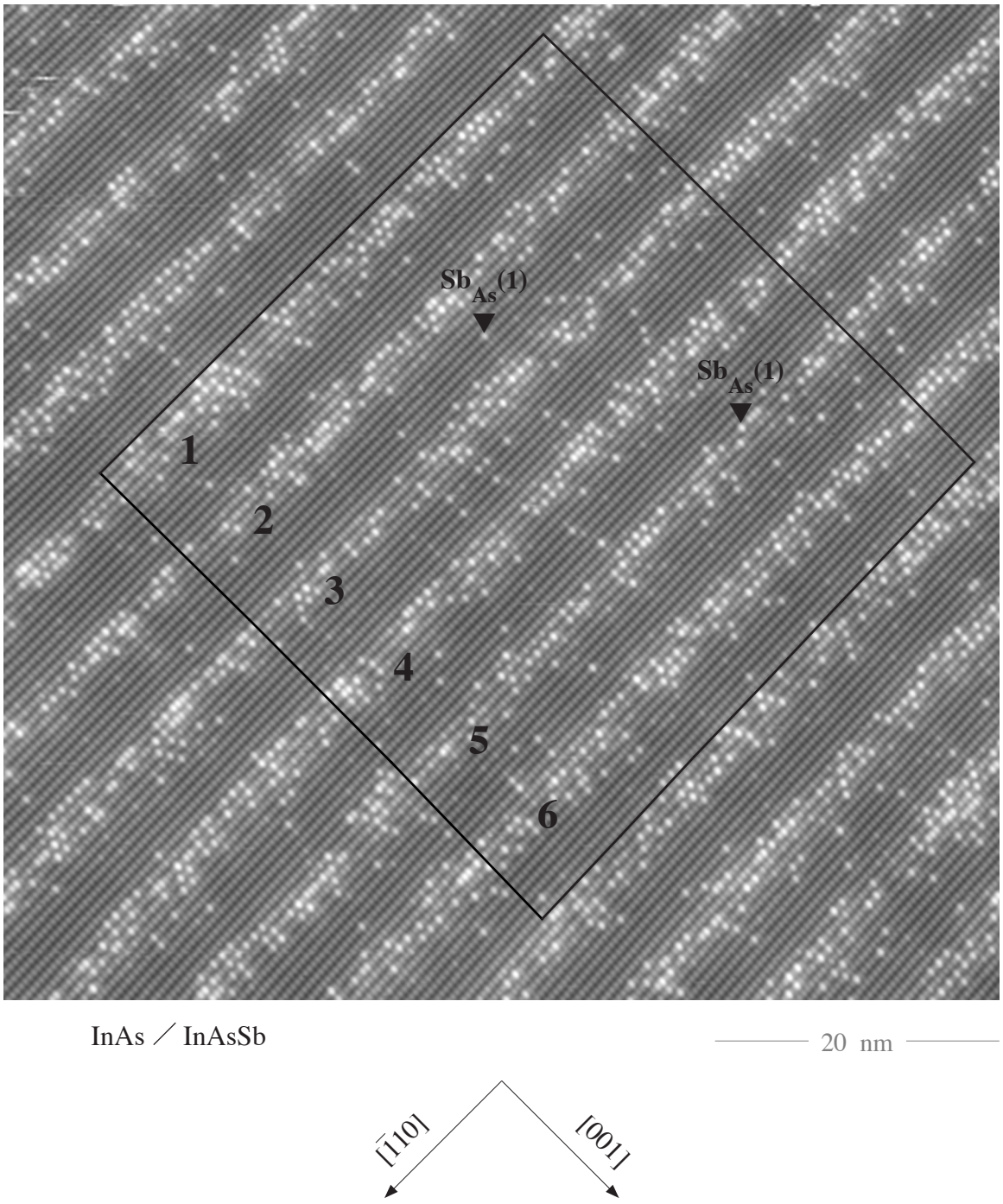

FIGURE 3.6. Representative counting window extending 62 surface monolayers in the growth direction, and encompassing 6 repeats of the superlattice period, was overlaid on each image of a survey. The width was selected to maximize total number of sites sampled in each window while avoiding double-counting in subsequent windows.

$$\sigma = \sqrt{np(1-p)} \tag{3.1}$$

where n is the number of available atomic sites, and p is the probability of a site being an antimony versus an arsenic atom. A representative surface antimony profile highlighting the modulation in the observed Sb_{As} (1) fraction across the entire counting region from one such survey is shown in Fig 3.7.

Surface and Bulk Distinction

In order to reconstruct a *bulk* monolayer–by–monolayer composition profile from the *surface* sampling obtained with STM, it is necessary to clearly understand the distinction between surface and bulk planes at {110} cleavage faces. For a zinceblende structure, only every other bulk (001) plane projects dangling bonds into the vacuum following {110} cleavage, hence the number of surface monolayers per period seen with STM is half that in the bulk. For a bulk period of even–integer value, each surface repeat[7] of the projected bulk planes represents the same alternating planes of the bulk layer sequence, so that the bulk is always under sampled. However, for a bulk period with an odd–integer value, two sequential surface repeats sample every bulk monolayer of the period once, revealing even– and odd–anion subsequences of the complete bulk profile in turn [46].

A simplified atomic diagram (Fig 3.8[8]) illustrates this strobing of the bulk by the

[7] A surface repeat is the surface sampling of the bulk anions. This term will be generalized in the succeeding text.

[8] In the diagram (and subsequent versions) we used InSb to represent InAsSb.

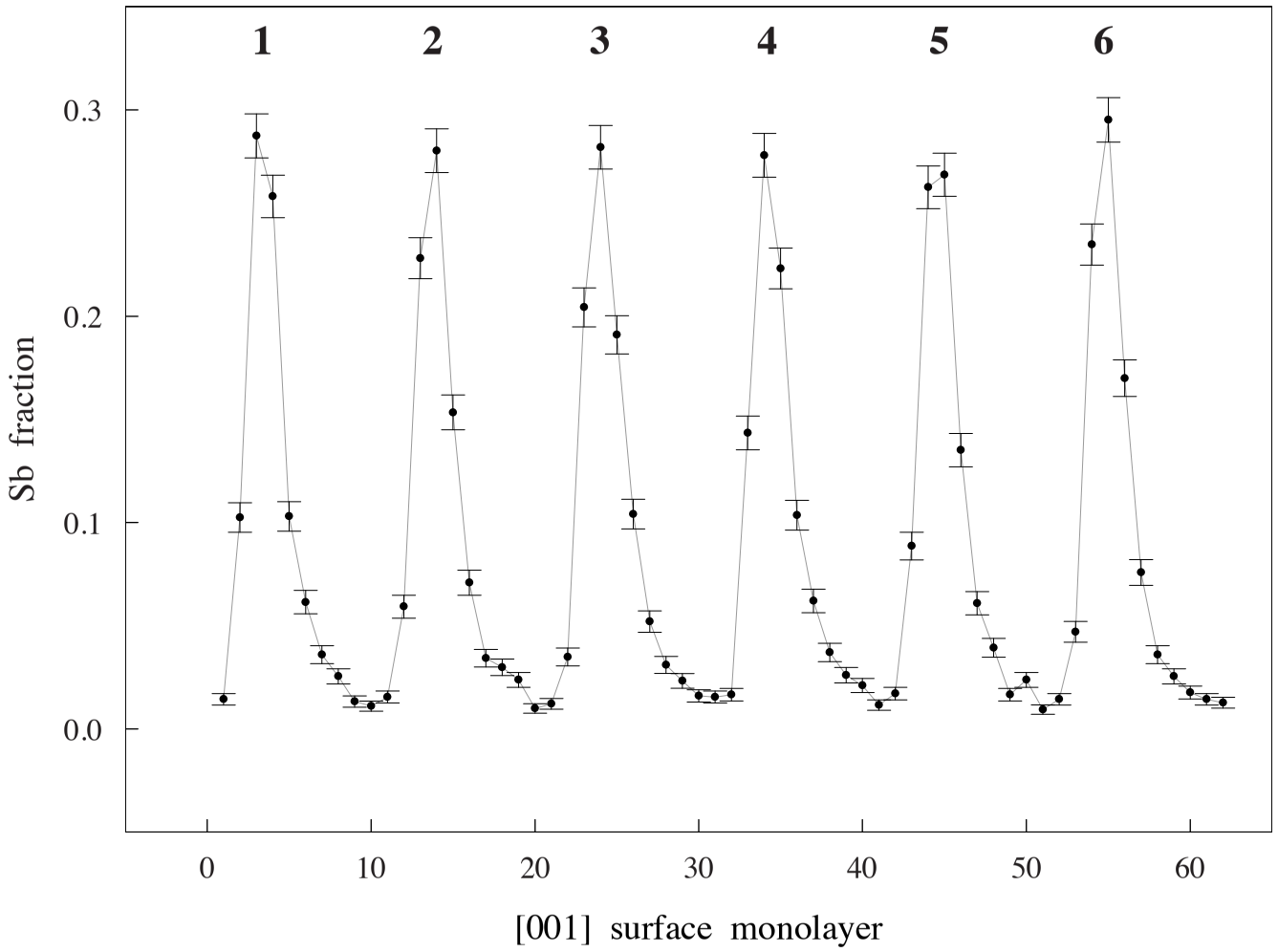

FIGURE 3.7. Observed antimony fraction as a function of surface monolayer (with corresponding binomial errors) calculated from a representative, micron–long <110> survey of six superlattice periods. Grey line is to guide the eye.

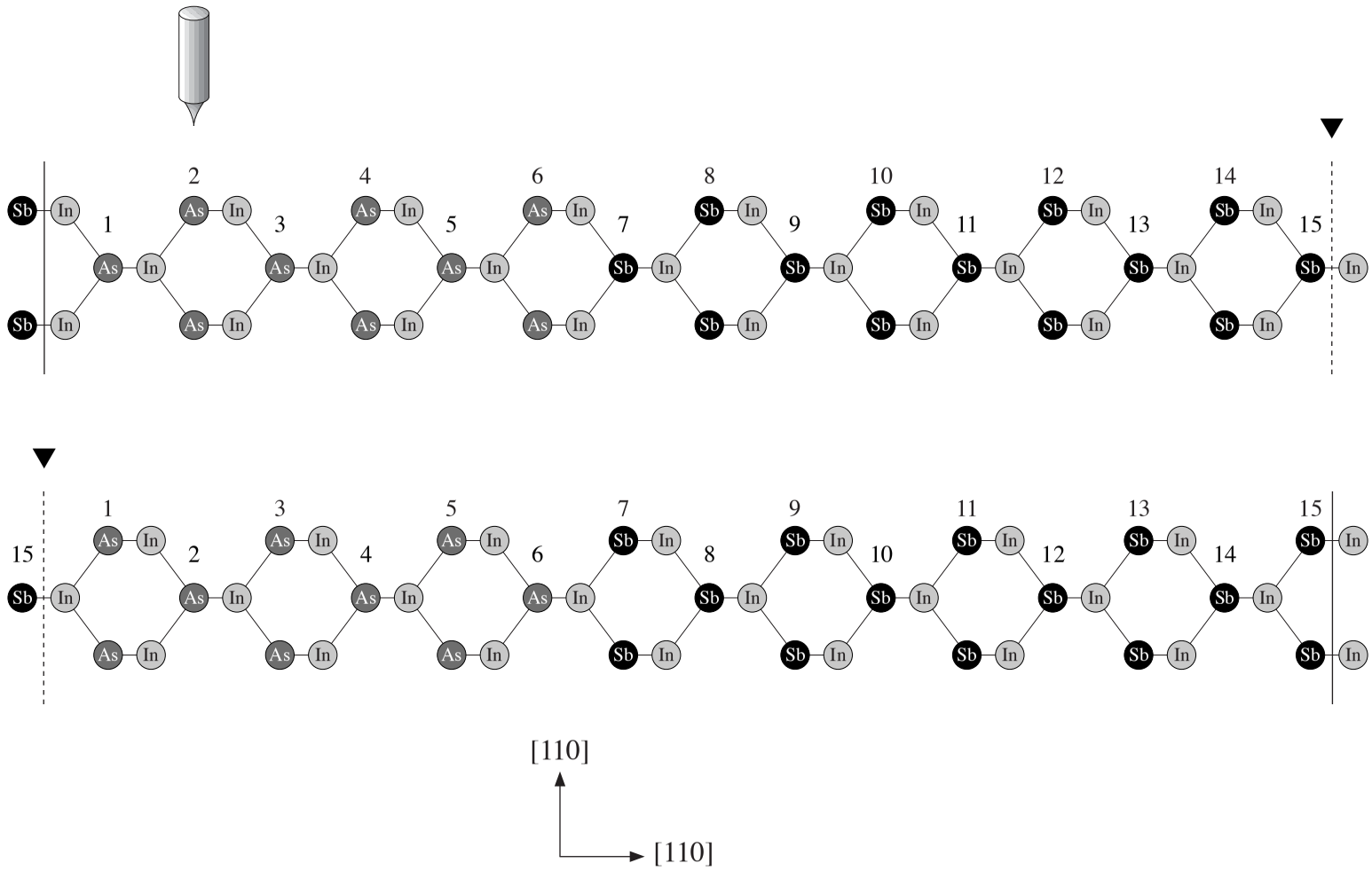

FIGURE 3.8. Simplified atomic diagram for an InAs/InSb superlattice with a bulk period of 15 ML. Schematic illustrates the strobing of bulk planes by an STM tip positioned over a (110) cross–section. The surface anions have dangling bonds, which are detected with STM, whereas the subsurface anions do not. The tip probes filled states; therefore, only anions are considered.

surface in (110) cross–section, where it is also clear the surface period is dictated by commensurability of the bulk period with an *integer* number of surface monolayers. In the diagram dashed lines indicate sequential surface repeats, carrots the continuation of the atomic structure from the first row to the second, and solid lines surface commensurability with the bulk. This relationship between bulk and surface periods can be written as

$$M \cdot B = 2 \cdot S \tag{3.2a}$$

where B is an integer bulk period, S the integer surface period, and M the integer commensurability number (i.e. the number of surface repeats to bring the surface and bulk back into coincidence with one another).

For bulk periods with a rational–fraction remainder, this bulk–surface relationship must be generalized via

$$M \cdot \Lambda = 2 \cdot S \tag{3.2b}$$

$$\Lambda = B + (p/q) \tag{3.2c}$$

where Λ consists of an integer (B) plus rational–fraction remainder (p/q), where p and q are integers. Commensurability is still guaranteed, but its rigorous fulfillment may be experimentally inaccessible due to the very large number of surface monolayers required. To determine the commensurability number (M) and surface period (S) we employ

$$M = \begin{cases} q & B \text{ even , } p \text{ even} \\ \\ 2 \cdot q & \text{all other cases} \end{cases} \tag{3.2d}$$

$$S = \begin{cases} \left(B \cdot q + p\right)/2 & B \text{ even , } p \text{ even} \\ \\ B \cdot q + p & \text{all other cases} \end{cases} \tag{3.2e}$$

For the special case of integer bulk periods (p=0), these formulas return the expected integer values with q=1.

With a bulk period of 20.6 ML, which is the case for the InAs/InAsSb superlattice studied here, 103 surface monolayers (S), or ten surface repeats (M), are required for strict commensurability. This is well outside our accessible counting window; therefore, to make use of the counting statistics from finite–size STM images, we need a reasonable approximation for the superlattice period that reduces this commensurability condition to a suitable number of surface layers.

Period Approximations

We explored two bulk–period approximations with small rational fraction remainders – 20.5 and 20.67 – that bracket the 20.6 value determined by HRXRD; these approximations translate into surface commensurabilities of 41 and 31 surface monolayers, respectively, each of which lies comfortably within our counting window. To establish the credibility of these two approximations, 31 ML and 41 ML sliding averages were calculated for each lateral survey; sliding averages for 40, 42, 30, and 32 surface monolayers were also calculated for comparison. Fig 3.9 illustrates one such 41 ML sliding window.

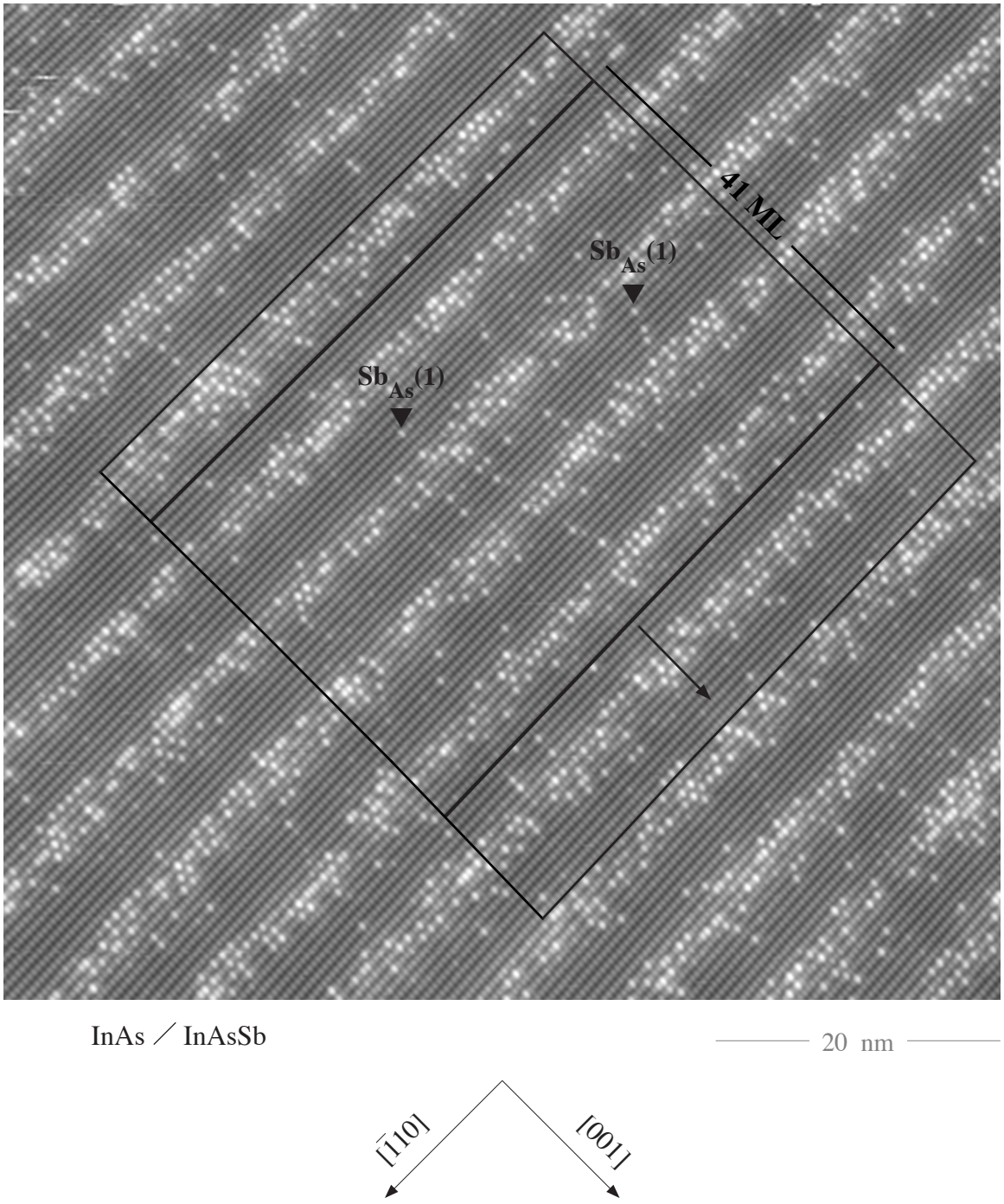

FIGURE 3.9. To determine the commensurability of the surface with the bulk for an approximate bulk period of 20.50 ML, a sliding average encompassing 40, 41, or 42 surface monolayers is performed and an average antimony fraction calculated with each step. The 41 ML subset is illustrated above.

As demonstrated in Fig 3.10 (left), the 41 ML sliding average is nearly translational invariant for early– and late–period lateral surveys, whereas other sliding averages include too few or too many monolayers to be commensurate with the bulk. As shown in Fig 3.10 (right), on the other hand, lateral surveys over the middle of the 100 period superlattice stack required a 31 ML window to achieve a similarly invariant result. The translational invariance manifestly demonstrated in Fig. 3.10 affirms that a bulk period approximation of 20.5 ML is reasonably accurate for superlattice periods near the beginning and completion of the growth sequence, whereas 20.67 ML is a better rational–fraction approximation for periods near the middle of the growth.

It is of interest to note that one may also use the respective, translationally–invariant sliding averages from each survey to look for any time dependence in the total antimony incorporated per superlattice period. Calculation of the survey–average surface antimony fraction per translation–invariant sliding average window points to a measureable increase in incorporated antimony from beginning to end of the multilayer stack. For two of the dies (Fig. 3.11 and 3.12) this increase lies between 12 and 13%; a third die (Fig. 3.13) displayed a somewhat smaller 7% increase. We return to this important observation later on, in Chapter IV.

Reconstruction of Bulk Antimony Profile

Having established either 20.50 or 20.67 ML approximations to the bulk superlattice period as valid over different subsets of the full superlattice layer sequence,

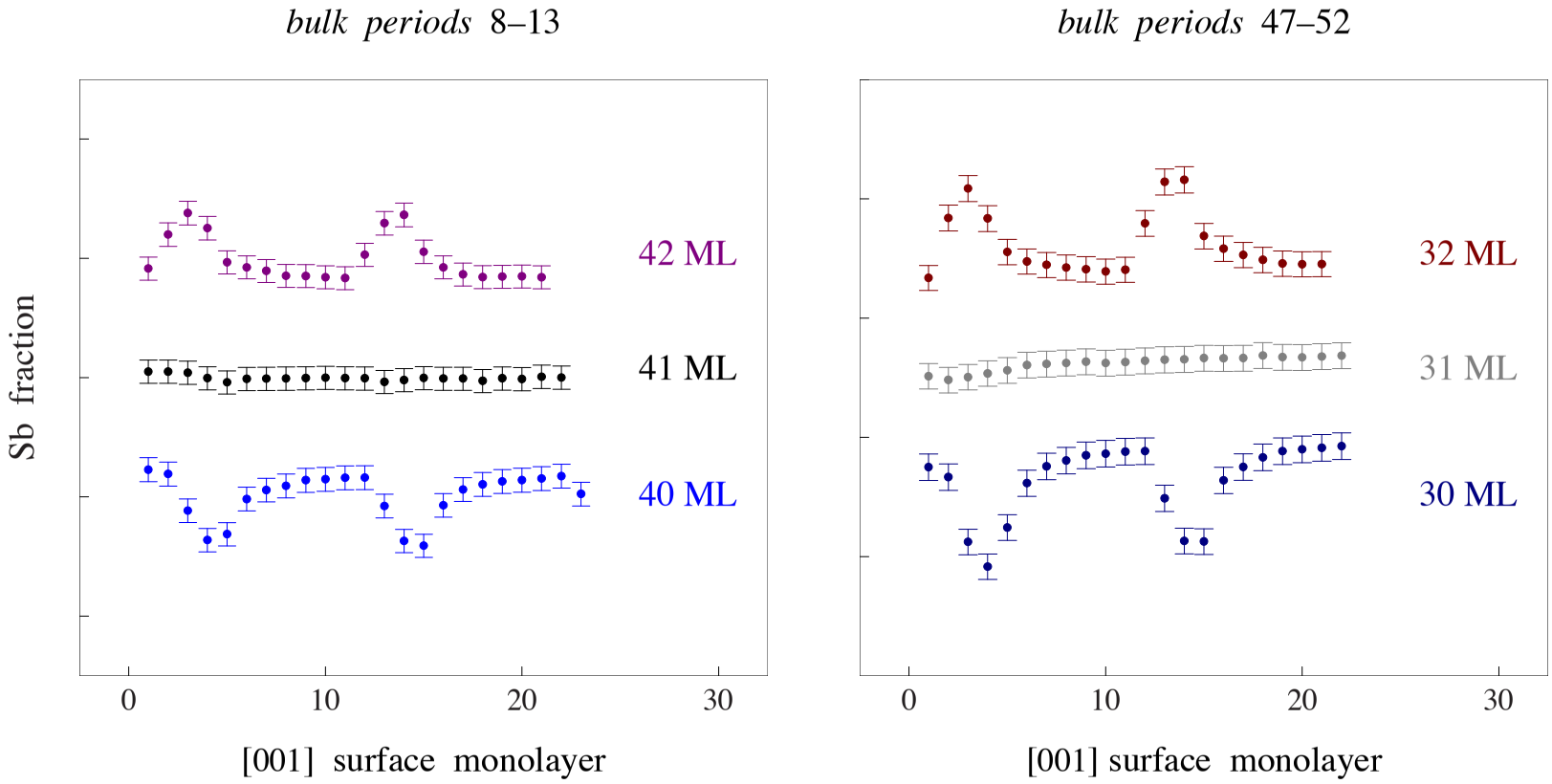

FIGURE 3.10. Sliding average plots for an early $(1\bar{1}0)$ survey, left, and middle $(1\bar{1}0)$ survey, right. The 41 ML window average is nearly translationally invariant for early–period and late–period (not shown) lateral surveys. The 31 ML subset provides a similarly translation–invariant result for surveys acquired from the middle of the growth.

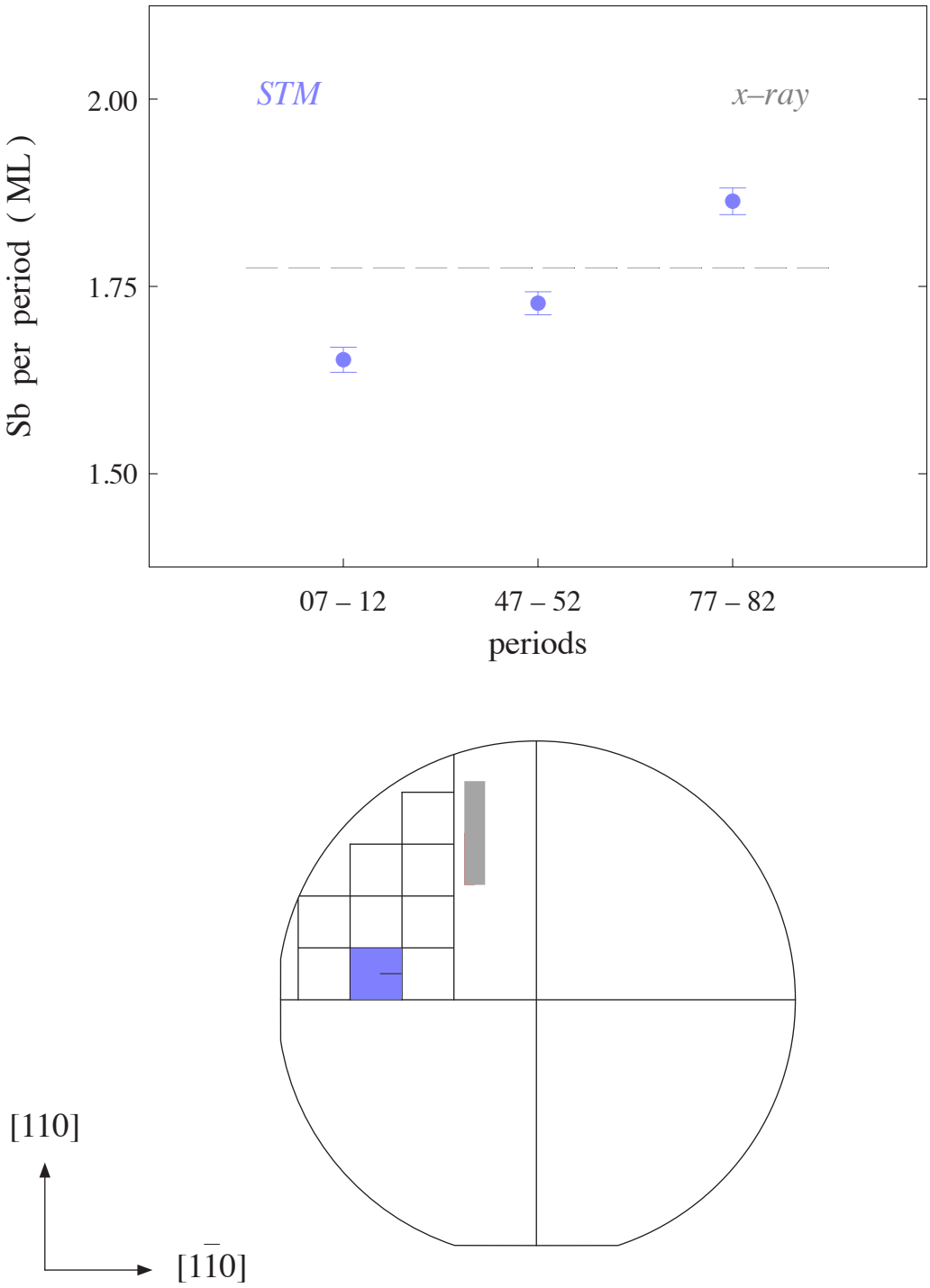

FIGURE 3.11. Total antimony per period calculations for (110) STM surveys acquired near the initiation, midpoint, and conclusion of the growth (blue points) reveal an increase of 13%. Wafer diagram illustrates the location of the sample die and x–ray measurement.

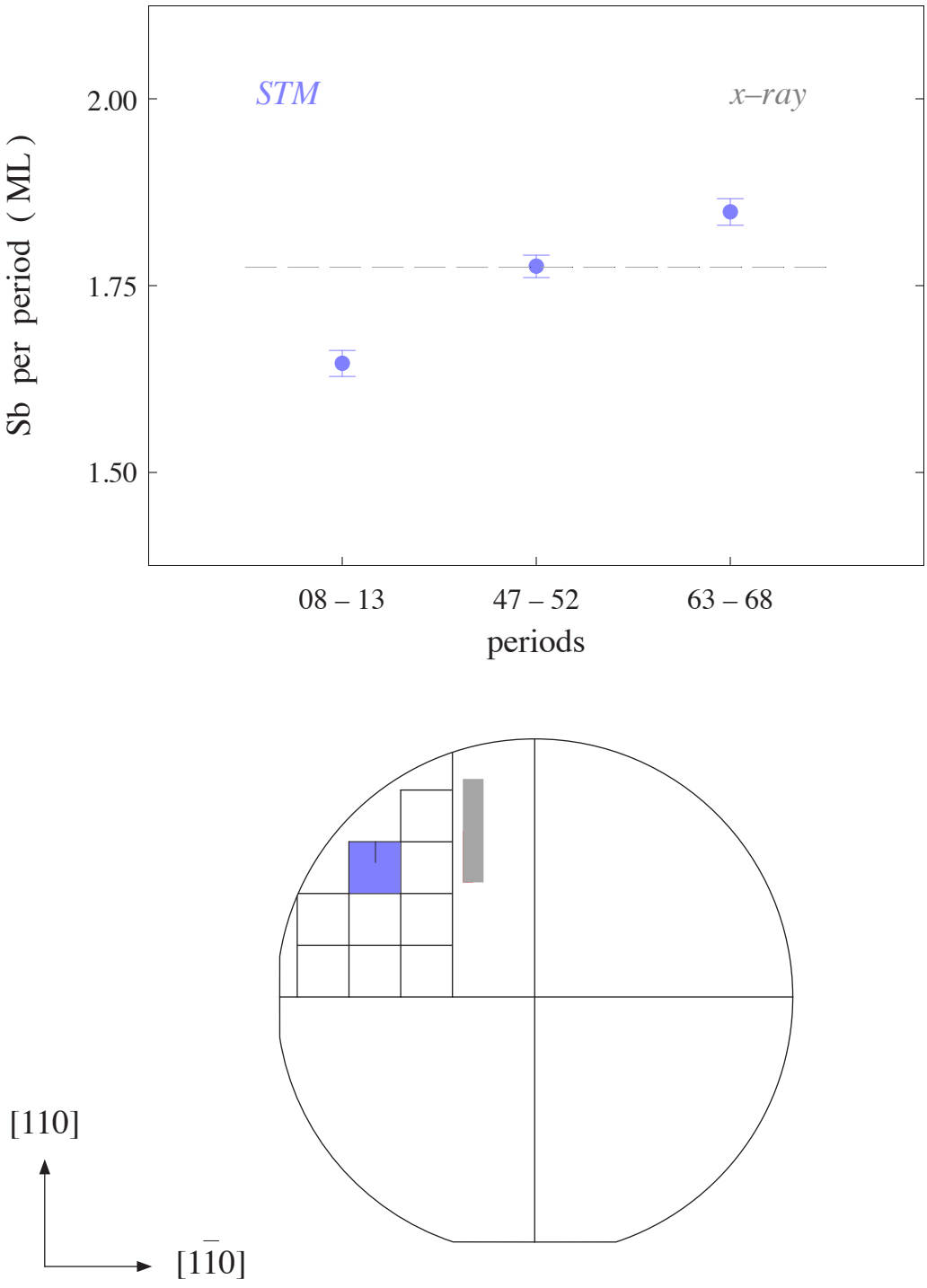

FIGURE 3.12. Total antimony per period calculations for (1$\bar{1}$0) STM surveys acquired near the initiation, midpoint, and conclusion of the growth (blue points) reveal an increase of 12%. Wafer diagram illustrates the location of the sample die and x–ray measurement.

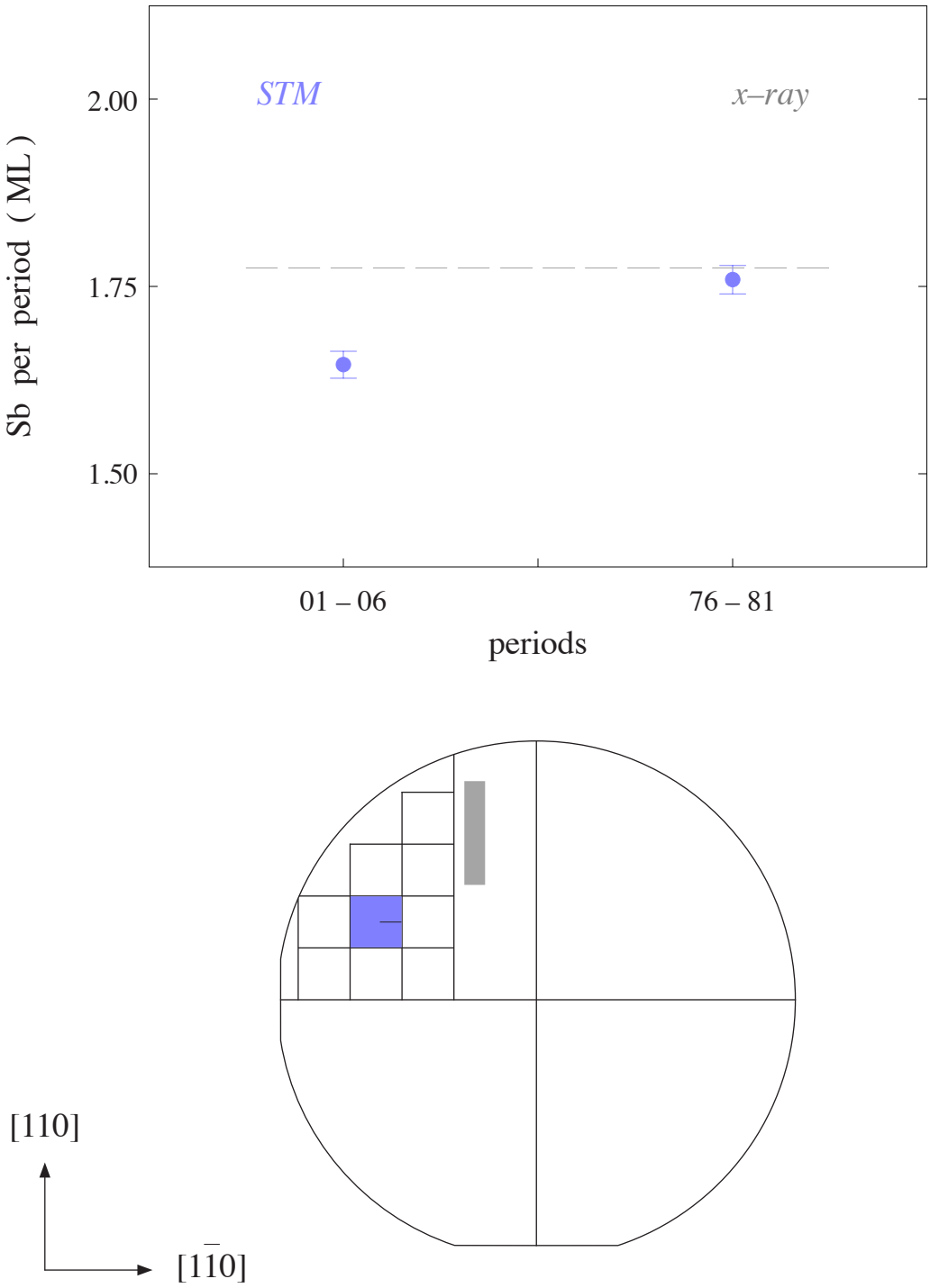

FIGURE 3.13. Total antimony per period calculations for (110) STM surveys acquired at the initiation and near conclusion of the growth (blue points) reveal an increase of 7%. Wafer diagram illustrates the location of the sample die and x–ray measurement.

we next reconstruct a representative layer–by–layer composition profile that summarizes the spatial distribution of antimony throughout a typical bulk period as follows.

The strobing previously illustrated in Fig. 3.8 is repeated in Fig. 3.14, where surface monolayer indices (*s*) and surface repeats (*m*) are now denoted in grey. As before, dashed lines indicate sequential surface repeats, carrots the continuation of the atomic structure from the first row to the second, and solid lines surface commensurability with the bulk. The same atomic diagram is shown again in Fig. 3.15 with the corresponding bulk monolayer indices (*b*) now denoted in black. The translation from surface monolayer index to bulk monolayer index follows the algorithm[9]

$$b = \left\{2 \cdot s\right\} \bmod \left\{(m-1) \cdot B\right\} \tag{3.3}$$

where *b* is an integer from 1 to *B*, *s* an integer from 1 to *S*, and *m* an integer from 1 to *M*. This algorithm is illustrated in Fig 3.16 for an odd integer bulk period (*B*) of 15 ML and surface period (*S*) of 15 ML. This re–identification is then used to interleave even and odd subsequences to reconstruct the full bulk profile.

The surface monolayers in each surface period are separated into *M* surface repeats following

$$S_m = \begin{cases} \left[S/M\right] & 1 \le m \le M - S \bmod M \\ \left[S/M\right]+1 & M - S \bmod M + 1 < m \le M \end{cases} \tag{3.4a}$$

$$\sum_{1}^{M} S_m = S \tag{3.4b}$$

[9] We define mod in the following manner: $a = b \left(\bmod\ d\right) \Rightarrow a = b + nd \Rightarrow a = b$, for mod 0 and integer *n*.

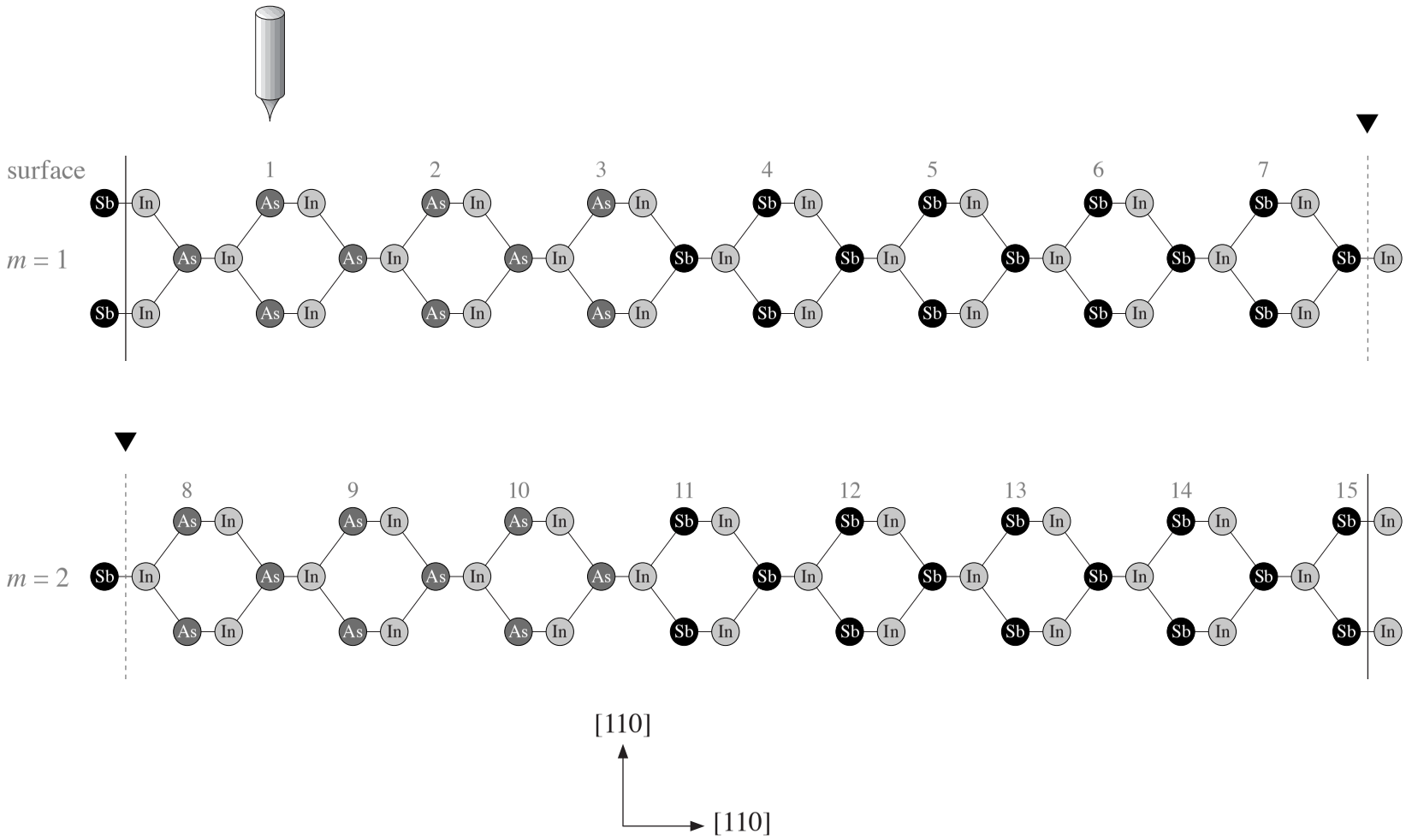

FIGURE 3.14. Simplified atomic diagram for an InAs/InSb superlattice with an integer bulk period of 15 ML, illustrating the surface monolayer index (s in Eq. (3.3)) of the surveyed anions over two surface repeats (m).

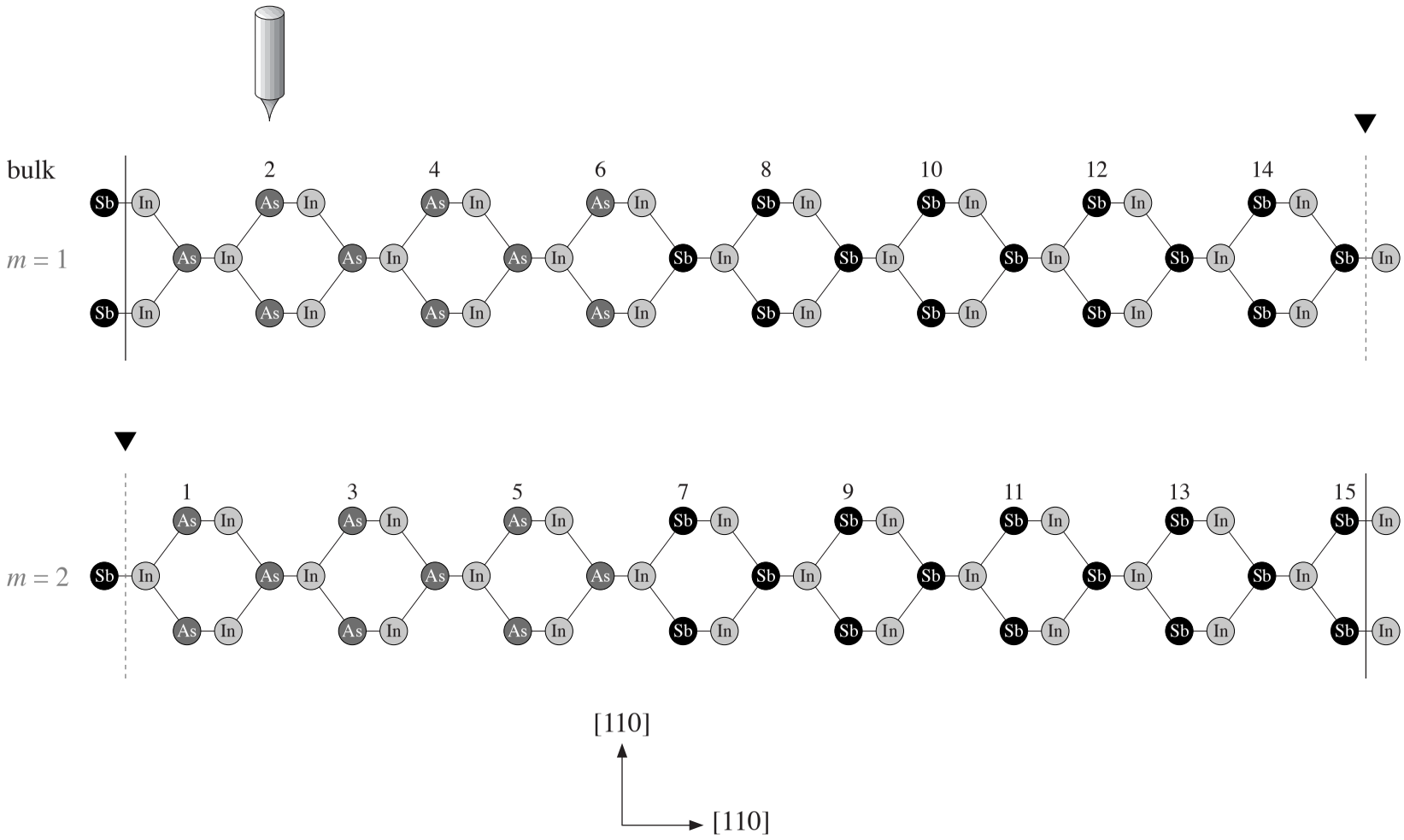

FIGURE 3.15. Simplified atomic diagram for an InAs/InSb superlattice with an integer bulk period of 15 ML, illustrating the bulk monolayer indices (b in Eq. (3.3)). These indices correspond to the surface monolayer indices (s in Eq. (3.3)) in Fig. 3.14 for surveyed anions across two surface repeats (m).

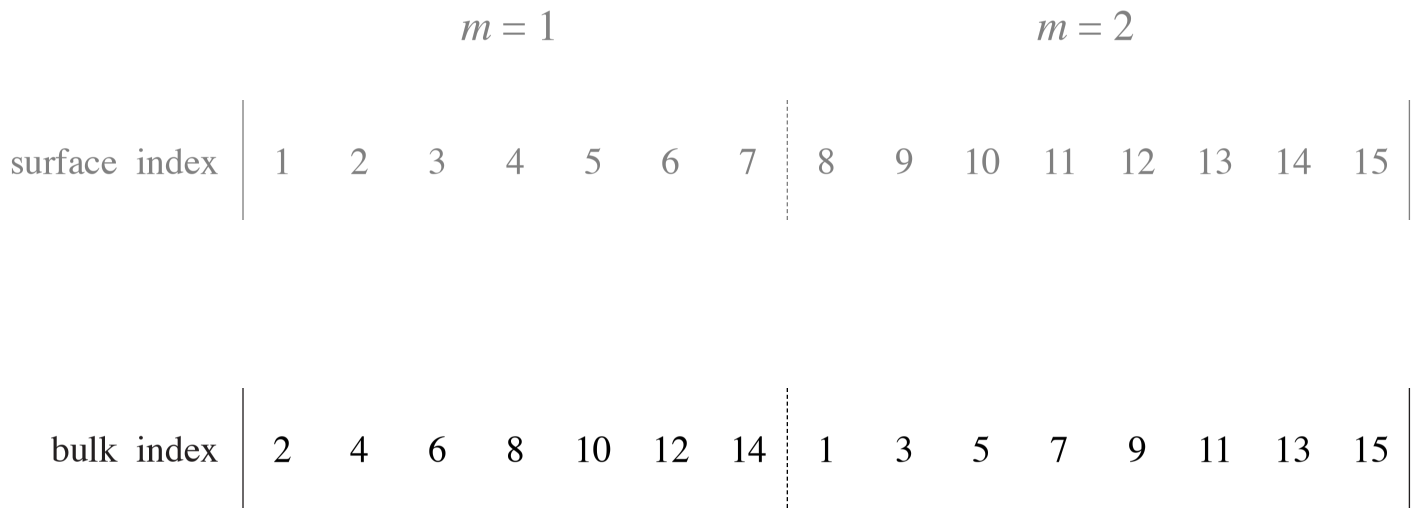

$$b = \{ 2 \bullet s \} \bmod \{ (m - 1) \bullet B \}$$

FIGURE 3.16. Illustration of the algorithm (Eq. (3.3)) used to convert integer surface monolayer index (s) to integer bulk monolayer index (b) for each surveyed anion in an observed surface repeat (m). The integer bulk period (B) here is 15 ML, and the surface and bulk indices correspond to Figs. 3.14 and 3.15, respectively.

where S_m is the number of surface monolayers assigned to a surface repeat, and [S/M] refers to the greatest integer function.

It is important to note that Eq. (3.3) assumes the number of surface monolayers per repeat (S_m) always follows Eq. (3.4a). For example, in Fig. 3.16 the grouping of surface monolayers according to Eq. (3.4a) (seven surface monolayers in the first repeat and eight in the second repeat) corresponds to the even– and odd–anion subsequences of the bulk period per Eq. (3.3)[10].

For bulk periods with a rational–fraction remainder, as is the case here, Eq. (3.3) can be written as

$$z = \{2 \cdot s\} \bmod \{(m-1) \cdot \Lambda\} \tag{3.5}$$

where z is now a rational bulk monolayer index. Fig. 3.17 illustrates the situation for a bulk period (Λ) of 7.5 ML and surface period (S) of 15 ML. Four sequential surface repeats (M) are needed to fully sample the bulk period, and the number of monolayers per repeat again follows Eq. (3.4). As with previous diagrams, dashed lines denote sequential surface repeats and solid lines indicate surface commensurability with the bulk. In this instance, odd repeats map onto *integer* bulk monolayer indices, whereas even repeats map onto *half–integer* values. As before, this mapping is used to appropriately interleave surface data to reconstruct a representative bulk antimony profile.

[10] It is important to add that our counting window, wherein this algorithm is applied, has an arbitrary offset associated with surface index, s; the bulk period (B or Λ) is the parameter governing the re–identification.

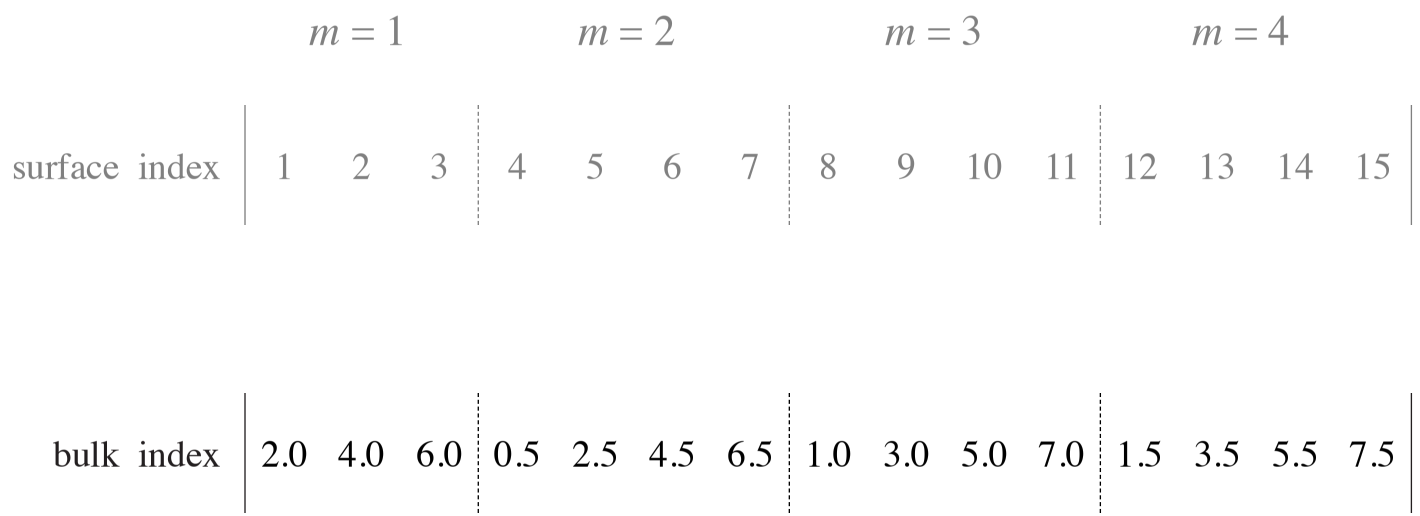

$$z = \{ 2 \bullet s \} \bmod \{ (m - 1) \bullet \Lambda \}$$

FIGURE 3.17. Illustration of the algorithm (Eq. (3.5)) used to convert integer surface monolayer index (s) to rational bulk monolayer index (z) for each surveyed anion in an observed surface repeat (m). The rational bulk period (Λ) here is 7.5 ML.

This discussion raises the question of proper interpretation of the fractional monolayers denoted by Eq. (3.5). For MBE, a fractional monolayer is well–defined since shutter times and elemental fluxes are both well–controlled and unrestricted to discrete "integer" values. A fractional monolayer is likewise well defined for x–ray diffraction, but not for an atomic lattice structure where atomic positions are by definition discrete. We interpret the fractional monolayers described here as lateral averages over domains. As an example, in Fig. 3.17 where the bulk period is 7.5 ML, a random sampling from a one micron long survey would produce a period of 7 ML with 50% probability and 8 ML with 50% probability.

Using the interleaving algorithm defined by Eq. (3.5), we can now "fold back" the six peak *surface* profile (Fig. 3.7) into a single *bulk* antimony profile (Fig. 3.18) for each lateral survey. Because this fold back is based on an approximation to the bulk period, albeit a good one, these reconstructed profiles yield a semi–quantitative picture of the antimony distribution rather than a precision measurement. As we will see later on in Chapter IV, however, they are actually quite close to the truth.

The profile shown in Fig 3.18 is typical of all our data and differs quite markedly from design intentions (grey). There is an exponential–like rise and subsequent exponential–like fall in the antimony fraction, reflecting compositionally–graded, rather than abrupt, heterojunctions. As we explicitly demonstrate in Chapter IV, this compositional grading is due to antimony segregation, but for now it is sufficient to point out the occurrence of this phenomenon at *both* interfaces is not readily apparent from Fig. 3.7.

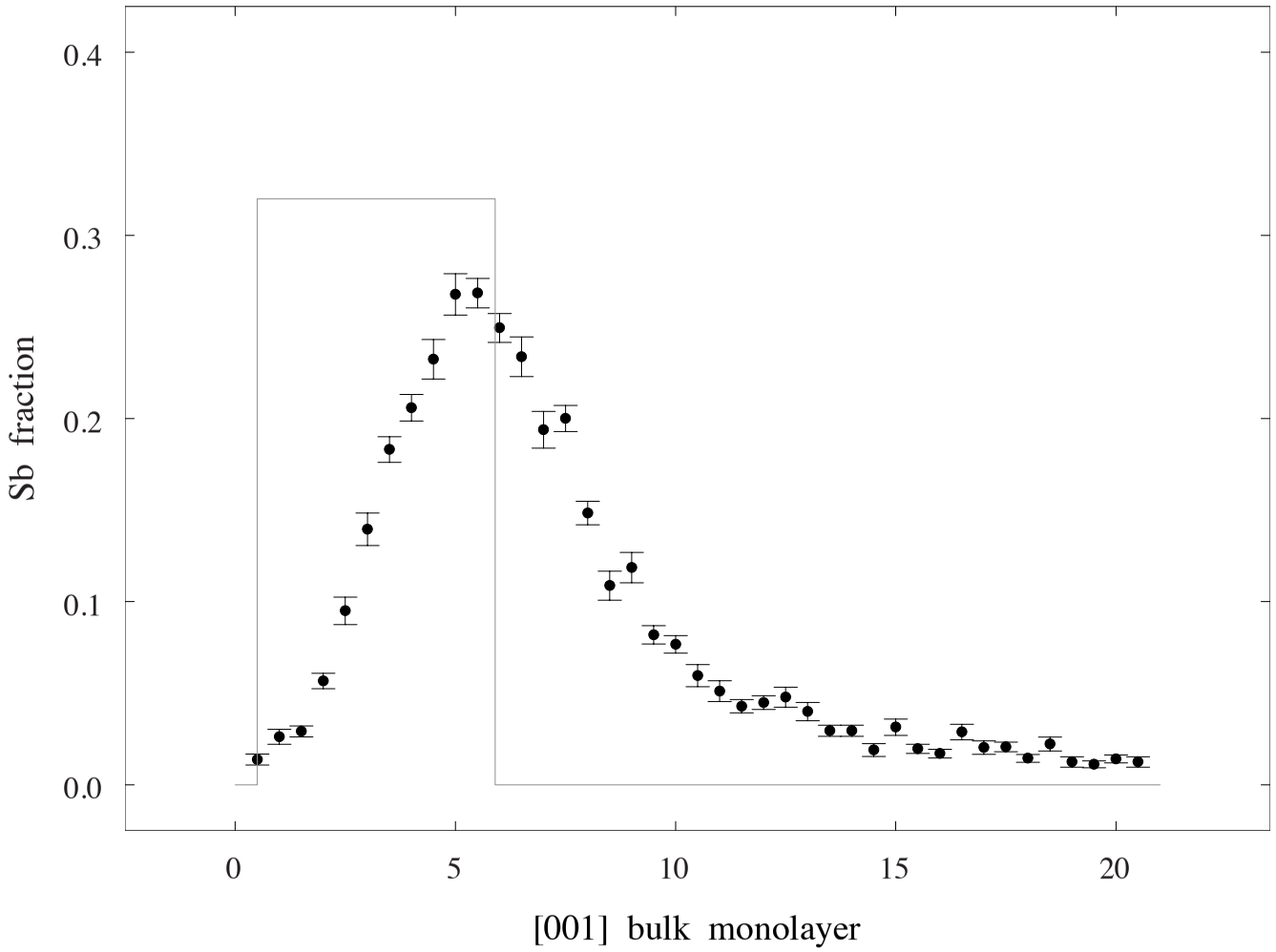

FIGURE 3.18. The compositionally–graded as–grown antimony profile reconstructed from STM. The data (assembled, here, from a late–period survey) exhibits an interfacial asymmetry characteristic of segregation. Intended profile is overlaid in grey.

It is likewise of interest to consider the monolayer–by–monolayer strain that follows from the compositional grading seen in the reconstructed bulk antimony profile. This strain serves as an important touch point for alternative characterization techniques, such as TEM [47], which measure strain in order to infer composition, and it likewise enters into many calculations of superlattice optical properties [48]. It turns out that, under conditions of coherent growth, the [001] lattice constant of InAsSb on GaSb is approximately linear in composition due to the near degeneracy of InAs and InSb Poisson ratios [49]. As a consequence, the predicted bulk strain profile for psuedomorpic InAsSb, plotted in Fig 3.19, directly mirrors the antimony fraction in the bulk profile of Fig 3.18.

To make the case that this STM–derived profile is representative of the superlattice structure as a whole, we again turn to dynamical x–ray simulations. Using the antimony fractions and resulting strain from each bulk profile as inputs to the simulation program, we generate an x–ray simulation for each survey. The experimental spectrum is compared against one of the (110) late period survey simulations in Fig. 3.20. The simulation provides a good description of the satellite peak intensities and background. This makes a convincing argument that our reconstructed antimony profile is characteristic of the superlattice as a whole, and points to compositional grading as the primary source of the difference between *as–grown* and intended x–ray spectra (Fig 3.2). To be sure, there are still small discrepancies between the STM–profile simulation and the experimental spectrum due to the period approximation employed as well as the

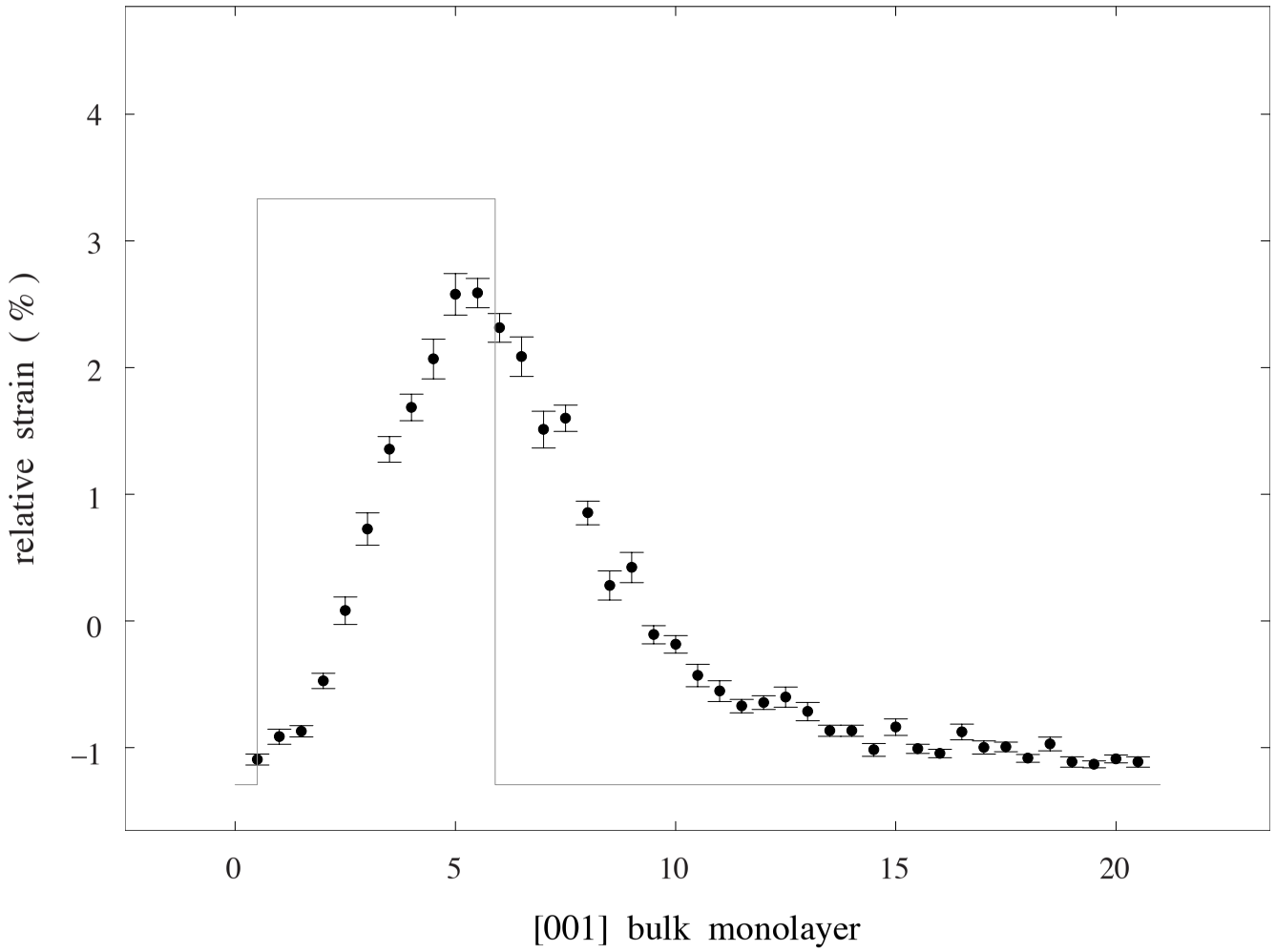

FIGURE 3.19. The corresponding strain, under coherent growth conditions, for the reconstructed profile in Fig 3.18. The inferred bulk strain directly mirrors the observed bulk composition. Intended strain is overlaid in grey.

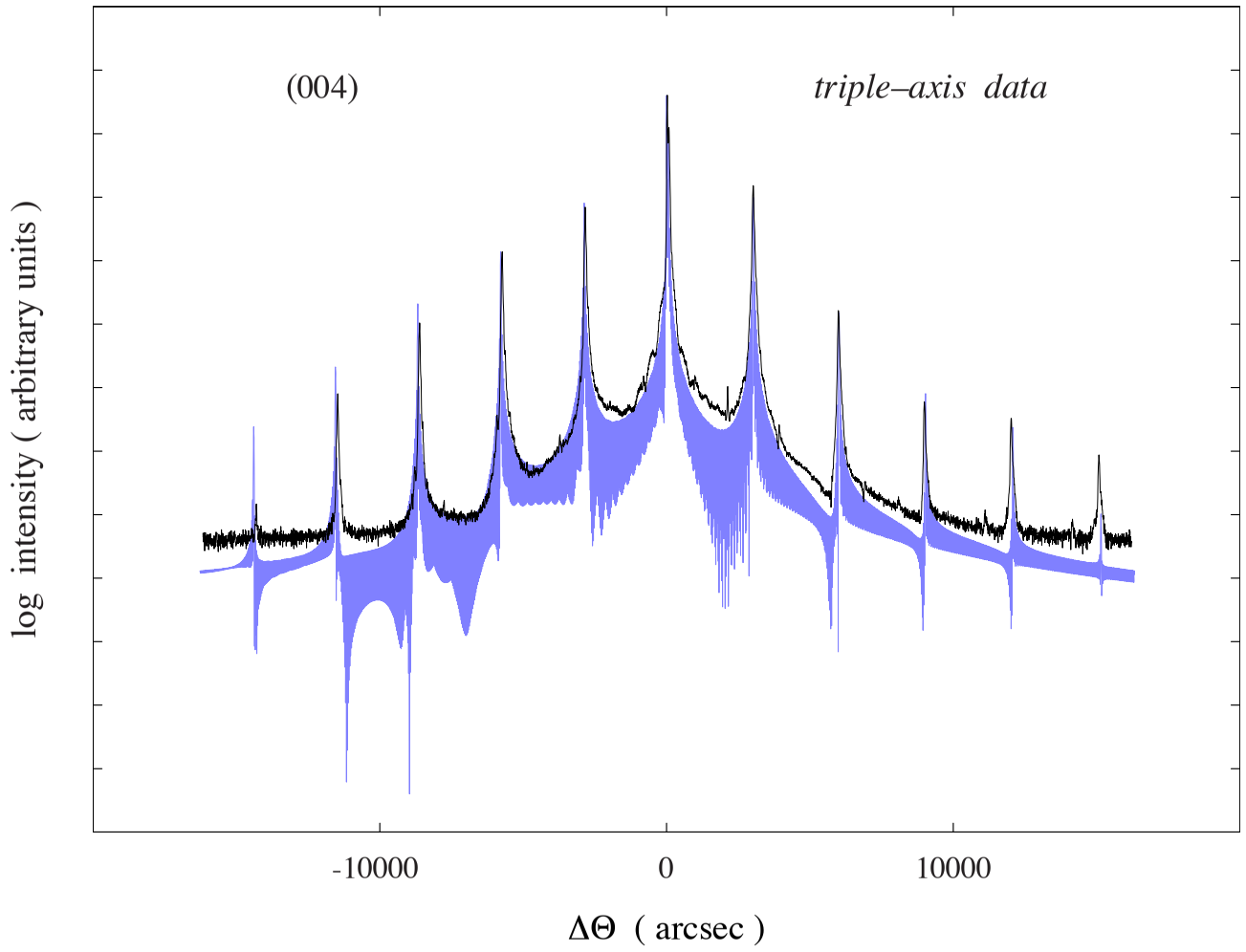

FIGURE 3.20. Dynamical x–ray simulation (normalized to the observed substrate peak intensity) assuming the as–grown profile in Fig. 3.18 deduced from STM (blue). Comparison with the experimental HRXRD spectrum (black) demonstrates this structure provides a good global description of the observed x–ray satellite peak intensities and overall background.

variation in incorporated antimony over the 100–period superlattice stack, but these discrepancies will be addressed in Chapter IV.

Synopsis

We have obtained monolayer–by–monolayer compositional analyses of a gallium–free type–II InAs/InAsSb superlattice with cross–sectional scanning tunneling microscopy through identification of isovalent replacement of antimony for arsenic on the atomic scale. Multiple lateral surveys were acquired at various points along the multilayer stack for three separate locations on the sample wafer, providing a large statistical pool of data for analysis. The antimony fraction as a function of surface monolayer revealed a modulation of the antimony distribution across the superlattice structure.

In the above discussion, we presented the case for approximations to the bulk period in order to reconstruct a representative bulk composition profile, with one approximation for the STM surveys near the beginning and end of the growth and a separate approximation for the middle–period surveys. The presence of more than one bulk period in the superlattice is further explored in Chapters IV and V.

The reconstructed composition profiles provide appropriate visualization of an exponential–like increase and decrease in incorporated antimony, qualitatively consistent with anion segregation. HRXRD simulations based on the STM profiles agree overall with experiment, pinpointing compositional grading as the major source of the

discrepancies between intended and observed x–ray spectra. Detailed analysis of the atomic processes that lead to the compositional grading is the subject of Chapter IV.

CHAPTER IV

ANTIMONY SEGREGATION ANALYSIS*

Introduction

We now go on to examine the source of the compositional grading observed in InAs/InAsSb superlattices via bulk composition profiles reconstructed in Chapter III. An earlier study using scanning tunneling microscopy [50] noted interface asymmetry in an InAs/InAsSb superlattice grown by modulated molecular beam epitaxy. This asymmetry was attributed to anion cross–incorporation and antimony "riding up" into subsequent InAs layers. In another study [8], interface asymmetry was examined for a related structure, InAs/GaInSb, and antimony segregation was determined to be the cause. Here, we build on the hypotheses and insights gleaned from these studies to definitively characterize the growth non–idealities present in gallium–free type–II superlattices.

We begin this chapter with a brief overview of our segregation model and its application to the (single–peak) reconstructed bulk composition profiles. We proceed next to discuss adaptation of the segregation model to fit the original (six–peak) surface antimony profiles, and critically evaluate the resulting parameters. Finally, we conclude with dynamical x–ray simulations, taking into account the compositional grading observed with STM, as well as the evolution in incorporated antimony per period discussed in Chapter III, to provide a convincing argument that our analysis with STM is characteristic of the superlattice as a whole.

---

* Part of the data in this chapter is reprinted from M.R. Wood, K. Kanedy, F. Lopez, M. Weimer, J.F. Klem, S.D. Hawkins, E.A. Shaner, J.K. Kim, Journal of Crystal Growth, 425 (2015) 110-114.

Segregation Model and Continuum Generalization

We previously noted that the bulk composition profiles reconstructed in Chapter III appear asymmetrical when compared against the intended profile (Fig. 4.1). Ideally, during deposition, antimony should be confined to the InAsSb layers forming rectangular barriers. However, the *as–grown* antimony fraction displays an exponential–like increase, followed by a corresponding exponential–like decay, suggesting anion segregation. There is also an offset to the baseline antimony fraction, most likely due to anion cross–incorporation.

When antimony is co–deposited with arsenic, some portion of the antimony flux is incorporated in the current monolayer, while the remaining fraction is ejected to a floating layer on the surface and made available (in addition to the incoming flux) for incorporation into the next monolayer. Once the antimony–source shutter is closed, this partitioning continues as additional arsenic layers are formed until the floating layer is exhausted or the shutter is opened again. This process is referred to as anion segregation, asymmetric compositional grading across the two interfaces of the superlattice is its tangible consequence.

Anion cross–incorporation refers to a spatially uniform, random distribution of foreign species incorporated into the growth via unintended substitution for another anion. The anion species produced by the effusion cells are typically molecular (e.g. Sb_2) while the cations are atomic (e.g. In). The sticking probability for anion molecules is also smaller than that for cation atoms, so an anion overpressure is (almost) universally required for stoichiometric growth [19, 20]. As the anion vapor in the effusion cell

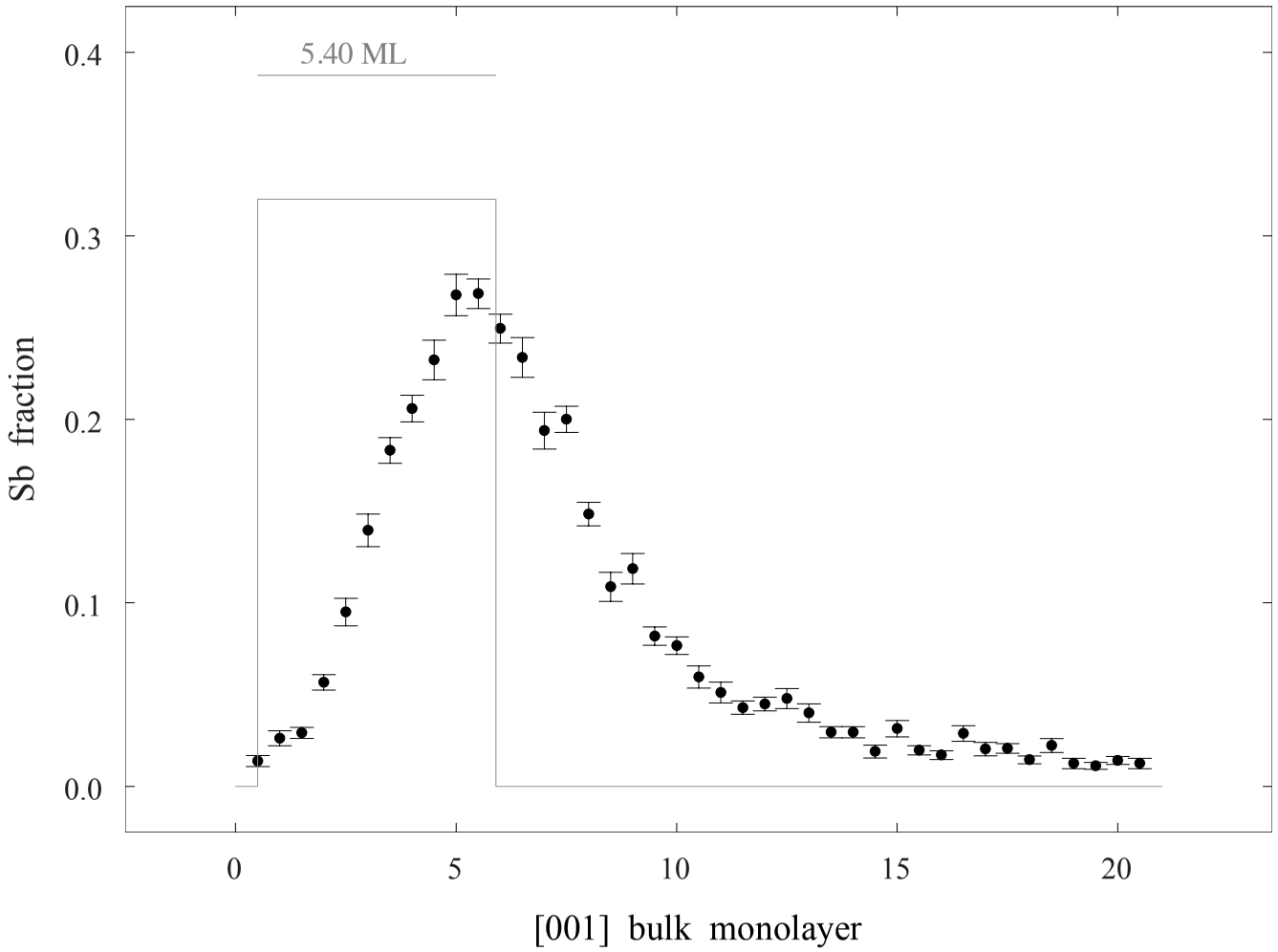

FIGURE 4.1. The compositionally–graded as–grown antimony profile reconstructed from STM, reproduced from Fig. 3.18. The intended profile, overlaid in grey, has width (d) 5.4 ML and steady–state height (x_{ss}) 0.33.

increases, molecules will leak around the shutter forming an unwanted ambient background, which will then compete with the intended anion stream for incorporation during growth.

To confirm segregation as the physical cause for the compositional grading observed at the interfaces in an InAs/InAsSb superlattice, it is essential to correctly model the segregation in these structures and analytically examine its resulting parameters. In an earlier study [8] performed by former members of this lab, antimony segregation was quantitatively investigated in a related system, InAs/GaInSb. Two separate samples displayed the expected geometric progression in antimony fraction due to segregation, and the profiles were fit using an adaptation of a segregation model developed by Muraki et al [51]. The original model can be summarized by the pair of equations

$$\begin{aligned} x_n &= x_{ss}\left(1-R^n\right) \qquad (1 < n < N) \\ x_n &= x_{ss}\left(1-R^n\right)R^{n-N} \quad (n > N) \end{aligned} \tag{4.1a}$$

$$R = \exp\left(-\frac{1\,\mathrm{ML}}{\lambda}\right) \tag{4.1b}$$

where x_{ss} represents the steady–state antimony fraction, N the integer number of monolayers in the intended antimonide layer, and R the corresponding segregation coefficient, equivalently parameterized in terms of a segregation length λ (in monolayers). All variables in Eq. (4.1a) are dimensionless, and both n and N presumed integer.

The original discrete formulation is problematic for a fractional monolayer period where each surface repeat samples only a portion of the bulk layer sequence. We therefore employed a continuum generalization of Muraki's model [46] to accommodate the non–integer period of the InAs/InAsSb superlattice examined in this study by way of

$$x(z) = x_{ss}\left(1 - \exp\left(-\frac{z}{\lambda}\right)\right) + x_0 \qquad (0 < z < d)$$
$$x(z) = x_{ss}\left(1 - \exp\left(-\frac{z}{\lambda}\right)\right)\exp\left(-\frac{z-d}{\lambda}\right) + x_0 \qquad (d < z < \Lambda) \tag{4.2}$$

Here, x_{ss} again represents the steady–state antimony fraction, z is now a continuously–varying coordinate along the growth direction, d the duration of a (presumed) spatially–invariant antimony exposure, Λ the superlattice period, λ a segregation length, and x_0 a constant background due to cross–incorporation. The variables z, d, λ, and Λ have dimensions of monolayers, while x_{ss} and x_0 are dimensionless.

To fit our profiles with the continuum segregation model, we employed a data analysis and graphing software package [52] equipped to run non–linear regressions. We first applied the segregation model to fit our antimony profiles using the bulk period approximations discussed in Chapter III. Fits with the appropriately constrained bulk period (Λ = 20.50 or 20.67 ML), describe the profiles reasonably well (Fig. 4.2, blue curve)[11]. This agreement provides persuasive confirmation that antimony segregation and cross–incorporation are indeed the physical mechanisms driving the compositional

[11] This profile (42 points) was folded–back with the 20.50 bulk period approximation following the algorithm outlined in Eq. (3.5).

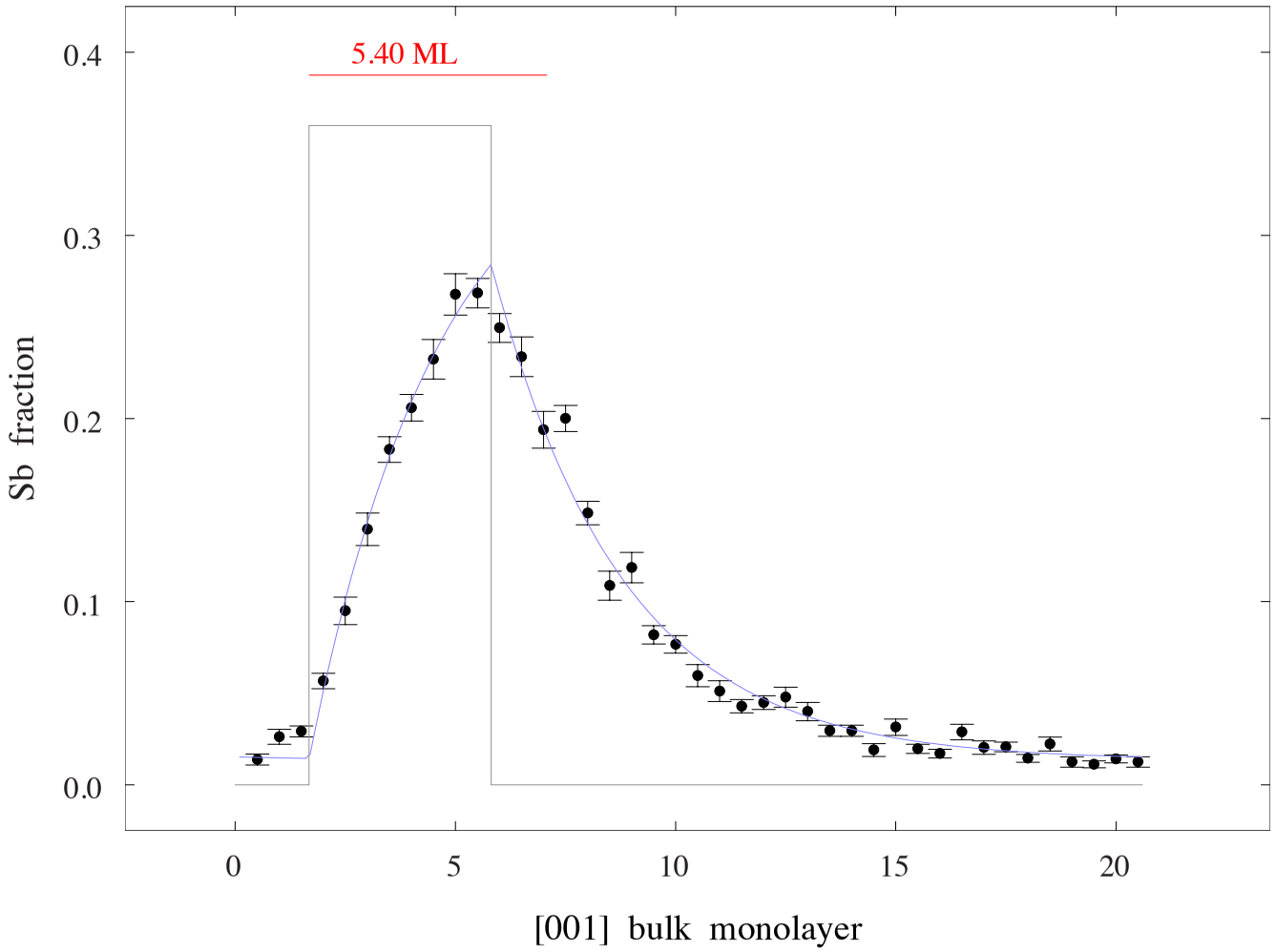

FIGURE 4.2. The as–grown antimony profile from STM, reconstructed with a bulk period approximation of 20.50 ML. Continuum segregation fit (Eq. 4.2) is illustrated by the blue curve. The implied source, overlaid in grey, has width (d) 4.0 ML, short of the intended 5.4 ML, and steady–state height (x_{ss}) 0.36, higher than the intended antimony fraction of 0.33.

grading across our superlattice interfaces and asymptotic antimony fractions, respectively.

Closer examination of Fig. 4.2, however, indicates such fits fail to properly capture the detailed shape of the antimony profile as it peaks, and this deficiency was shared by all lateral surveys. Furthermore, the source profile implied by the fit parameters, here, (Fig. 4.2, grey curve) is both too short and too intense compared with the intended source in Fig. 4.1.

Variable–Period Segregation Model

To ascertain whether these discrepancies are due to the segregation model itself or instead due to our bulk period approximations, we next permitted the bulk superlattice period, Λ, to be an additional fit variable thereby decoupling the two issues. Focusing now on each repeat[12], m, of the surface profile, the appropriately relaxed form of Eq. (4.2) then follows as

$$\begin{aligned} x(z) &= x_{ss}\left(1-\exp\left(-\frac{z}{\lambda}\right)\right)+x_0 && \left((m-1)\Lambda < z < (m-1)\Lambda + d\right) \\ x(z) &= x_{ss}\left(1-\exp\left(-\frac{z}{\lambda}\right)\right)\exp\left(-\frac{z-d}{\lambda}\right)+x_0 && \left((m-1)\Lambda + d < z < m\Lambda\right) \end{aligned} \tag{4.3}$$

Fits to the antimony profiles based on Eq. (4.3) yield an optimal peak spacing (superlattice period) for each lateral survey. As shown in Fig. 4.3, many of the values aren't far from the sliding average values (Chapter III), but in some cases our original

[12] The surface repeat, m, varies from 1 – 6 (Fig. 3.5), and is described in relation to the bulk period Λ in Chapter III, Eq. (3.5).

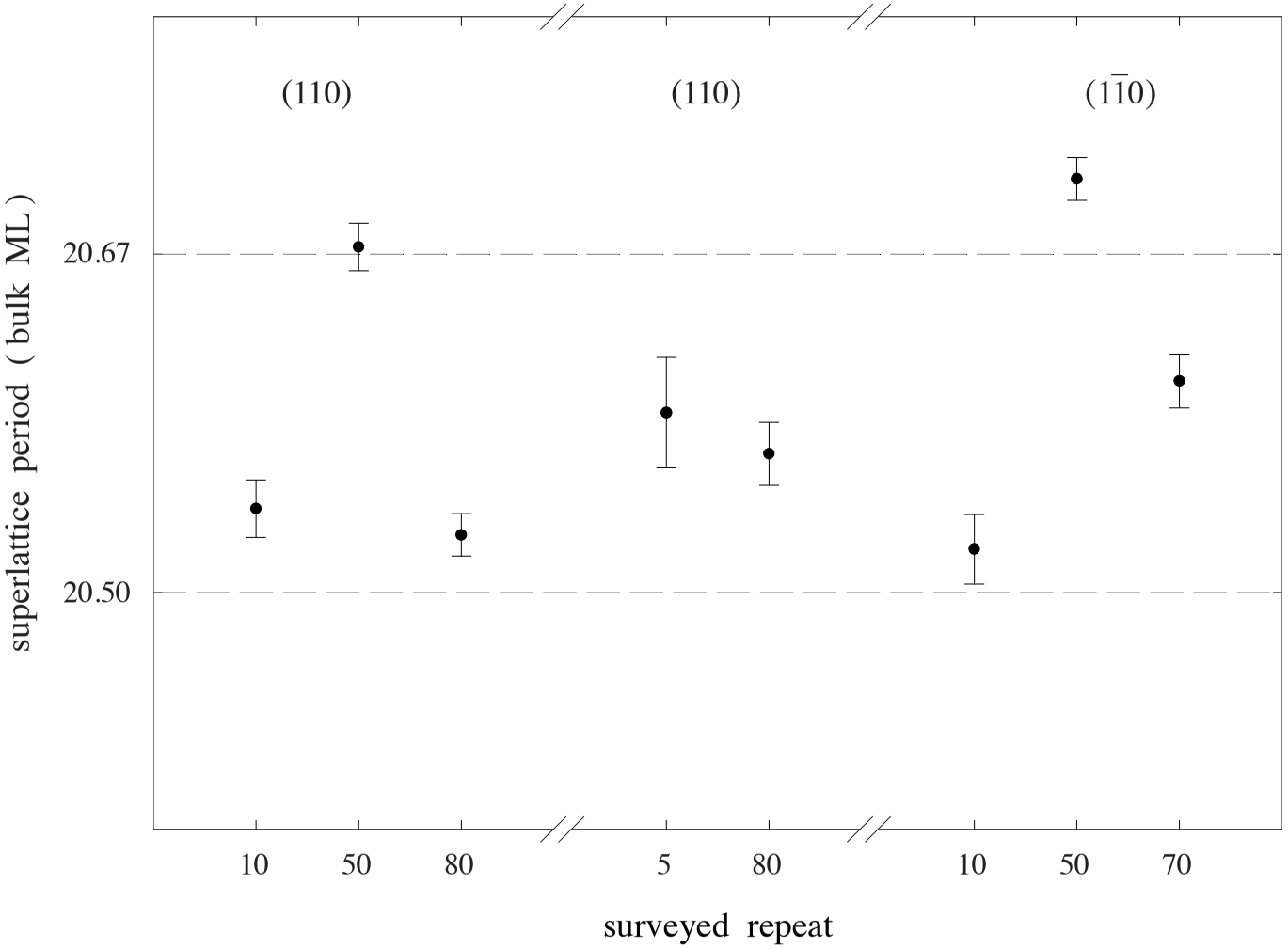

FIGURE 4.3. Direct comparison of the survey–average superlattice periods (Λ) deduced from a variable–period, continuum segregation model (closed circles, Eq. 4.3) or sliding–window average (dashed lines, Fig. 3.10). Each lateral survey is centered about the indicated repeat in the multilayer stack.

bulk–period approximation is outside error. These results nevertheless confirm that more than one bulk period is present in the multilayer stack.

Examination of the fit to the data for one lateral survey (Fig. 4.4, blue)[13] shows the variable–period segregation model provides a marginally better description of the data than the constrained–period model, and this is true of all lateral surveys. The average width (d) of the implied source across all surveys is 4.72 ± 0.03 ML (Fig. 4.5), which is still short of the intended 5.4 ML (Fig. 3.1). The corresponding average steady–state height (x_{ss}) of the implied antimony source is 0.307 ± 0.002 (Fig. 4.6), which is close to the intended 0.33.

Two–Source Segregation Analysis

One remaining adjustment to our model is to include a second segregation source, spatially offset from the first[14], to account for the possibility of interface roughness or a vicinal substrate, where the presence of terraces can create separate starting points for the segregation process. This two–source segregation model, with $x(z) = x_1(z) + x_2(z)$, is encapsulated by the following four equations

[13] This profile (62 points) was folded–back with the period determined by the variable–period segregation model following the algorithm outlined in Eq. (3.5).

[14] That is, a second spatial origin for the antimony segregation, not a second antimony effusion cell.

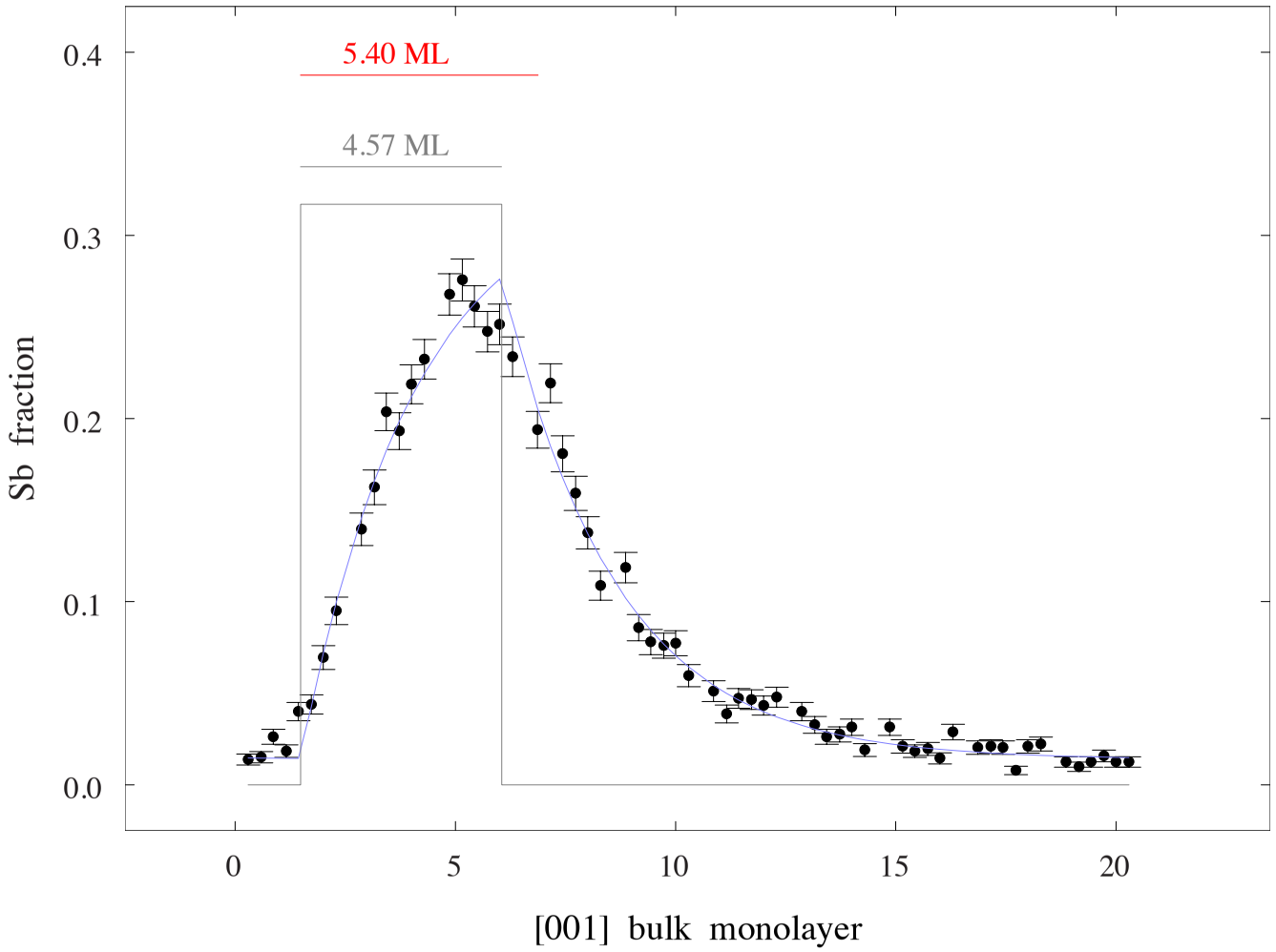

FIGURE 4.4. The as–grown antimony profile, reconstructed with a bulk period of 20.57 ML from a variable–period continuum segregation fit (Eq. 4.3), overlaid in blue. The implied source, overlaid in grey, has width (d) 4.57 ML, short of the intended 5.40 ML, and steady–state height (x_{ss}) 0.32, in good agreement with the intended antimony fraction of 0.33.

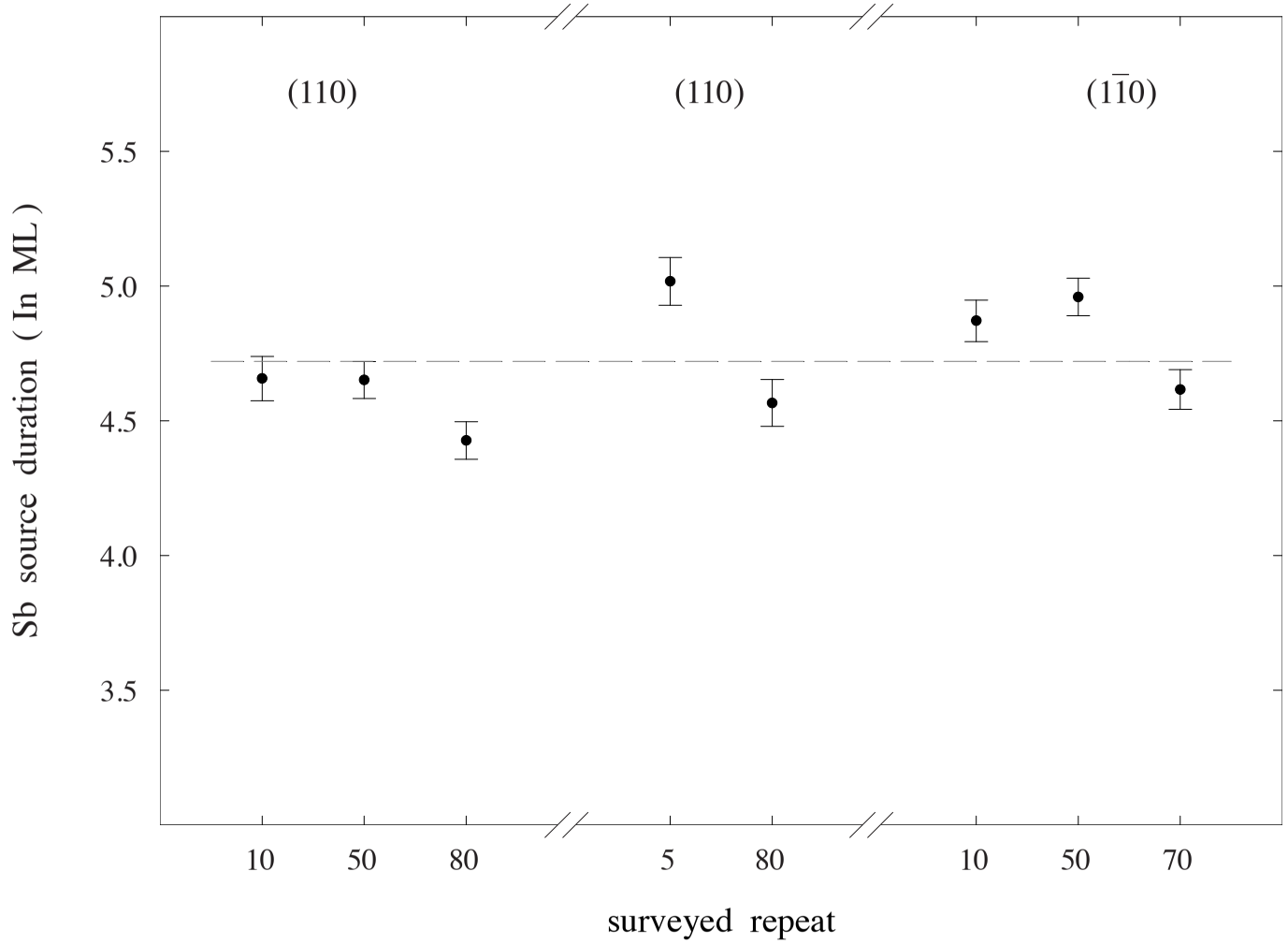

FIGURE 4.5. Source widths (d) deduced from variable–period, continuum segregation fits (Eq. 4.3). Each lateral survey is centered about the indicated repeat in the multilayer stack. Dashed line indicates an average value of 4.72 ML.

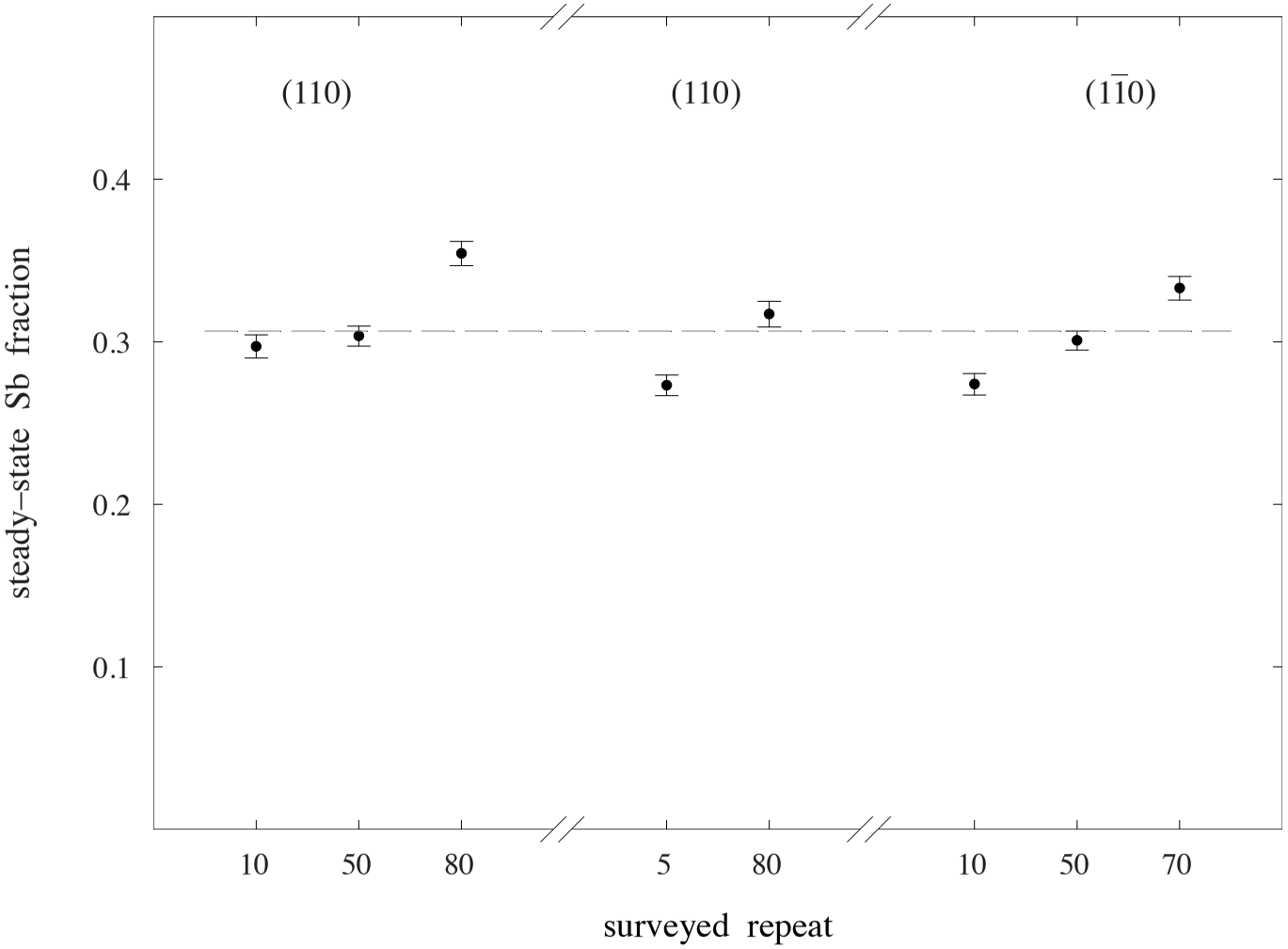

FIGURE 4.6. Steady–state source intensities (x_{ss}) deduced from variable–period, continuum segregation fits (Eq. 4.3). Each lateral survey is centered about the indicated repeat in the multilayer stack. Dashed line indicates an average value of 0.307.

$$
\begin{aligned}
x_1(z) &= \alpha\, x_{ss}\left(1-\exp\left(-\frac{z}{\lambda}\right)\right) + x_0 && \left((m-1)\Lambda < z < (m-1)\Lambda + d\right) \\
x_1(z) &= \alpha\, x_{ss}\left(1-\exp\left(-\frac{d}{\lambda}\right)\right)\exp\left(-\frac{z-d}{\lambda}\right) + x_0 && \left((m-1)\Lambda + d < z < m\Lambda\right) \\
x_2(z) &= (1-\alpha)\, x_{ss}\left(1-\exp\left(-\frac{\zeta}{\lambda}\right)\right) + x_0 && \left((m-1)\Lambda < \zeta < (m-1)\Lambda + d\right) \\
x_2(z) &= (1-\alpha)\, x_{ss}\left(1-\exp\left(-\frac{d}{\lambda}\right)\right)\exp\left(-\frac{\zeta-d}{\lambda}\right) + x_0 && \left((m-1)\Lambda + d < \zeta < m\Lambda\right)
\end{aligned}
\tag{4.4}
$$

where $\zeta = z + \phi$, ϕ is the spatial offset between source origins (in monolayers), α the fraction of the steady–state antimony contributed by the first source, and (1–α) the corresponding amount contributed by the second source. The physical content of this model is illustrated in Fig. 4.7, where the spatially–distinct starting points for the individual profiles (and corresponding implied sources), along with the common width *d* of the implied sources[15] are highlighted.

Applying this two–source continuum segregation model to the antimony profiles, we find it describes the data with persuasive accuracy, including the previously problematic shape near the peak of the curve (Fig. 4.8, blue)[16]. The values of ϕ that emerge from the two–source segregation fits average 1.09 ± 0.06 ML (Fig. 4.9), which

[15] Requiring the individual source widths to be the same is a reasonable assumption if a roughness model is physically correct; the fits furthermore do not converge if this constraint is relaxed.

[16] This profile (62 points) was constructed following the algorithm in Eq. (3.5), with the period determined by the two–source segregation model.

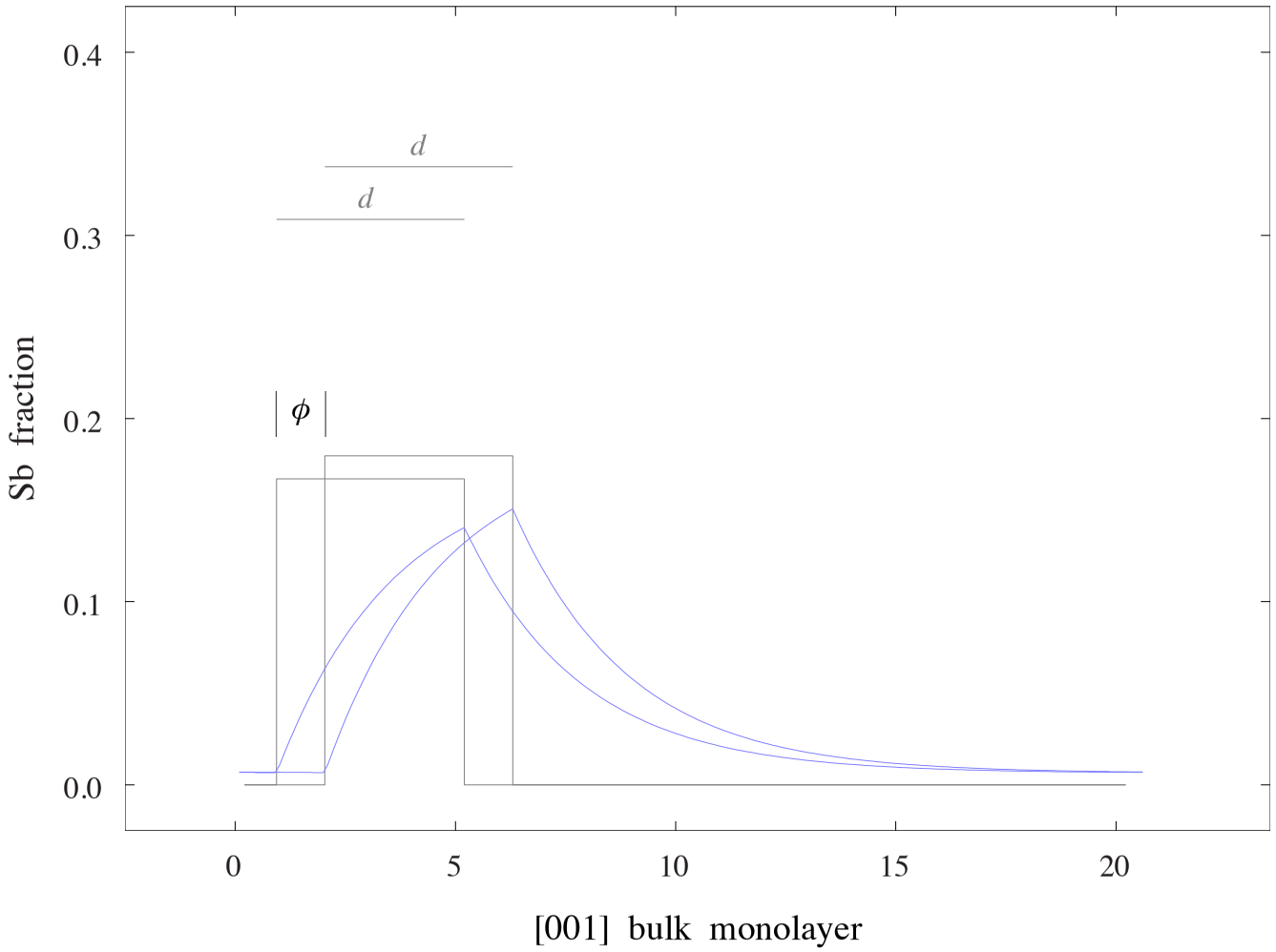

FIGURE 4.7. Individual profiles with spatially offset (ϕ) starting points from a two–source continuum segregation model (Eq. 4.4) illustrated in blue, and their corresponding implied sources, overlaid in grey, with common width d.

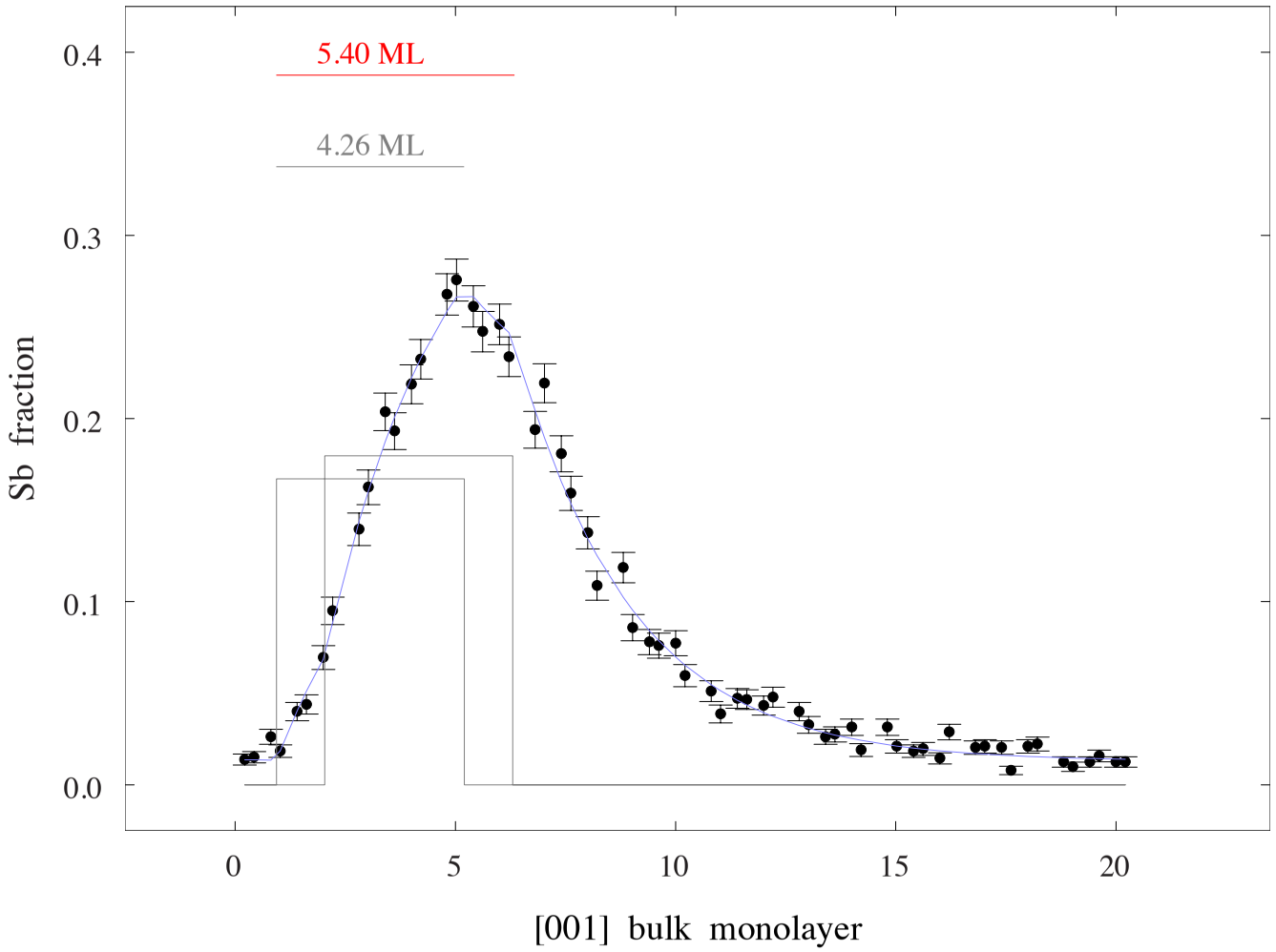

FIGURE 4.8. The as–grown antimony profile from STM, reconstructed with a bulk period of 20.60 ML from a two–source continuum segregation fit (Eq. 4.4), overlaid in blue. The common width (d) of the implied sources, overlaid in grey, is 4.26 ML, short of the intended 5.4 ML.

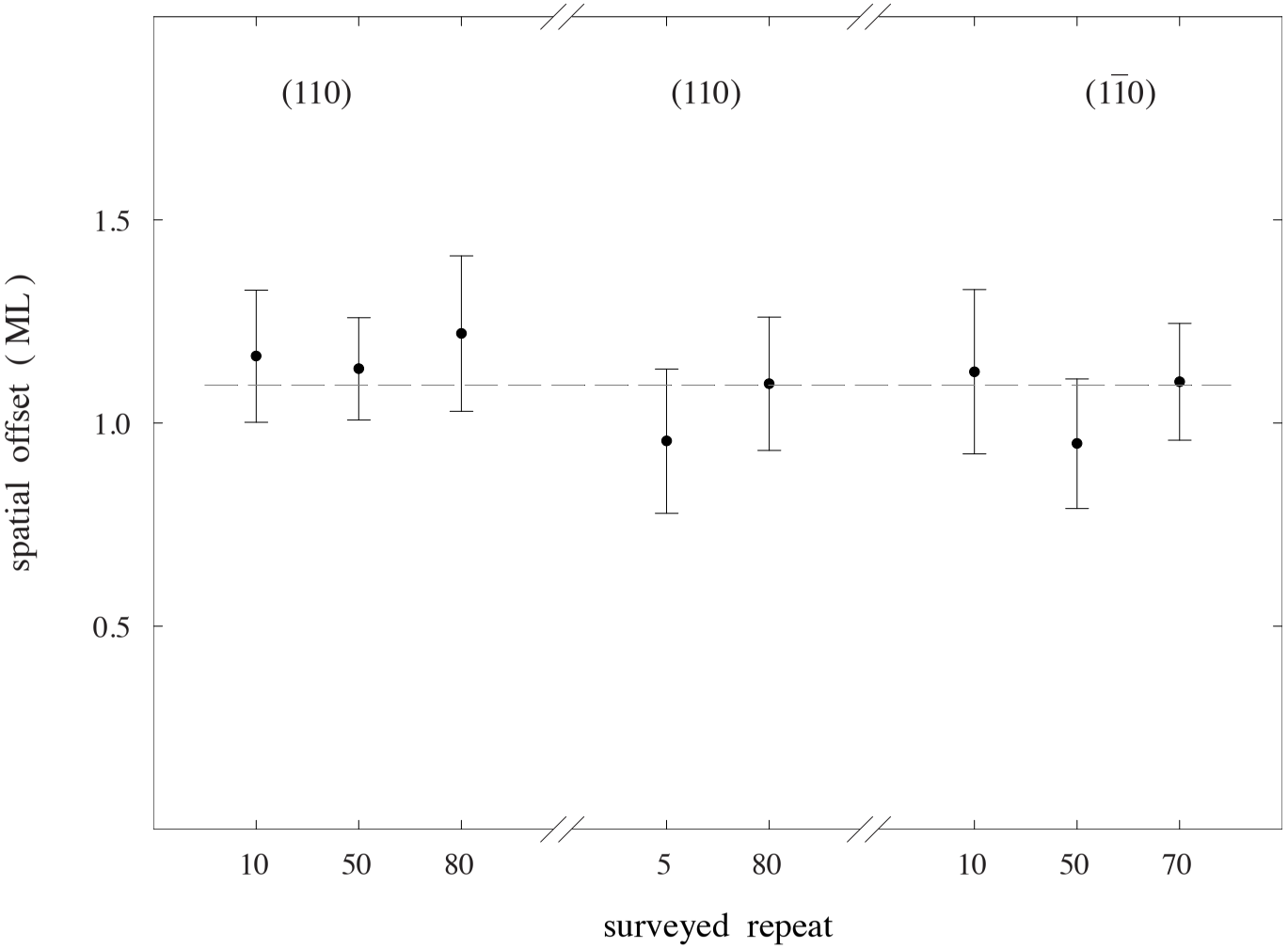

FIGURE 4.9. Spatial offset (ϕ) between segregation sources of a two–source, continuum segregation fit (Eq. 4.4). Each lateral survey is centered about the indicated repeat in the multilayer stack. Dashed line indicates an average value of 1.09 ML.

supports the physical motivation (i.e. monolayer roughness or vicinal substrate) for this generalization to the segregation model. Finally, the best–fit superlattice periods (Fig. 4.10) are within error of the periods determined from single–source fits and thus, again, in reasonable agreement with our sliding–window approximations.

The common pulse width, d, for the implied sources (Fig. 4.8, grey) has an average over all surveys of 4.46 ± 0.04 ML (Fig. 4.11), within error of the single–source pulse width average. The steady–state height, x_{ss}, and steady–state fraction provided by a single source, α, have respective averages of 0.330 ± 0.003 (Fig. 4.12) and 0.38 ± 0.02 (Fig. 4.13). The unresolved discrepancy between source widths determined from the segregation model (4.46 ± 0.04 ML) and growth–rate calibrations performed by Sandia (5.40 ML) is not understood at this time.

Parameters obtained from our continuum segregation model can also be used to determine the values of the antimony segregation coefficient (R) and constant background (x_0), which have potential predictive value for related structures. The segregation coefficient, expressed in Eq. (4.1b), and the background have respective averages of 0.671 ± 0.003 (Fig. 4.14) and 1.28 ± 0.03 % (Fig. 4.15)[17].

HRXRD Simulations

To establish the results of our fits with the continuum segregation model are characteristic of the superlattice structure as a whole, we once more turn to dynamical x–

[17] The average values for the segregation coefficient and background are in good agreement with those reported in [7].

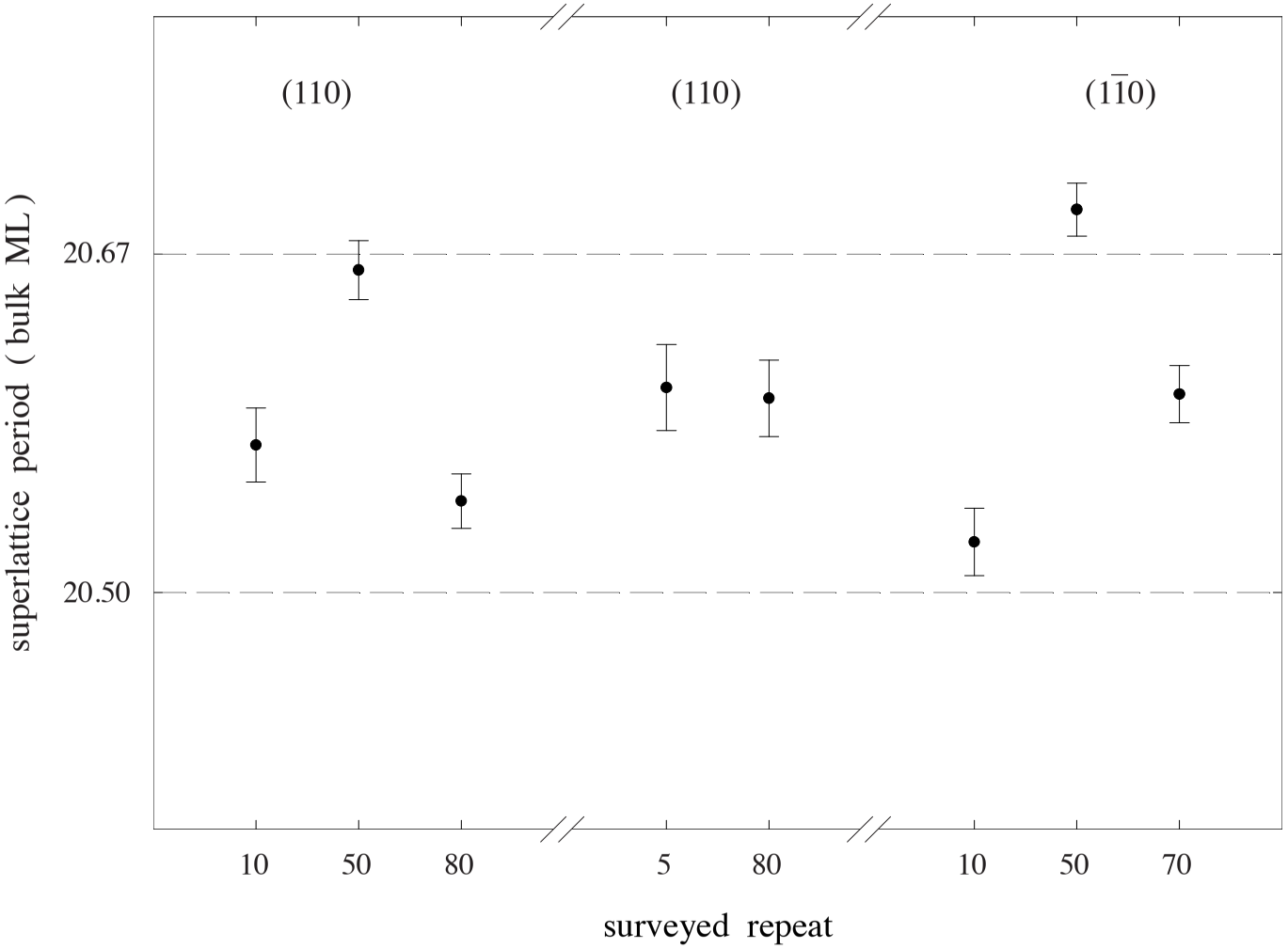

FIGURE 4.10. Direct comparison of the survey–average superlattice periods (Λ) deduced from a two–source, continuum segregation model (closed circles, Eq. 4.4) or sliding–window average (dashed lines, Fig. 3.10). Each lateral survey is centered about the indicated repeat in the multilayer stack.

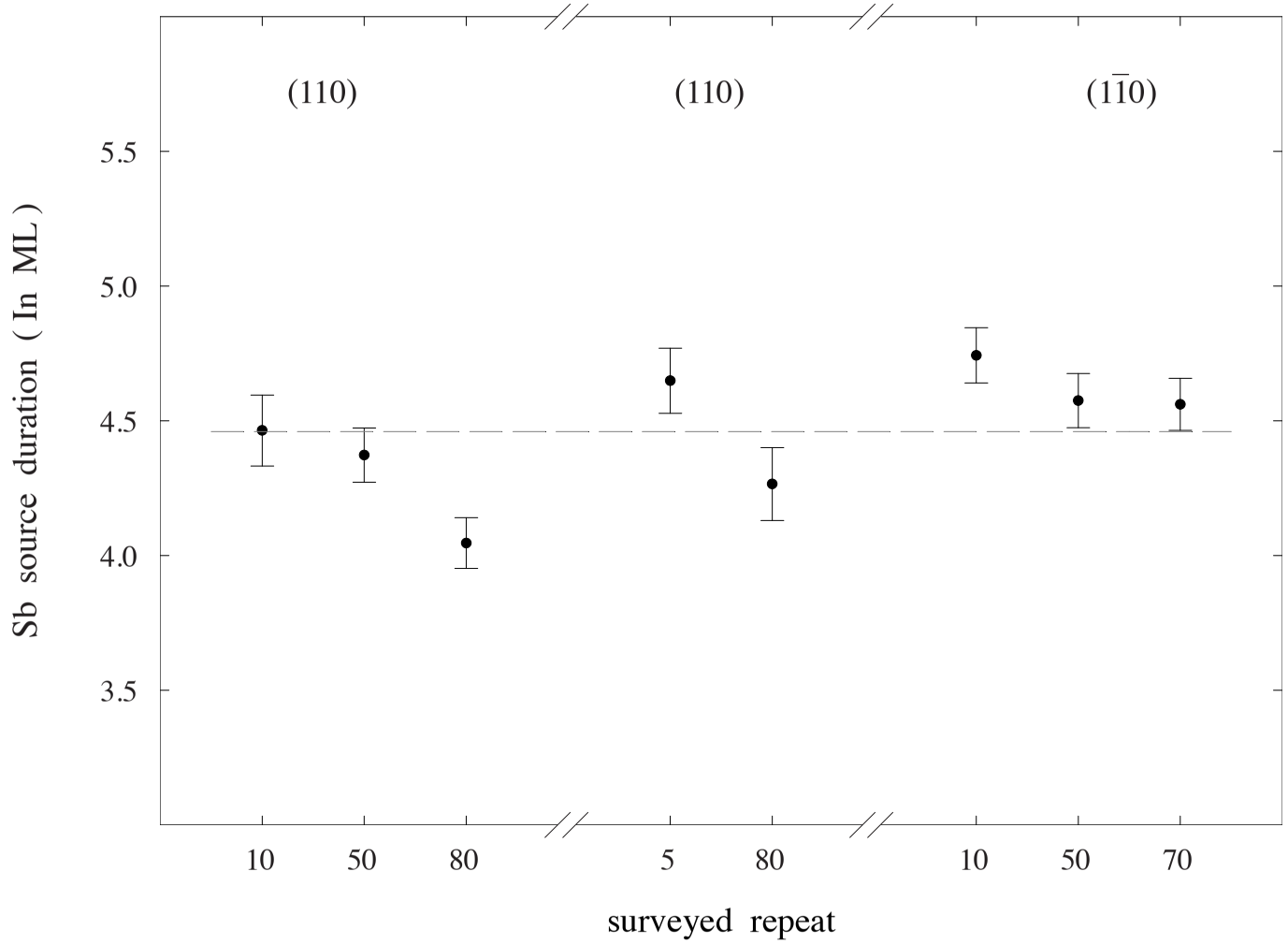

FIGURE 4.11. Source widths (d) deduced from two–source, continuum segregation fits (Eq. 4.4). Each lateral survey is centered about the indicated repeat in the multilayer stack. Dashed line indicates an average value of 4.46 ML.

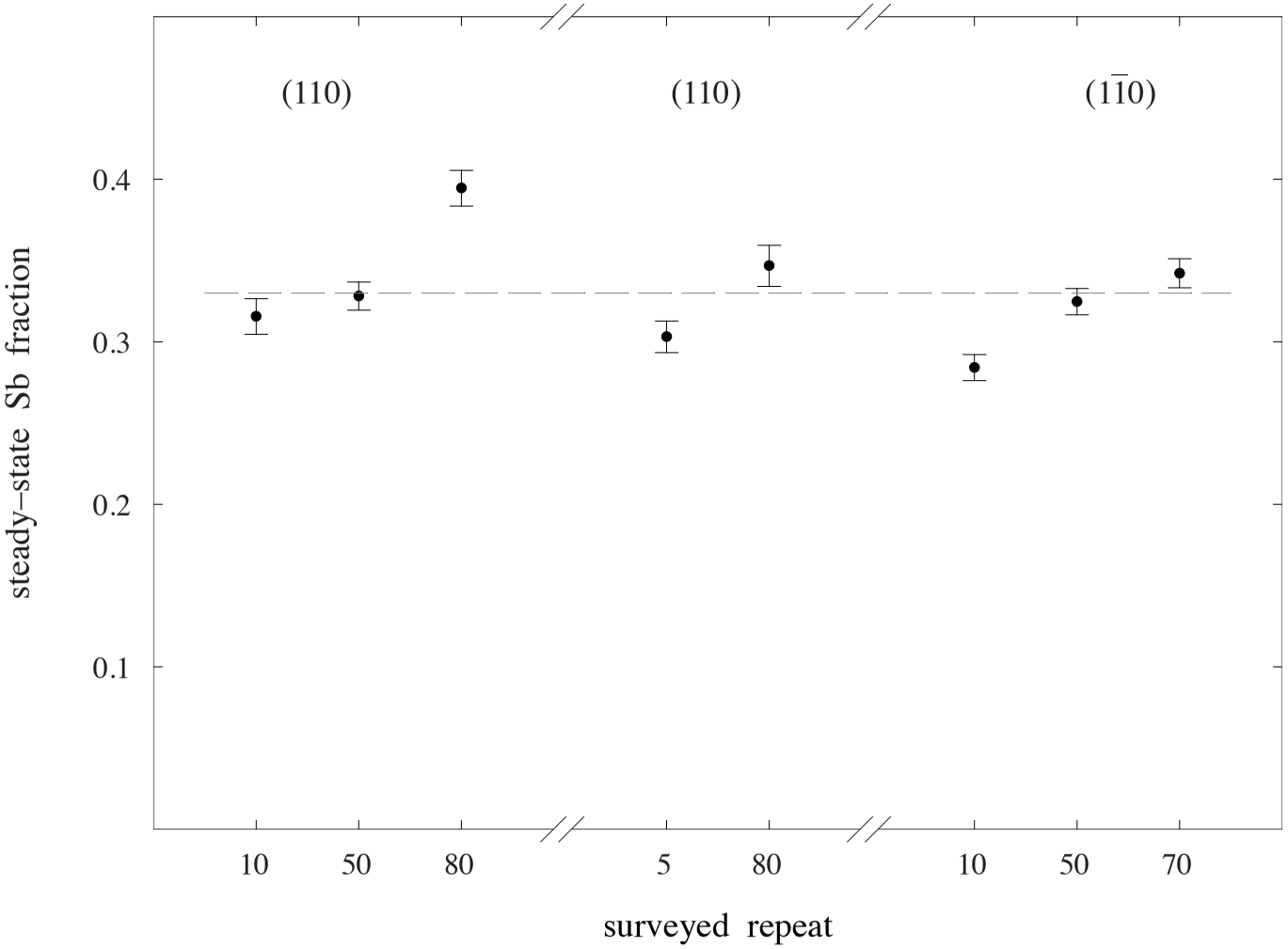

FIGURE 4.12. Steady–state source intensities (x_{ss}) deduced from two–source, continuum segregation fits (Eq. 4.4). Each lateral survey is centered about the indicated repeat in the multilayer stack. Dashed line indicates an average value of 0.330.

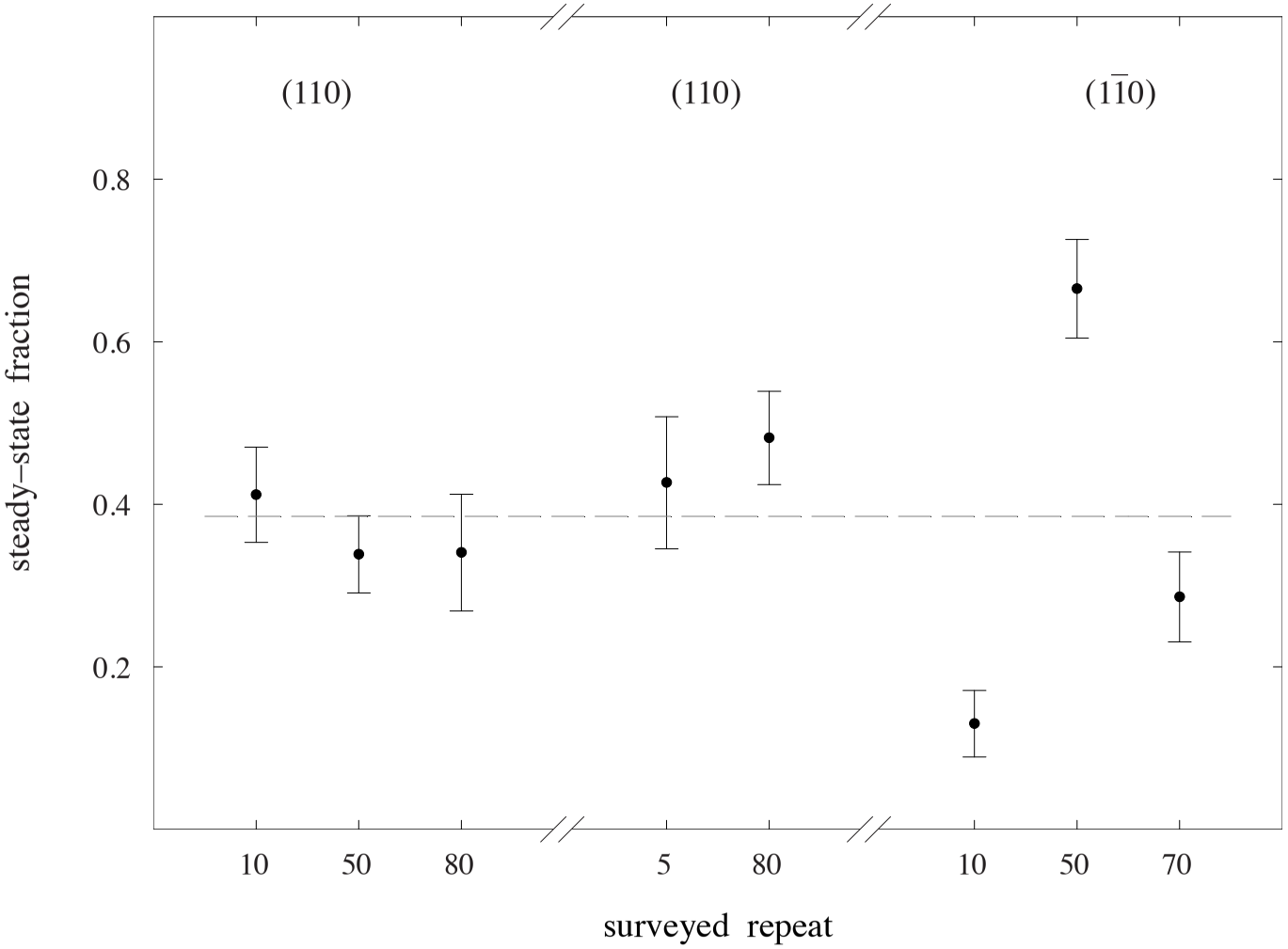

FIGURE 4.13. The fraction of steady–state source intensity (α) provided by one source of a two–source, continuum segregation fit (Eq. 4.4). Each lateral survey is centered about the indicated repeat in the multilayer stack. Dashed line indicates an average value of 0.38.

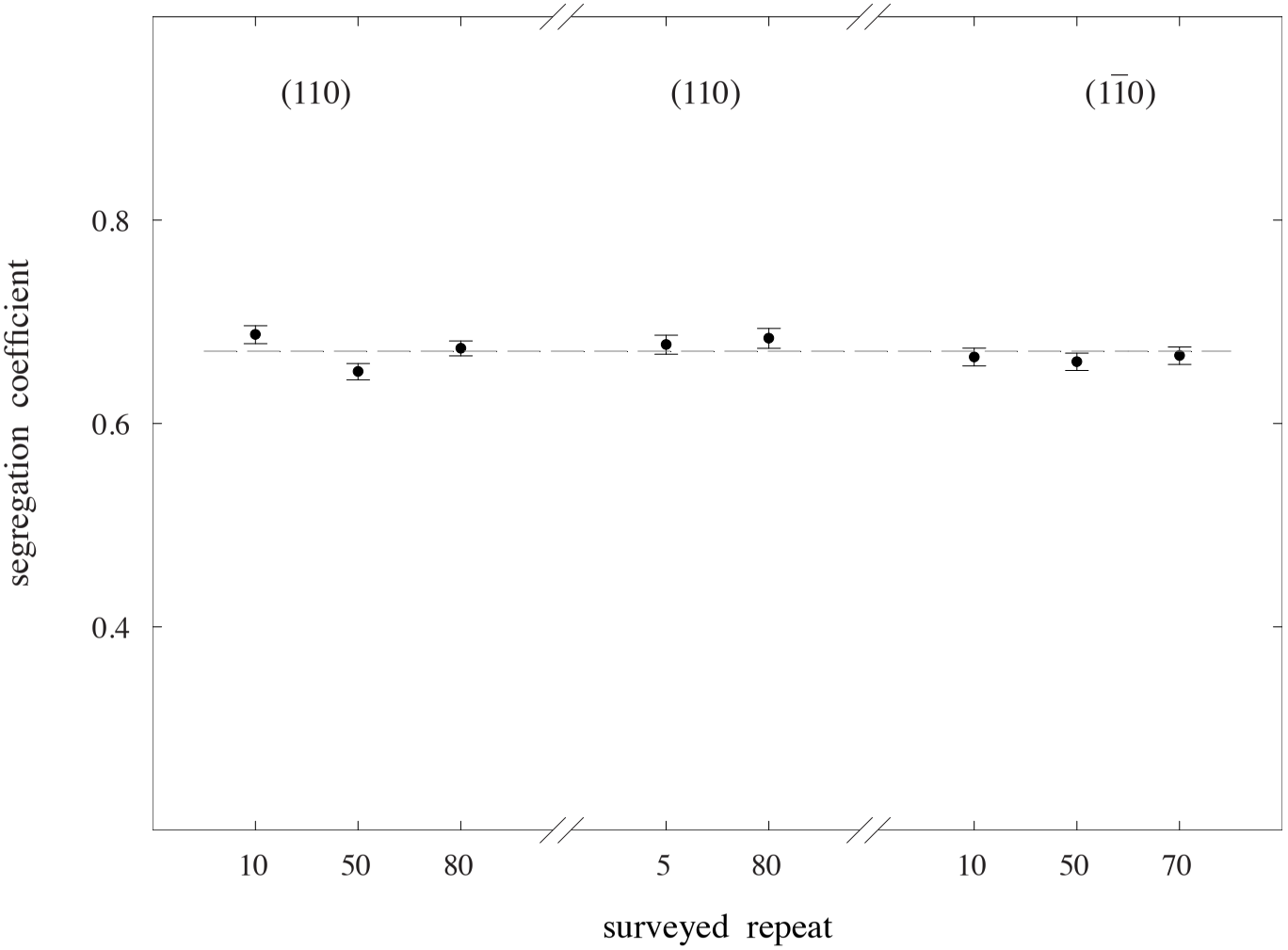

FIGURE 4.14. Antimony segregation coefficients (R) calculated from two–source, continuum segregation fits (Eq. 4.4). Each lateral survey is centered about the indicated repeat in the multilayer stack. Dashed line indicates an average value of 0.671.

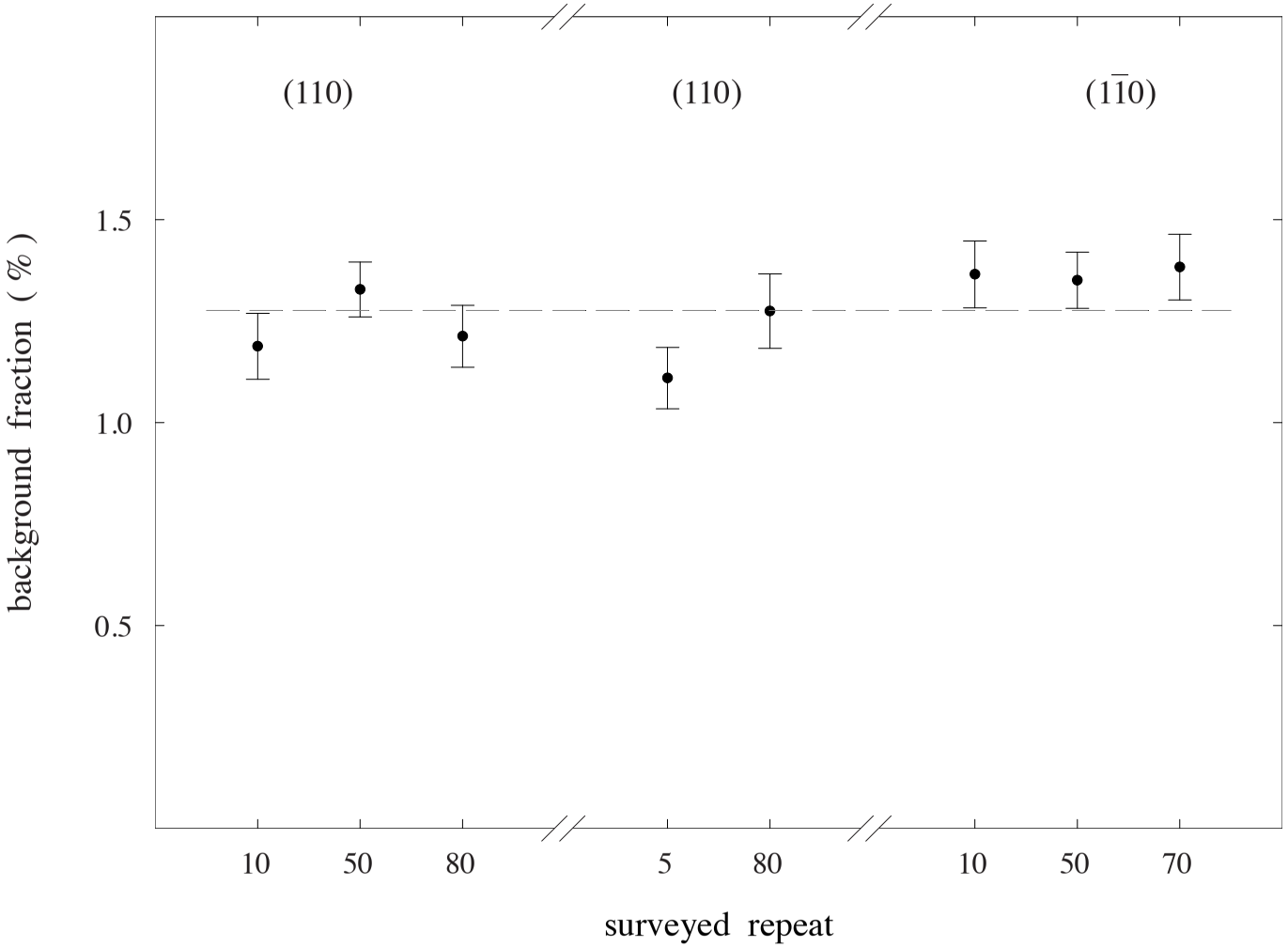

FIGURE 4.15. Antimony backgrounds (x_0) deduced from two–source, variable–period segregation fits (Eq. 4.4). Each lateral survey is centered about the indicated repeat in the multilayer stack. Dashed line indicates an average value of 1.28%.

ray simulations [44]. As discussed in Chapter III, the simulated spectrum of the intended structure (Fig. 4.16) fails to correctly describe the satellite peak intensities of the experimental HRXRD spectrum, as well as the broadening at the base of each peak. When we rely instead on the reconstructed antimony profile to generate a simulation, we see a marked improvement in the description of the experimental x–ray data (Fig. 4.17). Not surprisingly (since these reconstructed profiles were based on approximations to the bulk period) there are remaining differences between the simulated and experimental spectra.

With the two–source continuum segregation model, we can not only accurately account for segregation and cross–incorporation throughout the structure, but determine a self–consistent period for each lateral survey as well. We can also consider the role played by any evolution in incorporated antimony fraction as noted in Chapter III (Figs. 3.11 – 3.13), in refining our x–ray simulations. To this end, a small piece, previously used for x–ray analysis, was selected for depth profiling with secondary ion mass spectrometry (SIMS)[18]. The SIMS data are plotted in Fig. 4.18 as a moving average over nine periods (sienna line), and they support the STM results concerning the increase in average antimony fraction from initiation to completion of growth.

We account for these SIMS and STM data by including a simple, piecewise constant approximation (Fig. 4.18, blue line) to the steady–state antimony fraction characterizing our two–source segregation model. The resulting x–ray spectrum (Fig. 4.19) provides an impressive description of the experimental HRXRD. All significant

[18] The SIMS measurement was performed by Evans Analytical Group.

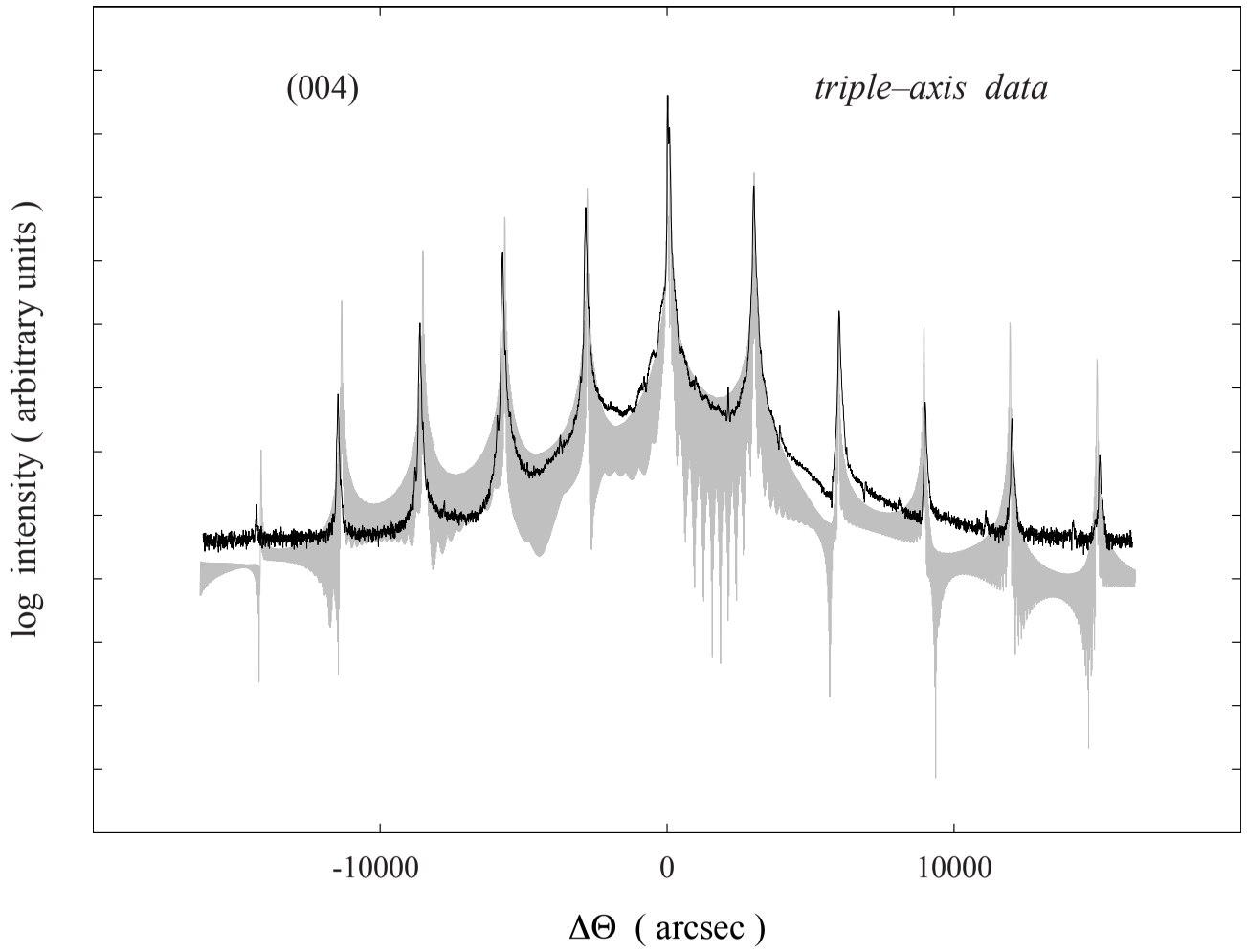

FIGURE 4.16 Comparison of dynamical x–ray simulation (normalized to the observed substrate peak intensity) assuming the intended composition in Fig. 3.1 (grey), with the experimental HRXRD spectrum (black); reproduced from Fig. 3.3.

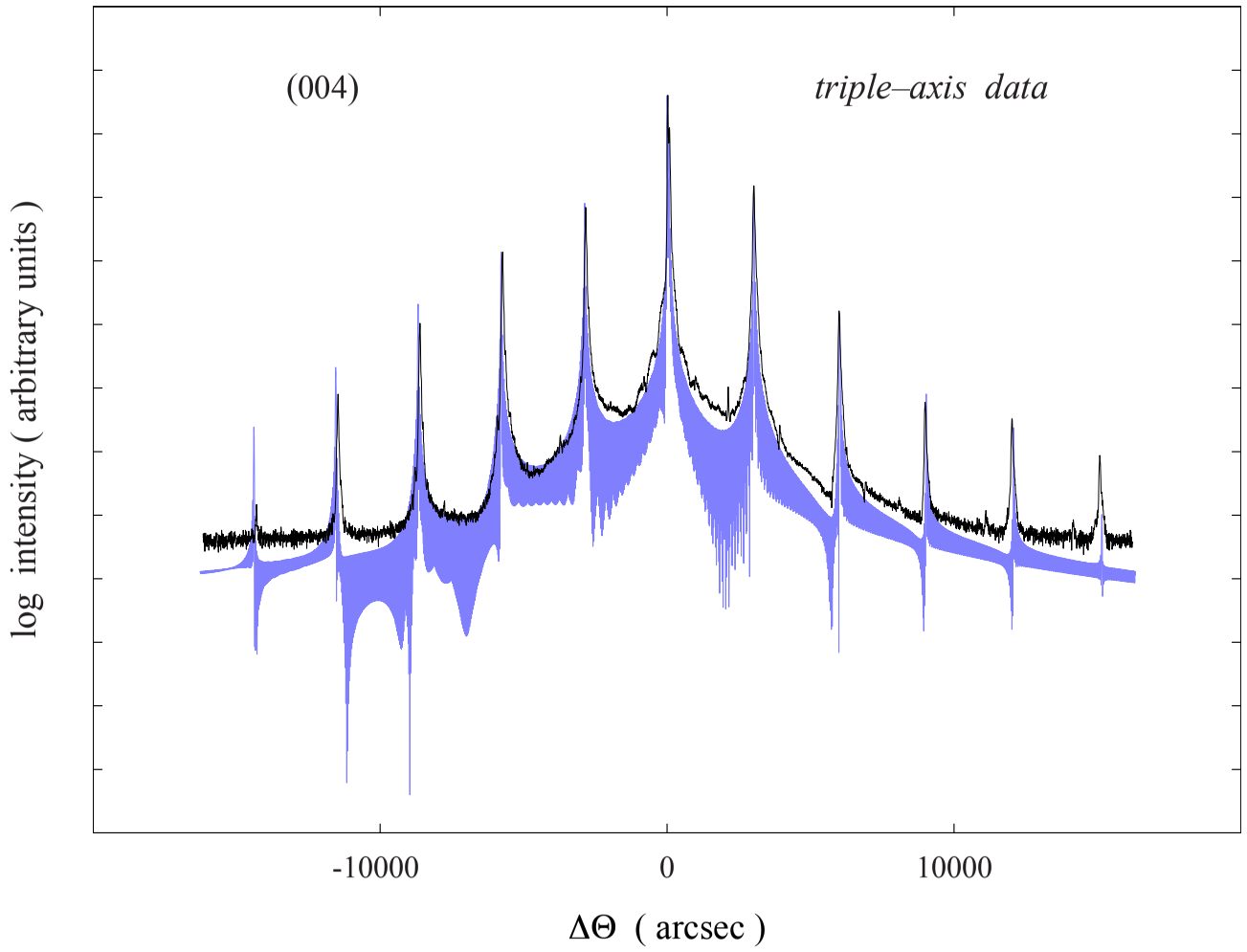

FIGURE 4.17. Comparison of dynamical x–ray simulation (normalized to the observed substrate peak intensity) assuming reconstructed as–grown profile with bulk period approximation deduced from STM (blue), with the experimental HRXRD spectrum (black); reproduced from Fig. 3.20.

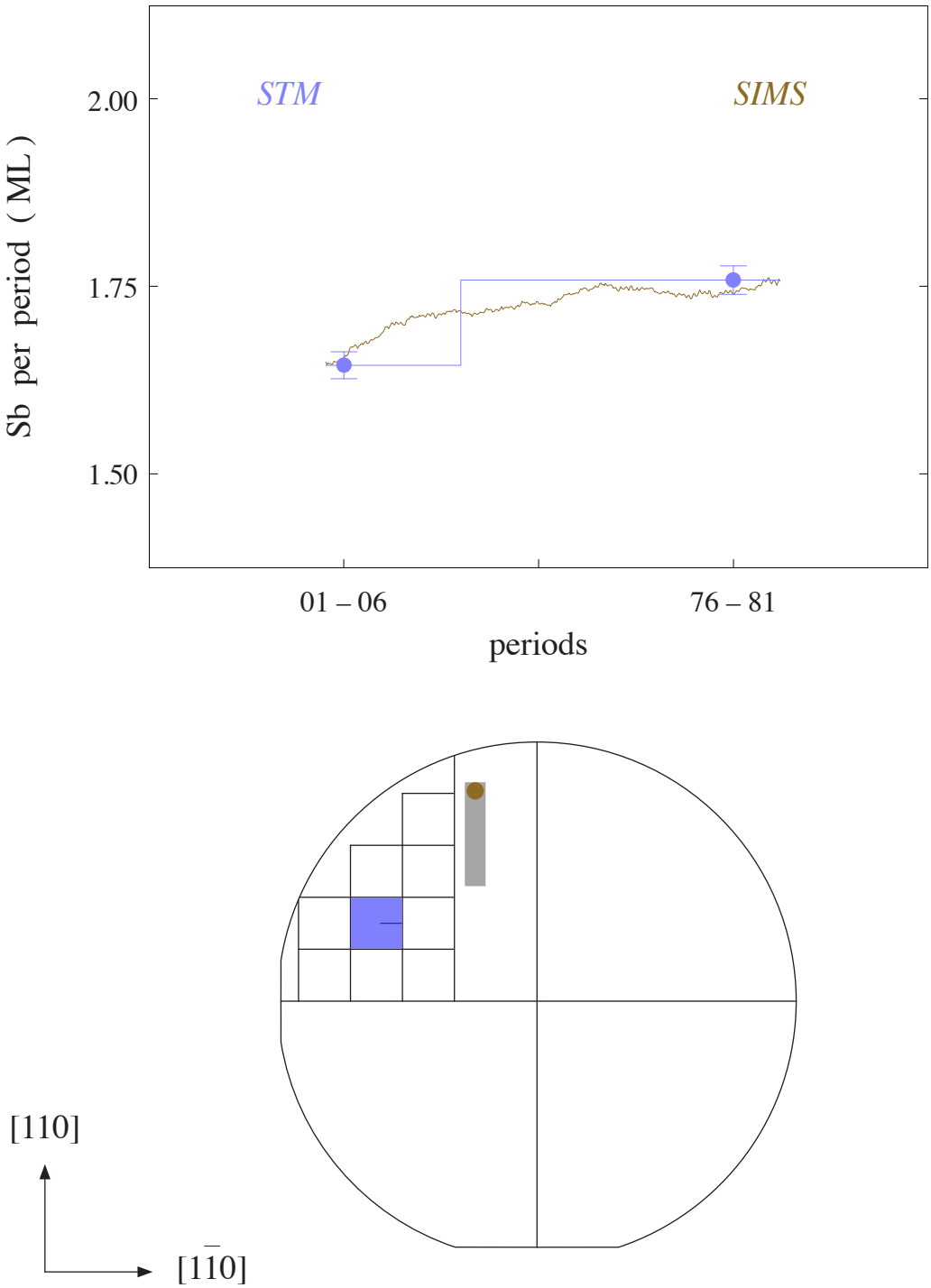

FIGURE 4.18. Depth profile from SIMS (sienna) agrees with observed increase in incorporated antimony from STM (blue points). A piecewise-constant approximation to the STM and SIMS data (blue line) is employed for x-ray simulation. Wafer diagram depicts location of the sample die (blue), SIMS measurement (sienna), and HRXRD (grey).

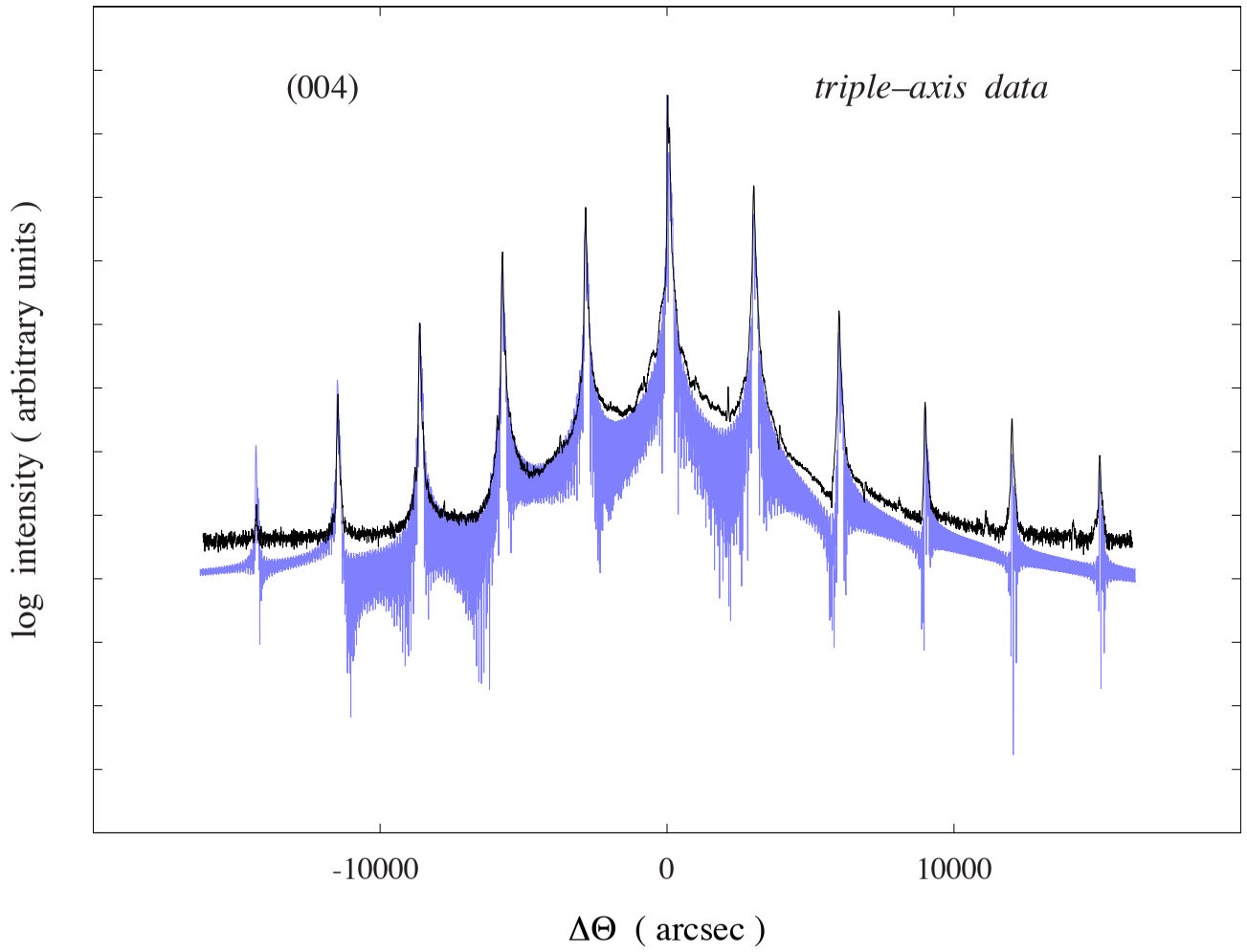

FIGURE 4.19. Dynamical x-ray simulation (normalized to the observed substrate peak intensity) assuming the continuum segregation fit to the as–grown antimony profile from STM, Fig. 4.8, as well as the piecewise–constant approximation illustrated in Fig. 4.18 (blue). Comparison with the experimental HRXRD spectrum (black) demonstrates an excellent global description of the observed x–ray mismatch, superlattice period, satellite peak intensities, peak widths, and overall background.

features of the x–ray data, including satellite peak intensities, peak widths, overall background, mismatch, and superlattice period, are now fully accounted for. This improvement is highlighted with the expanded views of Figs. 4.17 and 4.19 reproduced in Fig. 4.20.

Synopsis

Inspection of the InAs/InAsSb composition profiles established the existence of an interface asymmetry suggestive of anion segregation. We adapted a standard segregation model to accommodate for the non–integer period of our structure, and included an offset to account for cross–incorporation. This model provided a satisfactory fit to the profiles, thereby identifying a combination of antimony segregation and cross–incorporation as the physical origin of the observed compositional grading.

By removing the period approximation constraints imposed in Chapter III, we were able to use the segregation model to quantitatively analyze the superlattice period for each of the period subsets surveyed with STM. However, while the variable period model was an improvement, there were still notable discrepancies between the fit and the data. A second, spatially–distinct segregation source was then added, and it provided a superior description of the antimony profiles. The spatial offset between the two sources naturally settles on one monolayer, which is consistent with a vicinal substrate or interface roughness. However, the source widths determined by these fits disagree with the shutter timing (for antimony exposure) provided by the grower. This inconsistency is not understood at this time.

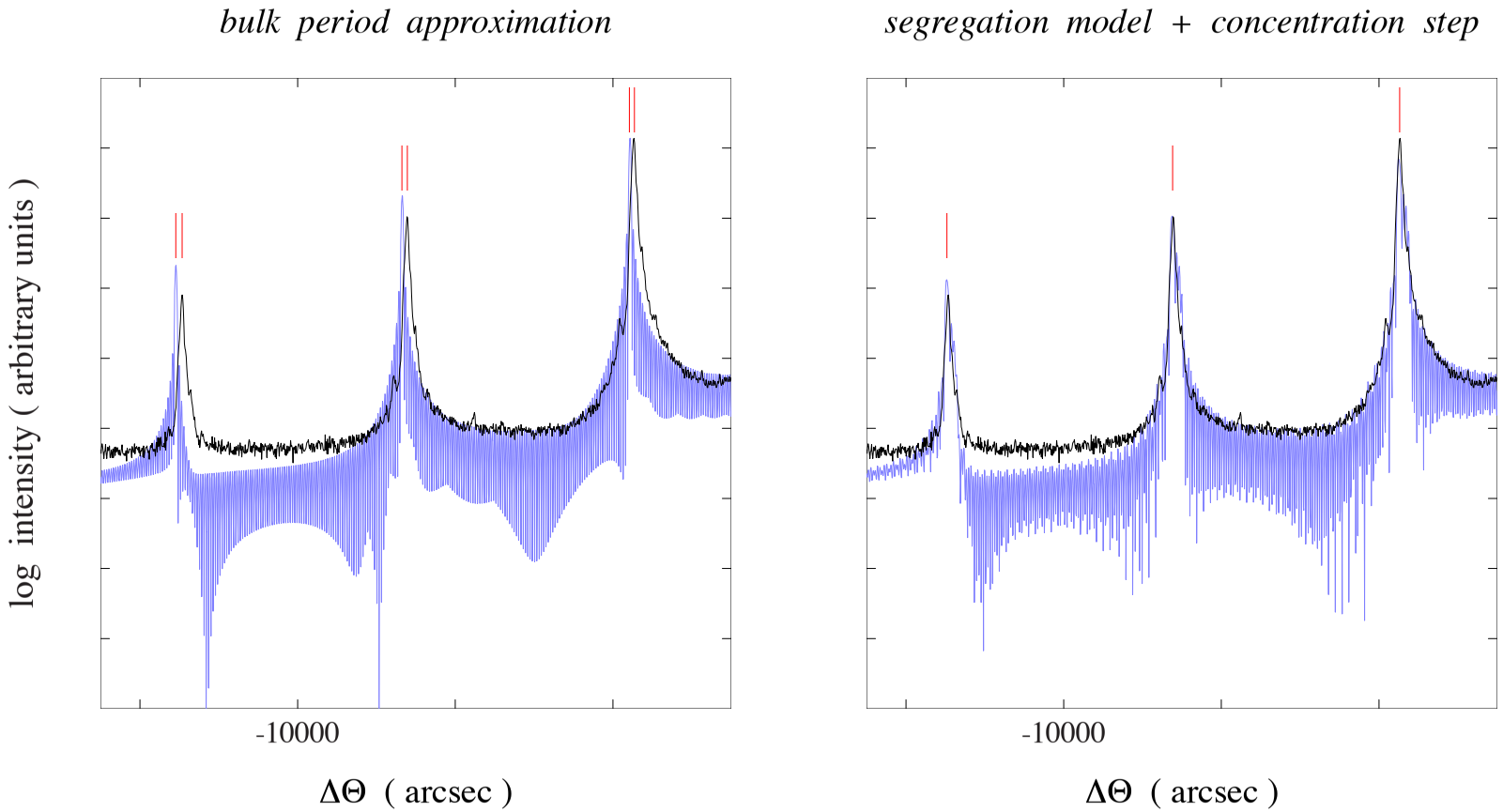

FIGURE 4.20. Expanded views of the –2, –3, –4 HRXRD satellites from Fig. 4.17 (left) and Fig. 4.19 (right). The combination of a piecewise–constant approximation to the vertical evolution in total antimony fraction per period (Fig. 4.18) with the two–source segregation model (Eq. 4.4) provides a decidely improved description of satellite peak intensities, peak widths, and superlattice period.

The systematic increase in incorporated antimony per period from beginning to end of the growth (observed with STM) was independently confirmed with SIMS. Combining this information with the compositional grading observed with STM in our dynamical x–ray simulations produced an impressively accurate match to the full, *as–grown* HRXRD spectrum. This makes a compelling argument that our compositional analysis with STM is characteristic of the superlattice as a whole.

CHAPTER V

PERIOD ANALYSIS

Introduction

In previous chapters, we have provided evidence of a small, but quantifiable variation in superlattice period from the beginning to end of epitaxial growth. Accurate knowledge of the *as–grown* superlattice period in multiple–quantum–well structures is important to the extent these deviations from design intentions adversely affect the overall optical properties in such devices. High–resolution x–ray diffraction (HRXRD) is conventionally used to assess the average superlattice period throughout the multilayer stack [43].

In principle, it is possible to learn something about period variations in the growth through careful examination of peak broadening in the HRXRD spectrum [43, 53]. Here, we also employ a new analytical method developed in the STM lab [23], which uses reciprocal–space maps from atomic–resolution STM images to accurately measure local heterostructure periods. We demonstrate the validity of this reciprocal–space method using our previous InAs/InAsSb superlattice period measurements – the sliding–average period approximations in Chapter III and the quantitative measurements deduced from the compositional profiles fit in Chapter IV – as independent checks.

Analysis of Period Variations from HRXRD

The (004) HRXRD analysis discussed in Chapter III, and reproduced, here, in Fig. 5.1, for easy reference, revealed an average superlattice period of 20.62 ± 0.01 ML for all 100 repeats in the multilayer stack. A peak fitting program [54] was used to determine the center of each satellite peak for this analysis by way of Gaussian fits.

All of the satellite peaks in the experimental spectrum are best described by more than one Gaussian component. One such example is the three–Gaussian fit illustrated in Fig. 5.2 for the second satellite from the left (compressive) side of the HRXRD spectrum. The blue curve represents the central portion of the satellite peak used for the aforementioned average–period measurement in Fig. 5.1 (bottom). The green and red curves may be interpreted as a broadening of this satellite due to fluctuations in the superlattice period at some point during the growth. The grey curve in Fig. 5.2 is the composite fit to these satellite data including all three Gaussian components. Separately applying Bragg's Law to the full set of small 'outer' peaks – those to the left of the compressive peaks in the HRXRD spectrum, along with those to the right of the tensile peaks – reveals a period of 20.53 ± 0.01 ML (Fig. 5.3, top), remarkably close to the 20.50 ML approximation employed in Chapter III. Applying Bragg's Law to the set of 'inner' peaks – those to the right of the compressive peaks along with those to the left of the tensile peaks – on the other hand, reveals a period of 20.69 ± 0.01 ML (Fig. 5.3, bottom), likewise close to the 20.67 approximation employed in Chapter III.

While these two measurements suggest more than one period within the superlattice, they offer no clues as to *where* these periods occur within the multilayer

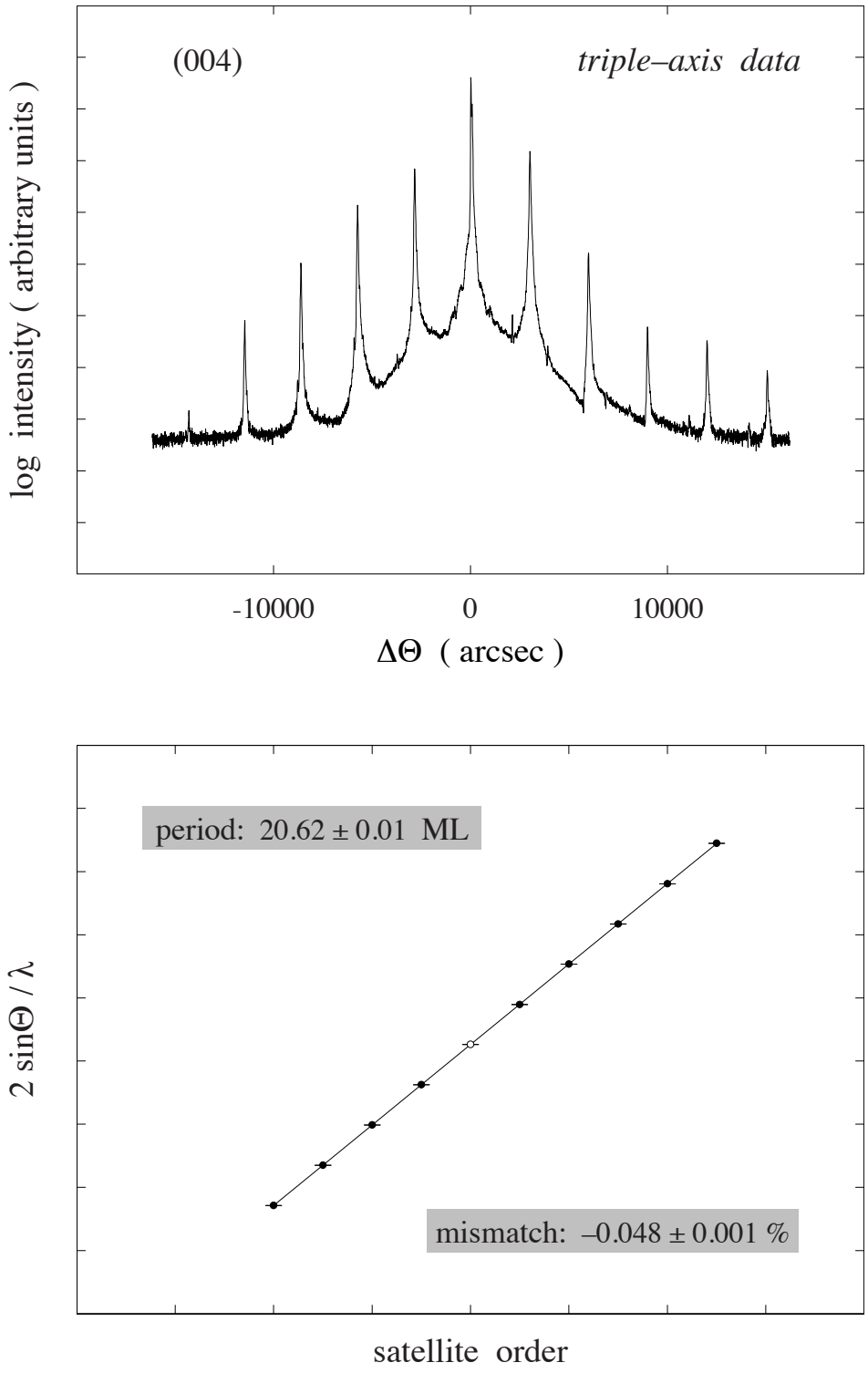

FIGURE 5.1 Conventional (004) triple–axis HRXRD measurement (top) and corresponding superlattice period from Bragg's law (bottom), reproduced from Fig. 3.2.

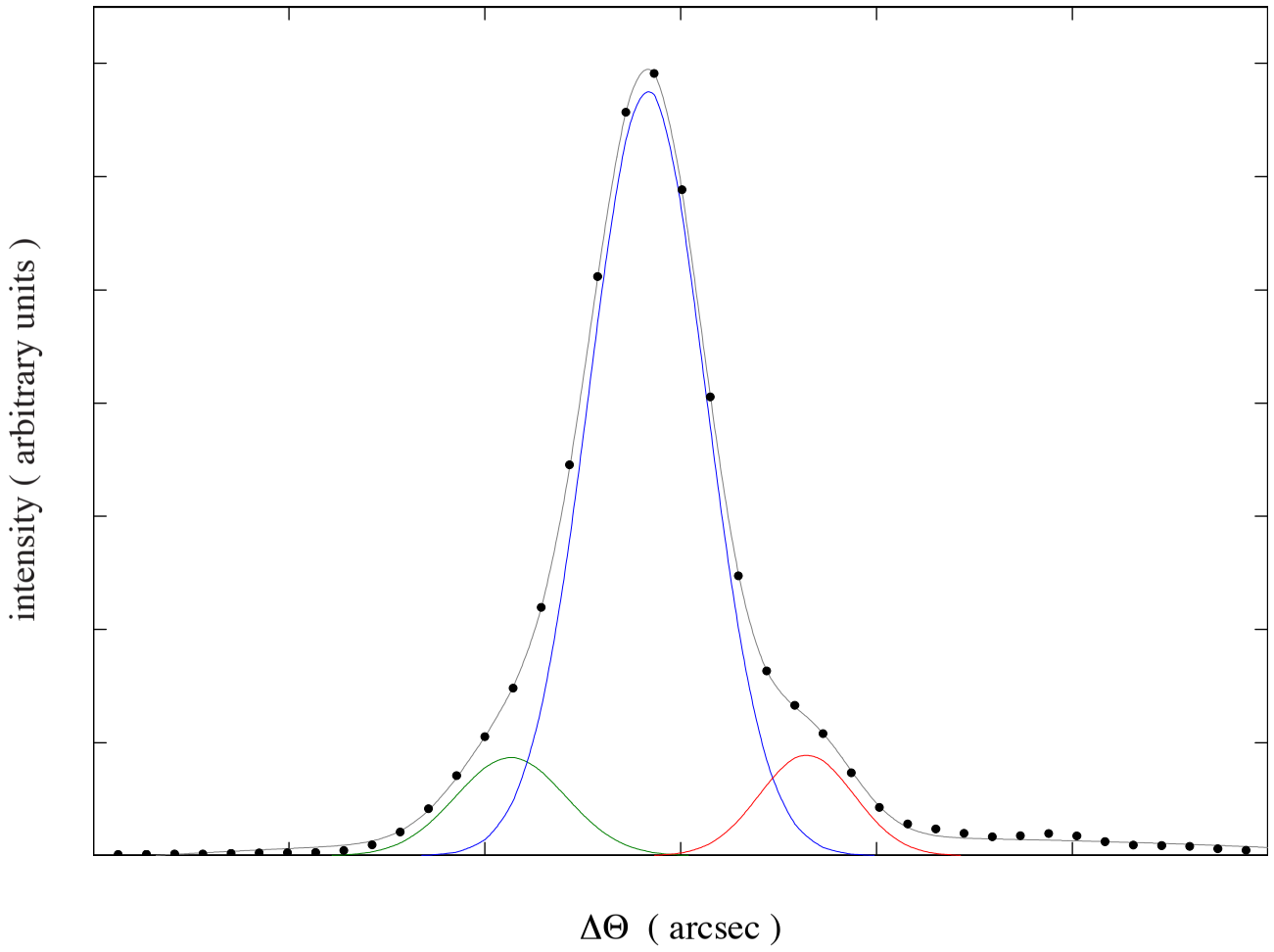

FIGURE 5.2 Each satellite in the HRXRD spectrum of Fig. 5.1 may be decomposed into a superposition of Gaussian curves. Here, for example, the second peak on the compressive side ($\Delta\Theta < 0$) is accurately represented as a sum (grey) of three, distinct Gaussian components.

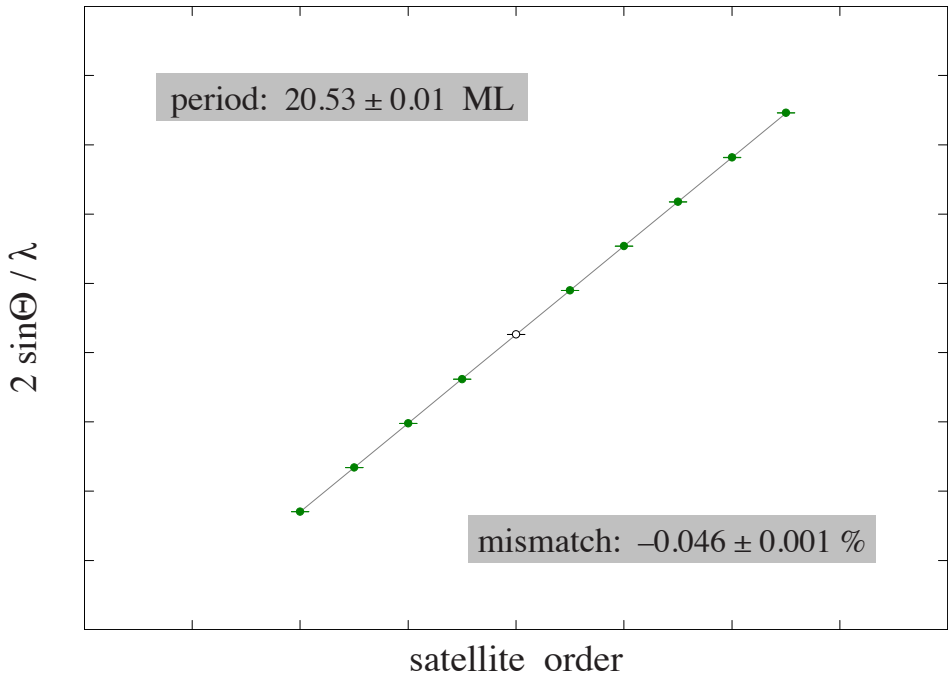

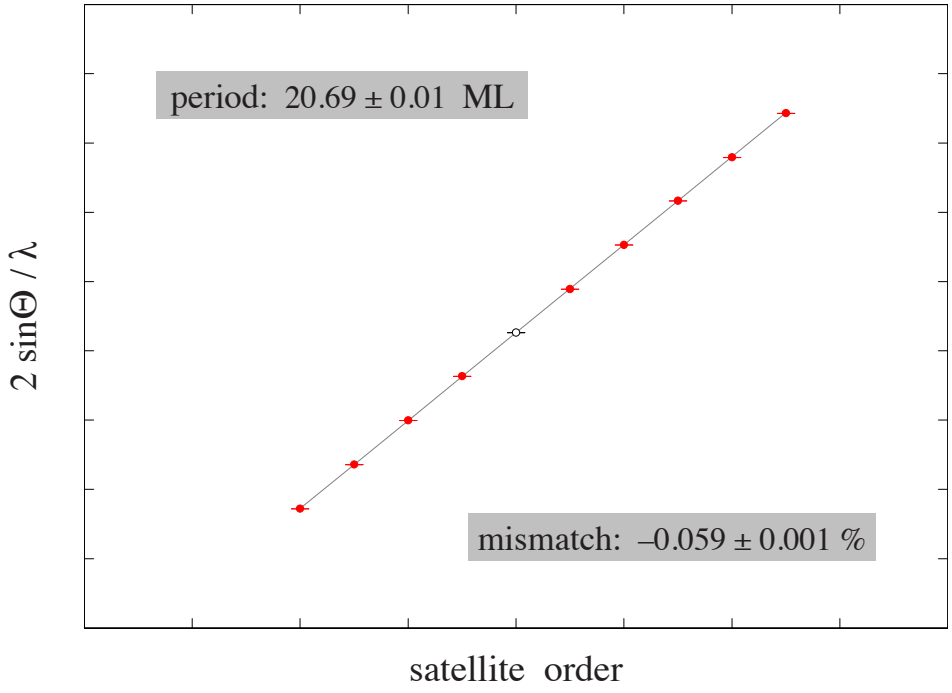

FIGURE 5.3 Bragg law fits to the auxiliary satellite peaks illustrated in Fig. 5.2, indicating possible presence of 20.53 and 20.69 ML periods within the multilayer stack.

stack. We must also consider that the x–ray peaks may be interpreted in other ways; for example, if we consider only the smaller peaks to the right–side of each satellite, we get a period of 20.65 ± 0.01 ML. Thus, we seek an analytical method that will permit reliable period measurements anywhere along the multilayer stack, a requirement admirably fulfilled by cross–sectional STM.

Local Period Measurement with STM

We first recount, briefly, the non–idealities accompanying the piezoelectric raster mechanism used in scanning tunneling microscopes [40]. In Chapter II, we described how the tripod scanner exhibits undesirable distortion effects (such as piezo creep and hysteresis) that make accurate length measurements problematic, along with empirically–established protocols for acquiring minimally–distorted data. We demonstrate here that under suitable circumstances one may overcome these inherent deficiencies to transform STM into a surprisingly accurate period–measurement tool.

To most conveniently ascertain atomic spacing with STM, we transition from real to reciprocal space by performing a two–dimensional (2–D) discrete Fourier transformation (DFT) on atomic–resolution images. One such image – of the Sb-sublattice over a GaSb substrate – is shown in Fig. 5.4 left, and its corresponding reciprocal space map easily obtained. This is repeated with each STM image in a given survey (in this case, over the substrate), and the survey–average reciprocal–space map (Fig. 5.4, right) is readily constructed. Constructive interference in the 2D-DFT results in localized spots oriented along the [001] (circled in red) and [110] (circled in white)

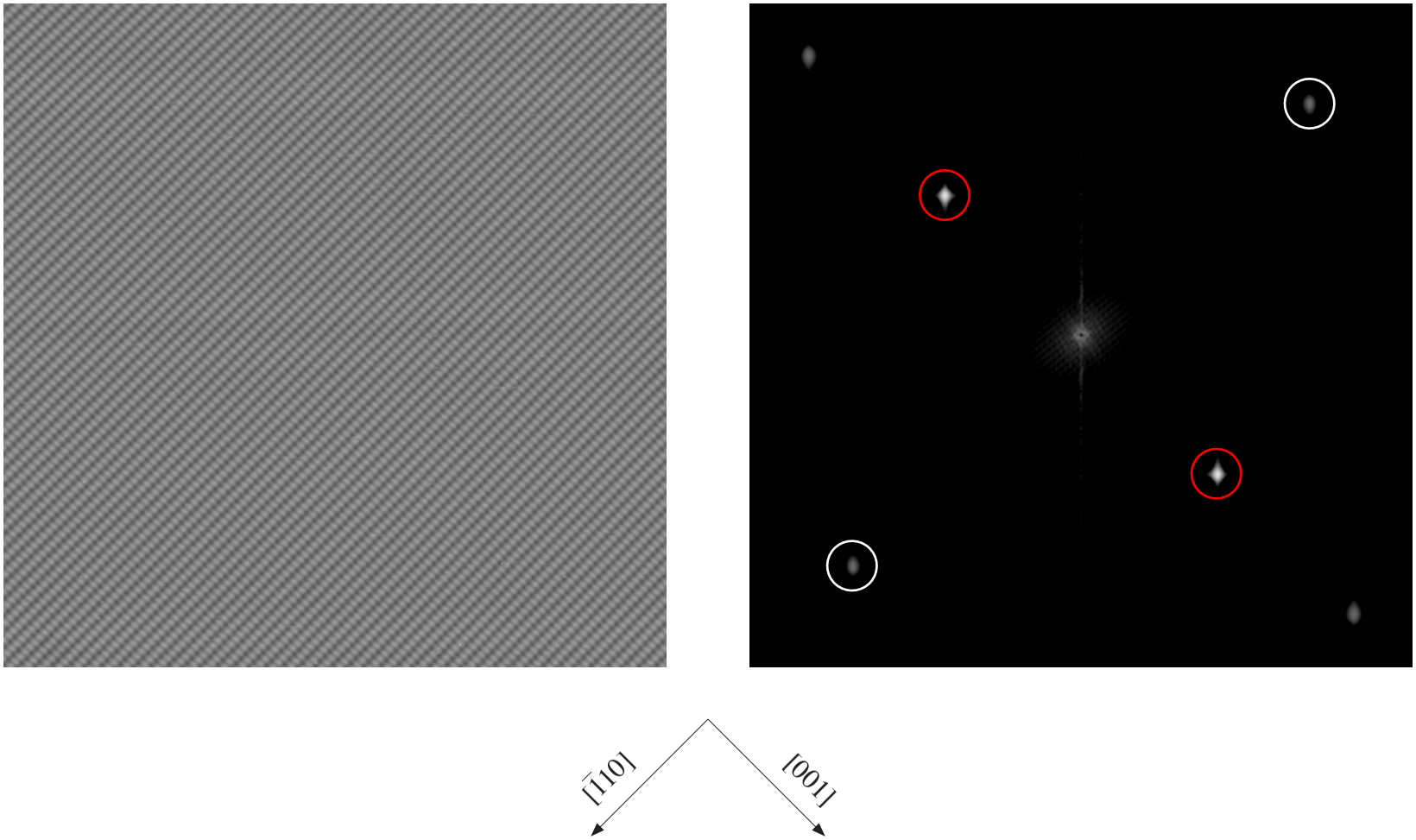

FIGURE 5.4. Atomic–resolution, filled–state STM image over a GaSb substrate (left) and survey–average reciprocal–space map (right). Bright spots denote the [001] (red) and [110] (white) reciprocal–lattice vectors defining the two–dimensional surface mesh.

reciprocal–lattice vectors, establishing the two–dimensional surface mesh. For a given STM image, all length measurements may be referenced to these locally determined reciprocal–lattice vectors [23], which constitute natural rulers automatically calibrated in units of the underlying crystal structure's lattice constant. Provided the corresponding image size is appropriately constrained, this normalization effectively factors out the piezo non–idealities discussed in Chapter II.

A representative atomic–resolution image is shown in Fig 5.5, where the black outline indicates a standard 400 Å by 400 Å crop area for the two–dimensional (2–D) discrete Fourier transformation (DFT). The size and location of this crop area were adopted to minimize the non–linear distortion effects previously described. The resulting power spectrum shown in Fig. 5.6 (right) is derived from the ensemble of atomic–resolution images (left) compromising a lateral survey. It shares the same [001] and [110] reciprocal–lattice vectors as the substrate–survey DFT in Fig. 5.4 (right), but now includes additional sets of superlattice satellite peaks convolved with the zone–center (blue) and [001] reciprocal–lattice vectors (red).

Due to reflection symmetry, the positive and negative zone–center satellite peaks are not independent, so we cannot use both; all [001]–convolved satellite peaks *are* independent of one another, however. These satellites, illustrated in Fig. 5.7 (top), are analogous to those observed in conventional (004) x–ray rocking curves. The small shoulders on either side of each [001] peak are artifacts due to the finite–crop window and unrelated to the superlattice period itself.

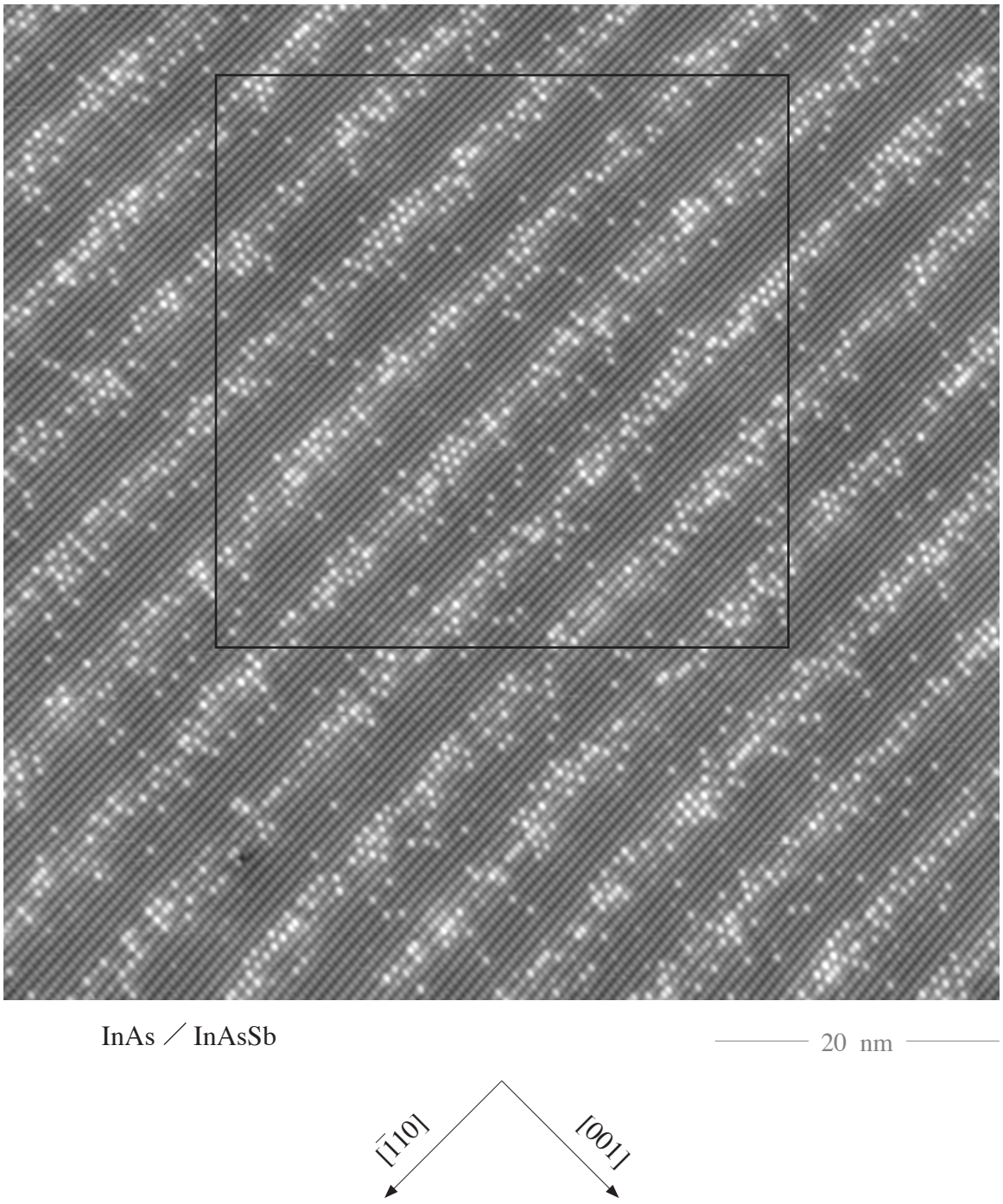

FIGURE 5.5. Representative atomic–resolution STM image of the anion (Sb, As) sublattice over a type–II InAs / InAsSb superlattice; solid outline indicates two–dimensional discrete Fourier transform crop area. Growth direction is from top–left to lower–right.

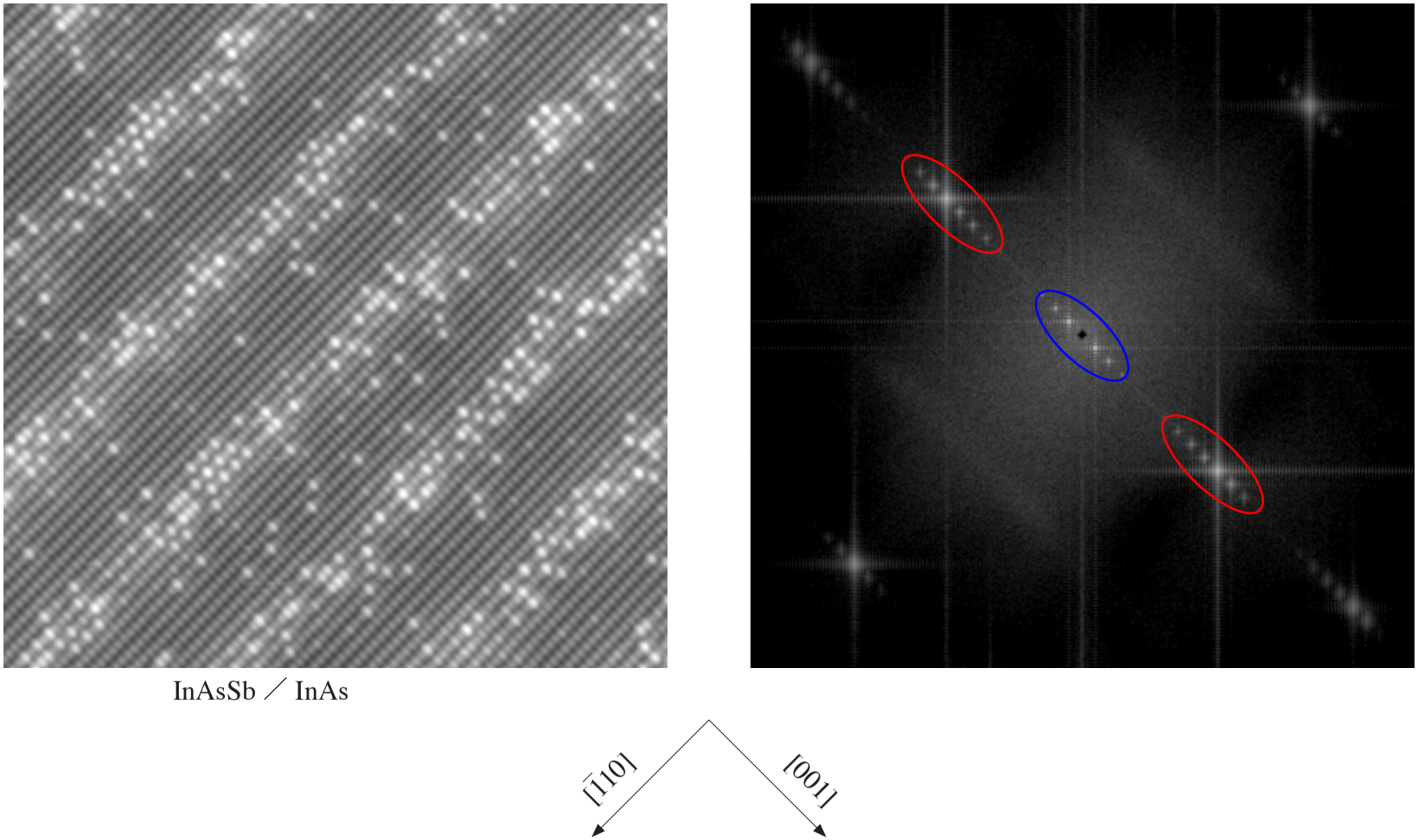

FIGURE 5.6. Representative single image crop from Fig. 5.5 (left) and survey–average reciprocal–space map (right). Superlattice satellite peaks symmetrically positioned about the zone center (blue) and asymmetrically convolved with the [001] reciprocal lattice vector (red) characterize the longer–range, periodic modulation of the underlying host lattice with substitutional antimony.

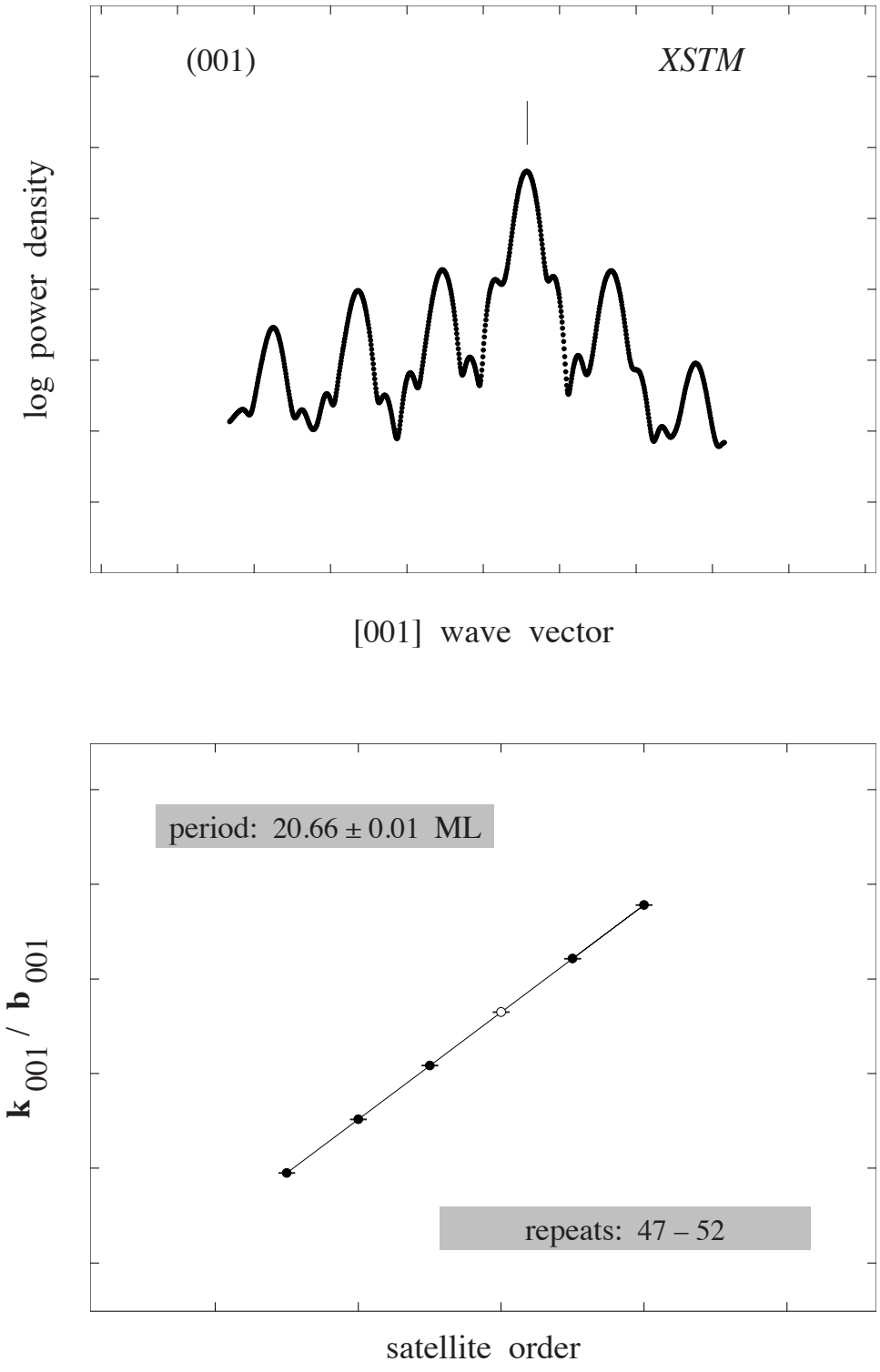

FIGURE 5.7. An [001]–section (top) through the survey average power spectrum of Fig. 5.6; hash mark indicates the [001] peak. Like their x–ray analogs in Fig. 5.1, the spacing between satellite peaks, here, may be used to determine the superlattice period (bottom).

Satellite peaks in the x–ray spectrum (Fig 5.1, top) are used to determine the average superlattice period via Bragg's Law (Fig. 5.1, bottom). The STM–derived satellite peaks in reciprocal space may be likewise used to determine a local superlattice period for any selected subset of bulk repeats via the two–dimensional analogue of this law. The spacing between satellite peaks as a function of peak order is again inversely proportional to the superlattice period, as shown in Fig. 5.7 (bottom).

The [001]–section in Fig. 5.7 (top) is taken through the survey average power spectrum of Fig. 5.6 (right). For an "ideal" STM, signal–to–noise is improved by averaging single–image measurements absent any systematic drift in the survey. However, this logic overlooks the fact that, in reality, the piezo properties change frame–by–frame, as described in Chapter II. A plot of the reciprocal–lattice vector *x*– and *y*–components for a representative survey (Fig. 5.8) emphasizes the point: the *x*–component is far more stable and reproducible from image to image than the *y*–component. This is unsurprising since piezo creep is always more pronounced in the slow–scan direction as explained in Chapter II.

It is clear from the foregoing that one is best served by separating reciprocal–lattice vector components, and we henceforth focus entirely on the *x*–component alone[19]. For local period measurements then, each of the evenly–spaced [001]–convolved

[19] The plot in Fig. 5.7 (top) includes both x– and y–components because it is aligned with the survey average [001]. The points in the bottom plot, however, are the survey average x–components normalized to the survey average [001] reciprocal lattice vector x–components. It is important to add that period measurements calculated with the *y*–component are typically within 1% of the *x*–components in spite of the notable drift of the *y*–piezo.

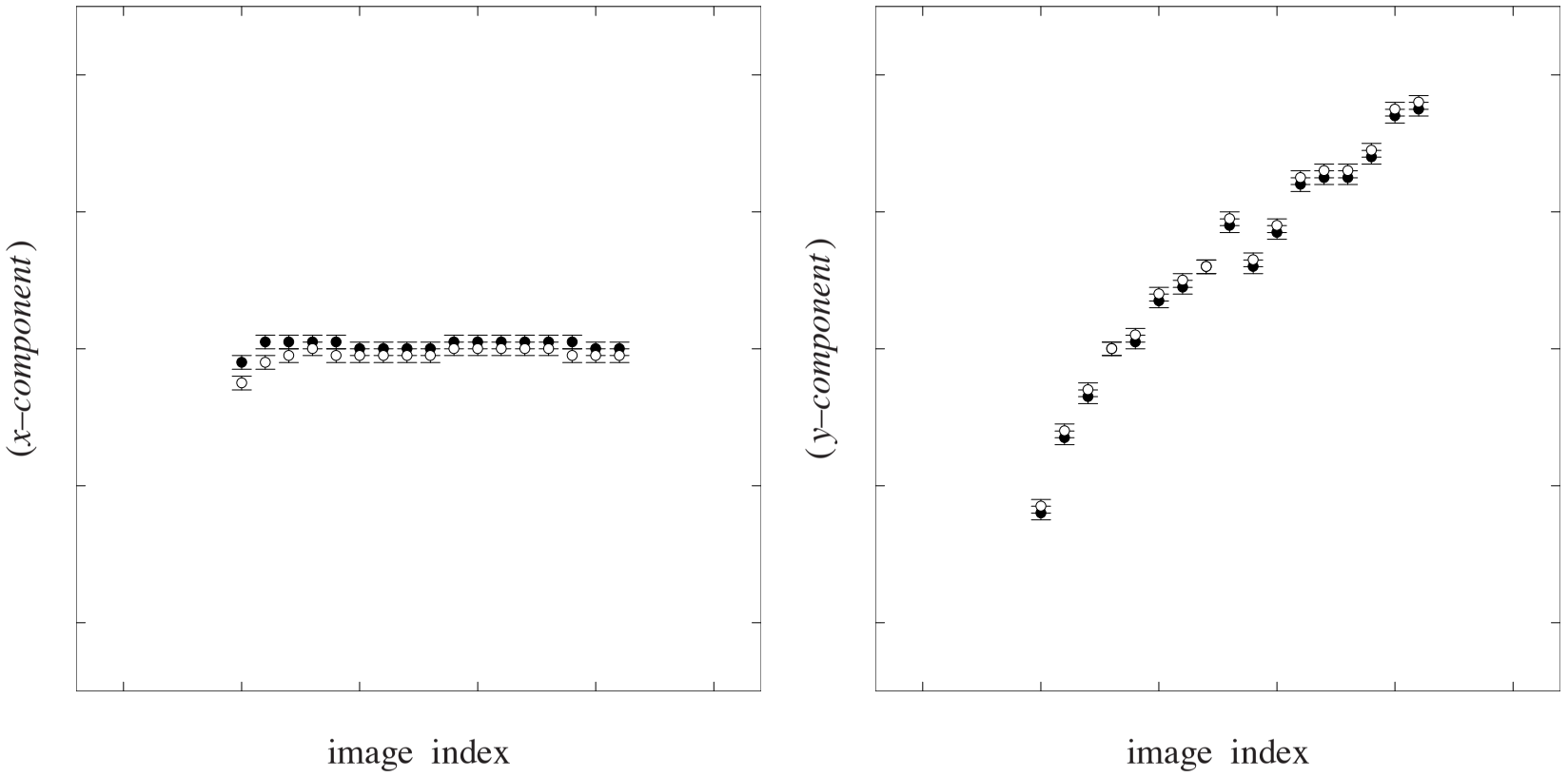

FIGURE 5.8. [001] reciprocal–lattice vector x– (left) and y– (right) components from a lateral survey over an InAs/InAsSb superlattice. Both components have the same vertical range (with suppressed zero), clearly indicating the larger drift in y throughout the survey. Full range for x– and y–components is ~ 0.3% and 3.6% of their respective mean value. The horizontal axis is image number, which is the same for both plots. Piezo hysteresis notwithstanding, the reciprocal–lattice vectors from forward– (closed circles) and reverse– (open circles) scans agree remarkably well (better than a part–per–thousand).

satellite peaks is normalized to the respective [001] reciprocal–lattice vector on an image–by–image basis, and subsequently averaged across all images in the lateral survey. Average satellite positions are plotted as a function of satellite order and fit to a straight line as in the x–ray spectrum of Fig. 5.1[20], with the superlattice period obtained from the inverse slope of this line.

Errors in x–ray measurements (Fig. 5.1) are determined by the error in the Gaussian fit to each satellite, and that error is used to weigh the linear fit to the satellite positions. For the STM–DFT period measurements, a measurement error of one pixel is included in the numerator and denominator when normalizing the [001]–convolved satellite peaks to the respective [001] reciprocal–lattice vector. That error is propagated when averaging the satellite position across all images and then used to weigh the linear fit. The resulting fit error, which we refer to as the "Bragg error", is surprisingly good (± 0.01 ML) for the superlattice periods shown in Fig. 5.9.

The STM–DFT period measurements in Fig. 5.9 (closed circles) are compared against the rational–fraction approximations (20.50 and 20.67, dashed lines) from Chapter III for subsets of periods from three survey locations in the multilayer stack in two orthogonal cross sections. We see that early– and late–period measurements all uniformly agree with the 20.50 ML approximation. Likewise, both middle period surveys are in good agreement with one another and with the 20.67 ML approximation.

[20] One important difference, however, is the lattice mismatch of the structure cannot be obtained with the STM–DFT method since all peaks are referenced to the local [001] spacing in the multilayer stack without any reference to the substrate.

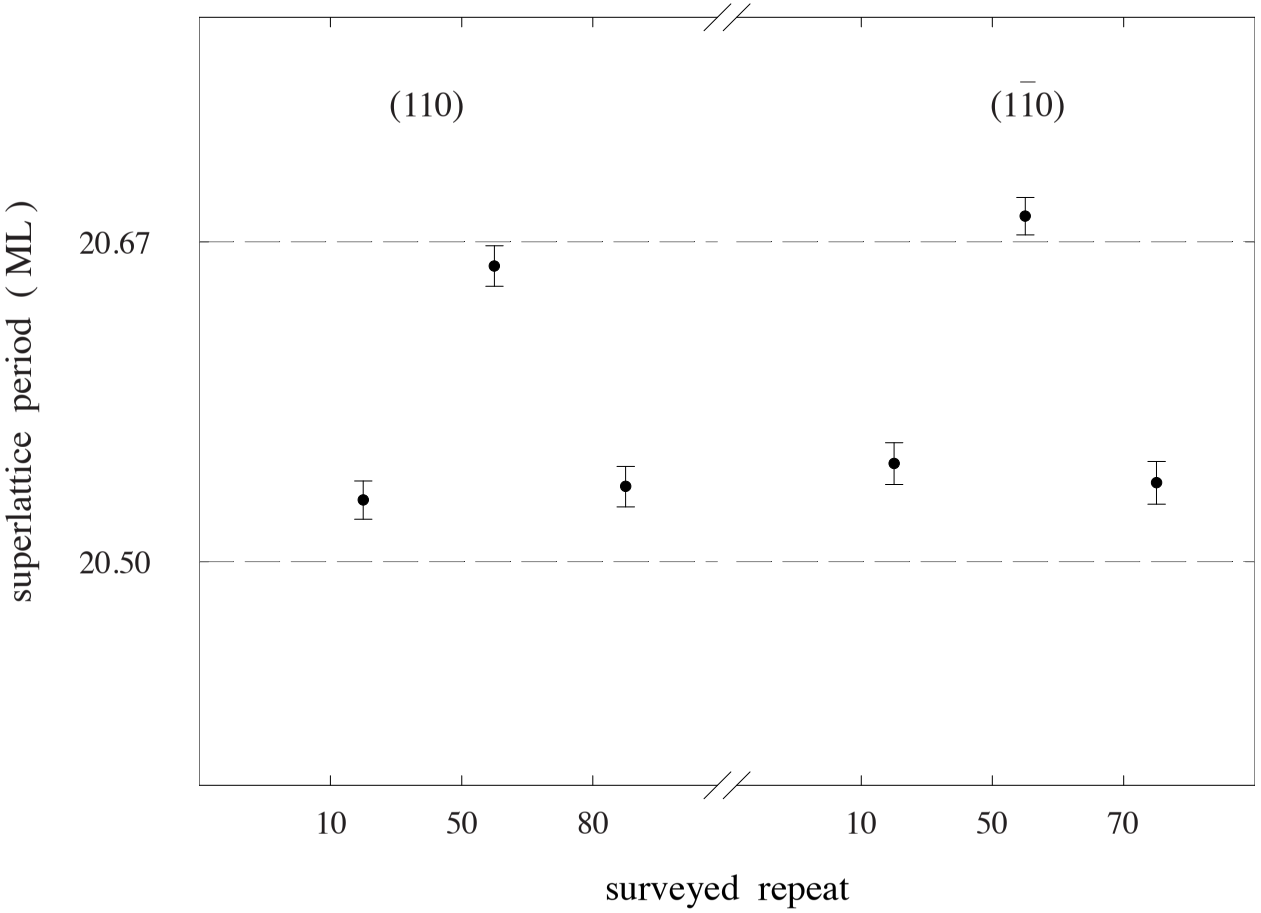

FIGURE 5.9. Direct comparison of the survey average superlattice periods deduced via the reciprocal–space discrete Fourier transform (closed circles), with the periods previously obtained from a sliding–window average (dashed lines, Fig. 3.10).

These same surveys were likewise analyzed in direct–space using the periodic antimony impurity profiles precisely mapped with STM. The profiles were described by a segregation model [46], which fit the spacing between InAsSb repeats providing quantitative period measurements, as detailed in Chapter IV. The resulting superlattice periods (Fig. 5.10, open circles), again independently corroborate the STM–DFT period measurements[21] (Fig. 5.10, closed circles).

The agreement between our reciprocal–space analysis, direct–space impurity profile, and the sliding–window averages provides a strong argument that normalizing to the reciprocal–lattice vector on an image–by–image basis effectively circumvents the non–idealities caused by the piezo scanner. This conclusion is further validated by observing the agreement between measurements obtained when the piezo scanner is elongating versus contracting (Fig. 5.11) – physical situations on opposite sides of the hysteresis loop that characterizes piezo non–linearity.

It is important to note our validation of this reciprocal–space technique means it can be confidently applied to other heterostructures, including those for which a direct–space impurity profile is unavailable, as in the quantum cascade materials studied in reference [23]. There, local periods calculated for lateral surveys acquired over selected

[21] As a separate confirmation of the agreement between the STM–DFT and compositional profile period measurement techniques, we refit the profile data with the segregation model, requiring the spacing between InAsSb repeats to be equal to the respective period measurements from the STM–DFT technique. The resulting fits were visually indistinguishable from the original.

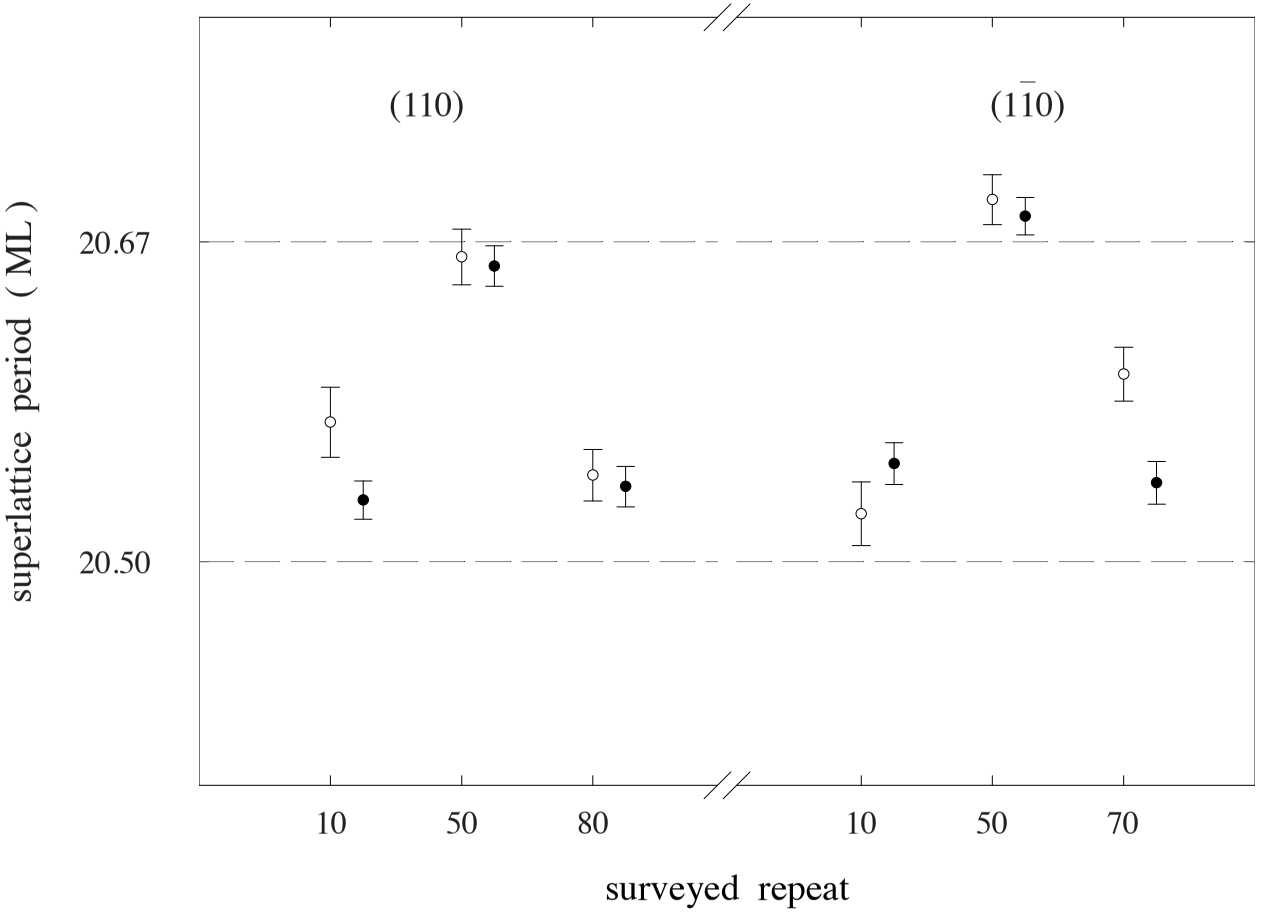

FIGURE 5.10. Direct comparison of the survey average superlattice periods deduced via the reciprocal–space discrete Fourier transform (closed circles), with the periods previously obtained from either a continuum segregation model (open circles, Fig. 4.10) or sliding–window average (dashed lines, Fig. 3.10).

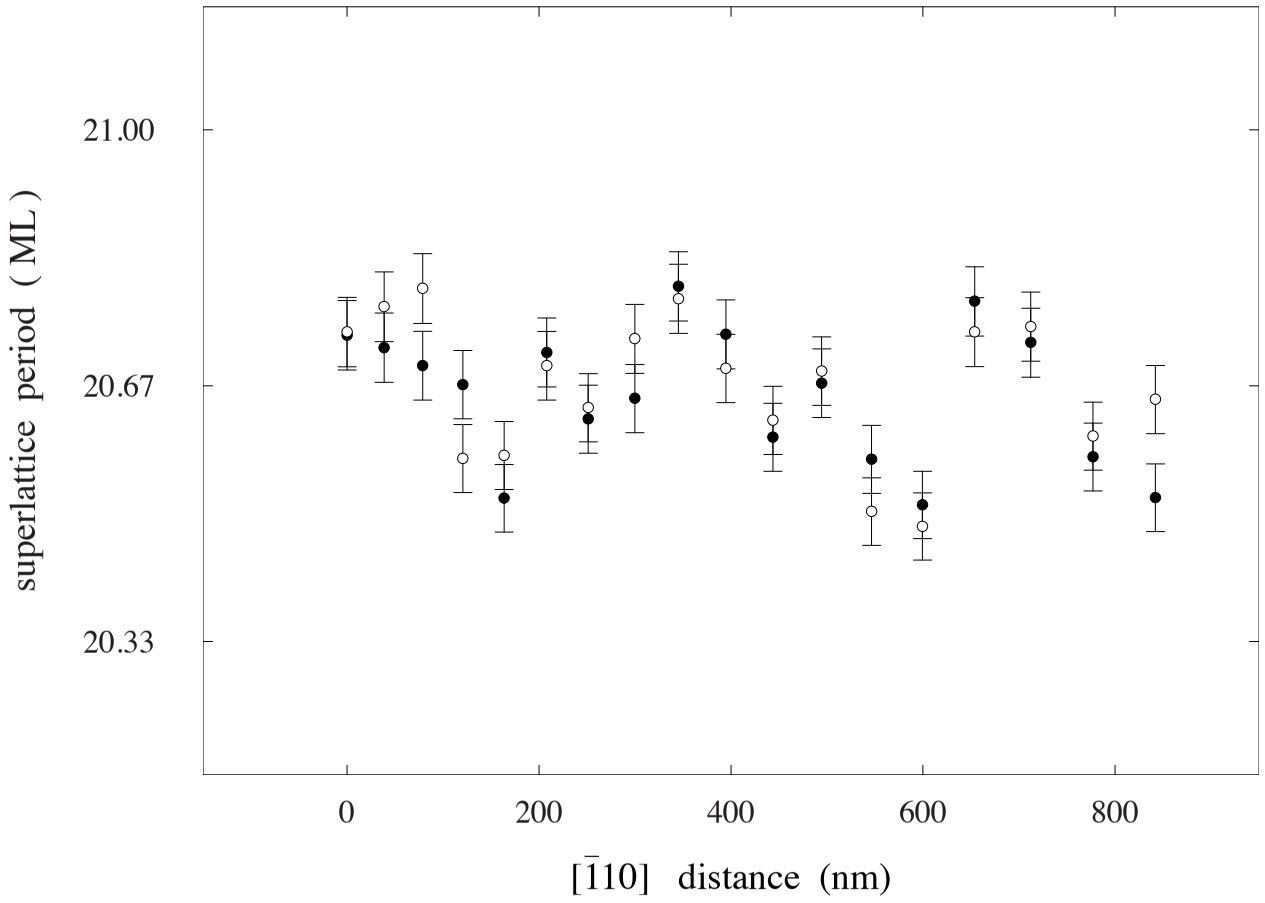

FIGURE 5.11. Reciprocal–space superlattice periods deduced from individual STM images across an entire [110] lateral survey centered about period 50 (Fig. 5.9). Consistency between independent data acquisitions with the piezo scanner elongated (open circles) and subsequently contracted (solid circles) demonstrates the reciprocal–space method successfully circumvents the real–space, piezo–raster deficiencies documented in Chapter II.

subsets of the multilayer stack (as well as their global average) again agreed remarkably well with HRXRD period measurements.

The image–by–image period measurements assembled in Fig. 5.11 represent a fixed subset of superlattice repeats surveyed along the <110> direction and centered about repeat 50 (Fig. 5.9). In this case, Bragg–like fits were applied to normalized satellite peaks from each STM image in the survey, with the resulting periods determined to ~0.05 ML[22]. From one image to the next, on the other hand, measurements differed by ~0.2 ML, an amount outside Bragg–like errors[23]. The source of this variation is still being investigated, however ongoing work by fellow lab members on interface roughness in quantum cascade materials has shown that fluctuations similar to these can arise from lateral correlations present within the interface, where they emulate the underlying stochastic process. When looked at this way, each image is a physical realization originating from the infinite ensemble that describes the stochastic process, yet each member of the ensemble can be characterized with convincing accuracy.

Summary

We have developed a two–dimensional reciprocal–space technique analogous to conventional HRXRD that transforms a scanning tunneling microscope into an accurate

[22] The errors in the single–image measurements are ~ 5x larger than the survey measurement Bragg errors shown in Fig. 5.9 and 5.10, since the errors are no longer reduced by the square-root of the number of images.

[23] Despite these fluctuations, overlapping STM images reliably yield the same period measurement even if the images are taken several hours apart.

tool for local period measurements in heterostructures. Device–scale STM surveys over selected subsets of an InAs/InAsSb superlattice provide statistically significant ensembles from which precise periods may be obtained. Satellite peaks in the discrete Fourier transform of atomic resolution STM images that are normalized to the [001] reciprocal–lattice vector successfully remove the distortions inherent to tripod–style piezo scanners, as demonstrated by the agreement between periods obtained from reciprocal space, sliding–window averages, and direct–space profiles for nominally the same dataset. All three methods point to a reproducible variation in the local superlattice periodicity at select points throughout the growth. Finally, the reciprocal–space method period measurements also reveal unanticipated fluctuations in the growth–plane that, although not pursued here, may be an additional source of energy–level broadening in optical devices based on these superlattices.

CHAPTER VI

CONCLUSIONS

We have used cross–sectional scanning tunneling microscopy to examine a gallium–free, type–II InAs/InAsSb superlattice and perform compositional monolayer–by–monolayer analyses of the *as–grown* structure through isovalent impurity identification on the atomic scale. We discussed the optimization of cleaving protocols, upgrades to the vacuum system, and standardized lab protocols to minimize the undesirable effects of STM raster non–idealities during data acquisition. These improvements allowed for representative, device–scale, lateral STM surveys to be conducted over select subsets of the multilayer stack, providing statistically–significant image ensembles for analysis.

We described the development of optimal counting protocols for identification of surface antimony–for–arsenic substitutions, where select areas are chosen across a full set of survey images. This identification facilitates monolayer–by–monolayer analyses of the antimony fraction across the surveyed repeats, as well as reconstruction of representative bulk composition profiles based on appropriate approximations to the bulk period dictated by commensurability conditions. These bulk profiles manifest exponential–like increases and decreases in incorporated antimony at the InAsSb–on–InAs and InAs–on–InAsSb interfaces, respectively, consistent with anion segregation, as well as an offset likely due to anion cross–incorporation. Agreement between STM–based HRXRD simulations and the experimental spectrum pinpoints compositional

grading as the major source of discrepancies between intended and *as–grown* x–ray spectra.

We likewise have developed a quantitative, continuum segregation model to fit the observed antimony profiles, and examined the resulting fit parameters. These fits conclusively establish antimony segregation, and cross–incorporation, as the physical mechanisms driving the observed compositional grading across superlattice interfaces, and asymptotic antimony fractions, respectively.

The model best describing the bulk profile relies on two, spatially distinct segregation sources with a spatial offset close to one monolayer, consistent with either monolayer roughness or substrate vicinality. This model also provides self–consistent period measurements over surveyed sections of the multilayer stack that are comparable with bulk period approximations based on translationally–invariant sliding window averages. Agreement between these two seemingly different approaches substantiates the occurrence of more than one bulk period in the multilayer stack. The insights achieved through such detailed analyses of the *as–grown* structure can then be combined with STM and SIMS data pointing to a vertical evolution in the total incorporated antimony per period to obtain x–ray simulations in excellent agreement with the experimental HRXRD spectrum.

Finally, we have demonstrated a novel reciprocal–space technique, analogous to Bragg's law in x–ray diffraction, that transforms cross–sectional STM into a precision tool for measuring local periods in superlattice structures. The non–idealities associated with STM piezo scanners are effectively factored out through normalization of the

superlattice satellite peaks in a two–dimensional discrete Fourier transforms of atomic–resolution STM images to the corresponding reciprocal lattice vector with which they are convolved. Comparison of the period measurements obtained with this technique and those from either the sliding–window average or segregation–model validate the accuracy of this new method, providing confidence in its more general use with other heterostructures absent similar impurity profiles.

REFERENCES

[1] J.N. Schulman, T.C. McGill, Applied Physics Letters, 34 (1979) 663-665.

[2] A. Rogalski, Reports on Progress in Physics, 68 (2005) 2267.

[3] E.F. Schubert, http://www.LightEmittingDiodes.org, Cambridge University Press

[4] C.-A. Chang, R. Ludeke, L.L. Chang, L. Esaki, Applied Physics Letters, 31 (1977) 759.

[5] E. Plis, A. Khoshakhlagh, S. Myers, H.S. Kim, N. Gautam, Y.D. Sharma, S. Krishna, S.J. Lee, S.K. Noh, The 40th National Symposium of the American Vacuum Society, 28 (2010) C3G13-C13G18.

[6] R.M. Feenstra, D.A. Collins, D.Z.Y. Ting, M.W. Wang, T.C. McGill, The 40th National Symposium of the American Vacuum Society, 12 (1994) 2592-2597.

[7] J. Harper, M. Weimer, D. Zhang, C.H. Lin, S.S. Pei, Applied Physics Letters, 73 (1998) 2805-2807.

[8] J. Steinshnider, J. Harper, M. Weimer, C.H. Lin, S.S. Pei, D.H. Chow, Physical Review Letters, 85 (2000) 4562-4565.

[9] G.A. Sai-Halasz, L. Esaki, W.A. Harrison, Physical Review B, 18 (1978) 2812-2818.

[10] C. Mailhiot, D.L. Smith, Journal of Vacuum Science & Technology A: Vacuum, Surfaces, and Films, 7 (1989) 445-449.

[11] C.H. Grein, P.M. Young, M.E. Flatte, H. Ehrenreich, Journal of Applied Physics, 78 (1995) 7143-7152.

[12] D.R. Rhiger, Journal of Elec Materi, 40 (2011) 1815-1822.

[13] S.P. Svensson, D. Donetsky, D. Wang, H. Hier, F.J. Crowne, G. Belenky, Journal of Crystal Growth, 334 (2011) 103-107.

[14] E.H. Steenbergen, B.C. Connelly, G.D. Metcalfe, H. Shen, M. Wraback, D. Lubyshev, Y. Qiu, J.M. Fastenau, A.W.K. Liu, S. Elhamri, O.O. Cellek, Y.-H. Zhang, Applied Physics Letters, 99 (2011).

[15] Wikipedia.org, https://en.wikipedia.org/wiki/Molecular_beam_epitaxy 12/02/2015

[16] U.C. London, http://www.ee.ucl.ac.uk/about/MBE 12/02/2015.

[17] A.Y. Cho, Microelectronics Reliability, 11 (1972) 485.

[18] P. Dhez, C. Weisbuch, Physics, fabrication, and applications of multilayered structures, New York : Plenum Press 1988.

[19] R. Fernandez, The 40th National Symposium of the American Vacuum Society, 6 (1988) 745-748.

[20] E. Michel, G. Singh, S. Slivken, C. Besikci, P. Bove, I. Ferguson, M. Razeghi, Applied Physics Letters, 65 (1994) 3338-3340.

[21] P.I. Cohen, P.R. Pukite, J.M. Van Hove, C.S. Lent, Journal of Vacuum Science & Technology: Part A-Vacuums, Surfaces & Films, 4 (1986) 1251.

[22] J.A. Stroscio, W.J. Kaiser, Scanning tunneling microscopy, Boston : Academic Press 1993.

[23] F.L. Cruz, STM Characterization of Interface Roughness in InAlAs / InGaAs Superlattices Grown by MOCVD, Texas A&M University2015.

[24] C.B. Duke, 38th National Symposium of the American Vacuum Society, 10 (1992) 2032-2040.

[25] R.M. Feenstra, J.A. Stroscio, J. Tersoff, A.P. Fein, Physical Review Letters, 58 (1987) 1192-1195.

[26] J. Tersoff, D.R. Hamann, Physical Review B, 31 (1985) 805-813.

[27] E.T. Yu, Materials Science and Engineering: R: Reports, 17 (1996) 147-206.

[28] Omicron, (NanoTechnology GmbH (McMurray, PA)).

[29] G.W. Brown, The reaction of ammonia with GaAs(110) studied by scanning tunneling microscopy, Texas A&M University1997.

[30] G.A. Lengel, Structure and dynamics of vacancies on GaAs(110) studied by scanning tunneling microscopy, Texas A&M University1995.

[31] P. Extorr Inc. New Kensington.

[32] P. Technical Manufacturing Corp., MA.

[33] S. Bradbury, P. Evennett, Contrast techniques in light microscopy, Bios Scientific Publishers1996.

[34] P.C. Robinson, S. Bradbury, Qualitative polarized-light microscopy, Oxford University Press1992.

[35] H. MDC Vacuum Products LLC., CA).

[36] W. Gulf Coast Data Concepts LLC., MS).

[37] I.H. Musselman, P.E. Russell, Journal of Vacuum Science & Technology: Part A-Vacuums, Surfaces & Films, 8 (1990) 3558.

[38] C. Sosolik, Honors Program Thesis, Texas A&M University, (1995).

[39] E.P. Stoll, Ultramicroscopy, 42 (1992) 1585-1589.

[40] J.F. Jorgensen, Journal of vacuum science & technology. B, , 12 (1994) 1702-1704.

[41] E.H. Steenbergen, O.O. Cellek, Y.H. Zhang, D. Lubyshev, Y. Qiu, J.M. Fastenau, A.W.K. Liu, Proceedings of SPIE - The International Society for Optical Engineering 2012.

[42] I. Vurgaftman, J.R. Meyer, L.R. Ram-Mohan, Journal of Applied Physics, 89 (2001) 5815.

[43] P.F. Fewster, X-ray scattering from semiconductors, 2nd ed. ed., London : Imperial College Press2003.

[44] S. Stepanov, http://sergey.gmca.aps.anl.gov.

[45] P.R. Bevington, D.K. Robinson, Data reduction and error analysis for the physical sciences, 3rd ed. ed., Boston : McGraw-Hill2003.

[46] M.R. Wood, K. Kanedy, F. Lopez, M. Weimer, J.F. Klem, S.D. Hawkins, E.A. Shaner, J.K. Kim, Journal of Crystal Growth, 425 (2015) 110-114.

[47] K. Mahalingam, E.H. Steenbergen, G.J. Brown, Y.-H. Zhang, Applied Physics Letters, 103 (2013) 061908.

[48] Y. Sun, S.E. Thompson, T. Nishida, Strain effect in semiconductors : theory and device applications, New York ; London : Springer2010.

[49] S. Adachi, Properties of group-IV, III-V and II-VI semiconductors, Chichester, England : John Wiley2005.

[50] A.Y. Lew, E.T. Yu, Y.H. Zhang, Journal of Vacuum Science & Technology B, 14 (1996) 2940-2943.

[51] K. Muraki, S. Fukatsu, Y. Shiraki, R. Ito, Journal of Crystal Growth, 127 (1993) 546-549.

[52] SigmaPlot, sigmaplot.com (Systat Software).

[53] K. Matney, M.S. Goorsky, Journal of Crystal Growth, 148 (1995) 327-335.

[54] PeakFit, sigmaplot.com (Systat Software).